8-18-2023

Reduction in the Thermal Budget of Sputtered Indium Tin Oxide (ITO) to Potentially Broaden its use in Microelectronic Devices

Zachary Flowers
zcf1323@rit.edu

Recommended Citation

Flowers, Zachary, "Reduction in the Thermal Budget of Sputtered Indium Tin Oxide (ITO) to Potentially Broaden its use in Microelectronic Devices" (2023). Thesis. Rochester Institute of Technology. Accessed from

Reduction in the Thermal Budget of Sputtered Indium Tin Oxide (ITO) to Potentially Broaden its use in Microelectronic Devices

Zachary Flowers

A thesis submitted in partial fulfillment of the requirements for the
degree of Master of Science in Material Science and Engineering in the
School of Chemistry and Materials Science,
College of Science
Rochester Institute of Technology

August 18th, 2023

SCHOOL OF CHEMISTRY AND MATERIALS SCIENCE
COLLEGE OF SCIENCE
ROCHESTER INSTITUTE OF TECHNOLOGY
ROCHESTER, NEW YORK

CERTIFICATE OF APPROVAL

M.S. DEGREE THESIS

The M.S. Degree Thesis of Zachary Flowers has
been examined and approved by the thesis
committee as satisfactory for the thesis required for
the M.S. degree in Materials Science and Engineering.

Dr. Michael Jackson, *Thesis Advisor*

Dr. Santosh Kurinec

Dr. Bruce Kahn

Dr. Scott Williams

August 18th, 2023

Acknowledgments

I would firstly like to thank my Thesis advisor, Dr. Michael Jackson, for his continuous help and support. He was always willing to meet and go over any questions I had or roadblocks I encountered as well as demonstrating tool use in the RIT cleanroom. His knowledge, expertise, and guidance enhanced my understanding of and greatly aided in this work. I would also like to thank my Thesis committee, Dr.Bruce Kahn for his feedback and support; Dr.Santosh Kurniec for her assistance in TLM design; and Dr.Scott Williams for his advice, support, and assistance with XRD measurements.

I would also like to thank the RIT cleanroom staff: Thomas Grimsley, Sean O'Brien, John Nash, Bruce Tolleson, and Richard Battaglia for their continual efforts in updating and maintaining the cleanroom tools, assisting with tool certifications, and always being available to answer any questions I had. I would also like to acknowledge Tom Allston, for his help certifying and using the XRD tool.

I would like to dedicate this work to my family, who always pushed me to achieve and fully supported me in my academic efforts. Without their support, this achievement may not have been accomplished. I would also like to thank my friends and loved ones, whose constant encouragement during my academic experience focused and refreshed me.

Abstract

Indium tin oxide, ITO, is a transparent conducting oxide widely known for its low resistivity and high transmission in the visible spectrum. It is most commonly used as a contact in optoelectronic devices, where its transmission is paramount to the function of the device. In this work, a low thermal budget process to sputter ITO films to potentially expand its applications in the RIT cleanroom was developed. The baseline process utilized a dielectric In_2O_3:SnO_2 sputter target and a 2 hour, 400°C post deposition anneal step to achieve a high quality film. This work achieved films with similar properties, but with anneals of 1-2 hours in the 230-250°C range.

A new processing window using a metal InSn sputter target was derived. By reactively sputtering oxygen deprived ITO films and annealing them at lower temperatures, the overall thermal budget was reduced. DOE techniques were used to define the following optimal parameters: a partial pressure combination of 11.2mT of Ar and 0.8mT of O_2, deposition power of 95 or 100W, and a 10 minute presputter at 110W. Using these conditions, anneal DOEs were created and run. It was found that the power was a driving factor in the oxygen content and crystal structure of the film. Films sputtered at 95W were more glass-like and had a strong XRD (622) peak, while 100W films were more metallic and had a preferential (222) peak. It was found that a 95W film annealed for two hours at 230°C yielded an ITO film with the best combination of low resistivity, $9.55\text{x}10^{-4}\Omega$-cm, and good transmission, 78.54%, over the 380 to 750 nm range. These results are comparable to the baseline process, while reducing the anneal time by 2 hours and temperature by 170°C.

As a proof of concept, an ITO anti reflective coating, ARC, was used on three different silicon solar cells and compared to a SiO_2 ARC. The ITO ARC yielded functional cells with an AM1.5 efficiency of 8.8%, a fill factor of 65.37%, and an open circuit voltage of 541.4mV. However, since the ITO is not 100% transparent, it caused a slight decrease in the short circuit current, dropping from 42 to 40mA. The SiO_2 ARC cells on the same wafer exhibited lower V_{OC} values, which is indicative of processing issues with the oxide, so we cannot conclude the ITO ARC was better from our limited results. Annealing the ITO at 230°C for an hour caused a decrease in shunt resistance, from 250 to 15.4Ω, fill factor, from 67.3 to 37.9%, and efficiency, 8.7 to 7.3%. No such degradation occurred with the SiO_2 ARC cells on the same wafer, indicating that the 230°C anneal may have triggered an interaction between the ITO and the Ti/Al films. These results show future work may be needed to further lower the thermal budget for the ITO film process.

Contents

List of Figures

List of Tables

Chapter 1

Introduction

Transparent conducting oxides, TCOs, are typically doped metal oxides with high transmission in the visible spectrum of light and low resistivity. Common TCOs include aluminated zinc oxide, indium oxide, tin oxide, indium doped zinc oxide, and tin doped indium oxide [1]. These TCOs are most commonly used as electrodes in optoelectronic devices, where their transmissive properties are paramount. The most used and studied TCO is indium tin oxide, ITO, due to its high transmission and conductivity.

1.1 Overview of Indium Tin Oxide (ITO)

Indium Tin Oxide (ITO) is a ternary n-type semiconductor typically comprised of 90% indium oxide and 10% tin oxide by weight with a chemical formula of $In_{2-x}Sn_xO_3$ [2]. The indium oxide, In_2O_3, is considered the host material which is doped by the tin oxide, SnO_2. Due to its excellent transmission, 80-90% in the visible spectrum, and low resistivity, 10^{-4} Ω-cm, ITO has seen widespread use across various applications.

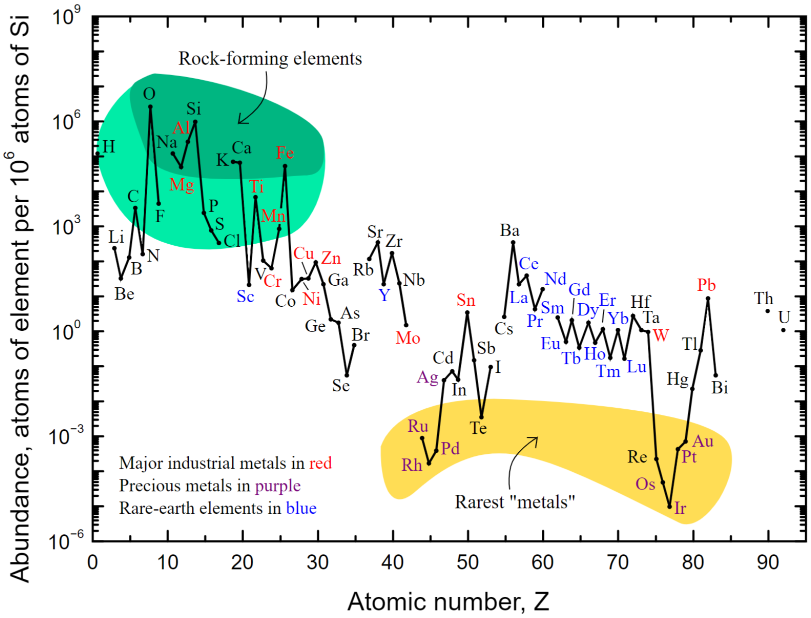

Figure 1.1: Abundance of Materials Per 10^{-6} Atoms Of Si [3].

The primary drawbacks of ITO are the cost and scarcity of the materials themselves. As seen in Figure 1.1, both indium and tin are rarer and more expensive than other materials used in TCO deposition. For example, the metals used in aluminated zinc oxide, Al and Zn, are among the most common elements found in the Earths crust and only cost $2.53 and $3.22 dollars per kg, respectively, whereas In and Sn cost $211.45 and $26.88 per kg as of 2023 [4]. Despite the sizable price difference between the two sets of metals, ITO is still the preferred transparent conducting oxide for most applications due to its electrical, optical, and physical properties.

1.2 Applications

Due to its transmission in the visible spectra and high conductivity, ITO has seen a wide variety of applications in microelectronic devices, optics, smartphones, and avionics. Both microelectronic devices and other applications will be discussed

1.2.1 Microelectronic Devices

One subset of microelectronic devices that ITO has seen wide use is photovoltaic and other optical devices. Photovoltaic refers to the photovoltaic effect, which describes the absorption of photons and generation of electron-hole pairs in a semiconductor. A diagram of this process can be seen in Figure 1.2.

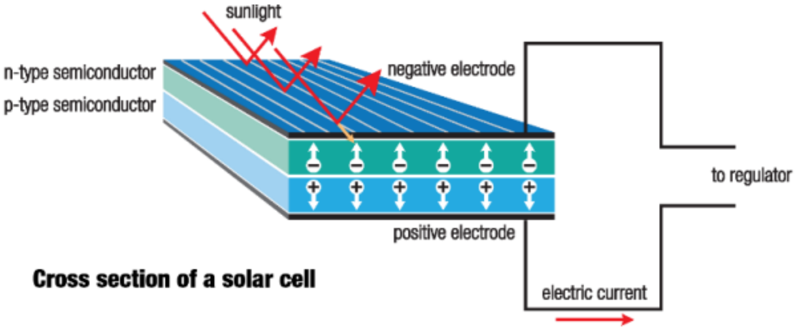

Figure 1.2: Diagram of the Photovoltaic Effect [5].

As shown in Figure 1.2, the incident photons are absorbed into the semiconducting material, where an electron-hole pair is generated and subsequently collected by the negative and positive electrodes, respectively. Since the majority of energy in the solar spectrum is located in the visible wavelengths [6], ITO's transmission in this range, conductive properties, and refractive index make it an ideal choice for an anti-reflective layer. The amount of reflection that occurs at an interface is dependent on the difference between refractive indices of the two materials, with a greater difference yielding a higher Reflectance. For example, if the interface being investigated is that between air and bare Si, with refractive indices of 1 and around 4 at a wavelength of 500nm, the reflection would be 0.39, or 39% of incident light of a wavelength of 500nm would be reflected. If a third material is introduced as an intermediary between the ambient and substrate, then the amount of reflected light could be reduced. Ideally, the new material would have a refractive index between the air and Si, such as ITO with a refractive index of around 2 at 500nm [7]. For the air-ITO interface, the reflection would be 0.11 while the ITO-Si interface also yields a Reflectance of 0.11. Therefore, the total reflection with an ITO film will be substantially lower than the air-Si film stack. Since ITO is also conductive, it mitigates the bottlenecks created by the fingers of the solar cell, as seen in Figure 1.3, and improves the collection of the generated carriers thereby decreasing the efficiency losses associated with recombination in the substrate or parasitic resistance [8].

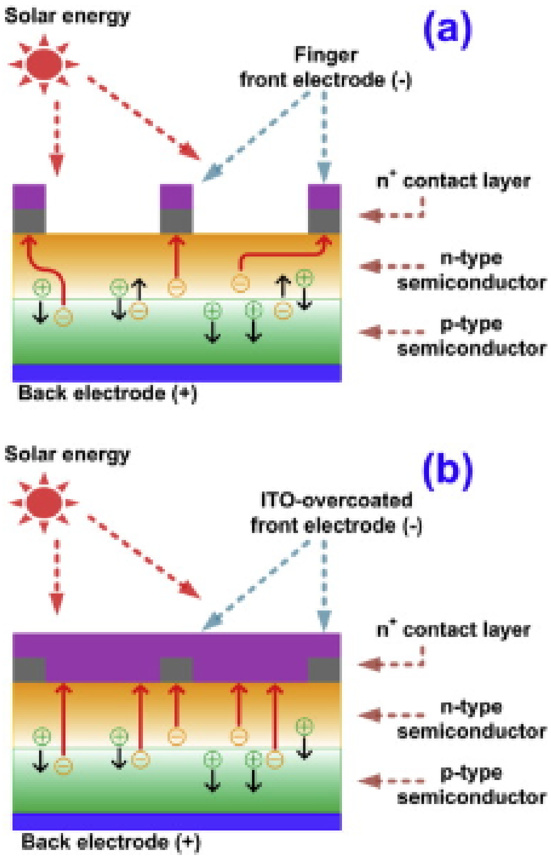

Figure 1.3: Use of Indium Tin Oxide as ARC [8].

ITO has also seen use as a pixel electrode in liquid crystal displays, LCDs. A liquid crystal changes the amount of light that propagates through it in response to an applied voltage. Since ITO can transmit both light and current, it serves as an ideal electrode to deliver voltage to the liquid crystal. The LCD device cross section can be seen in Figure 1.4.

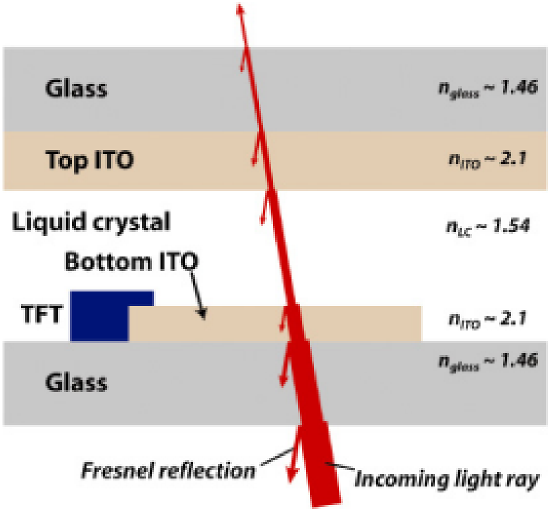

Figure 1.4: Liquid Crystal Display Cross Section [9].

The incoming light ray noted in Figure 1.4 is generated from a back light unit. This light passes through the LCD stack, exiting the device. While some loss in reflected light is associated with this stack, the ITO electrodes are invaluable to the function of this device. Liquid crystal displays are primarily used in flat screen televisions and smart phone screens.

Another optical microelectronic device where ITO is prevalent is a light emitting diode (LED), specifically an organic LED, OLED. Pictured in Figure 1.5 is a cross section of an OLED.

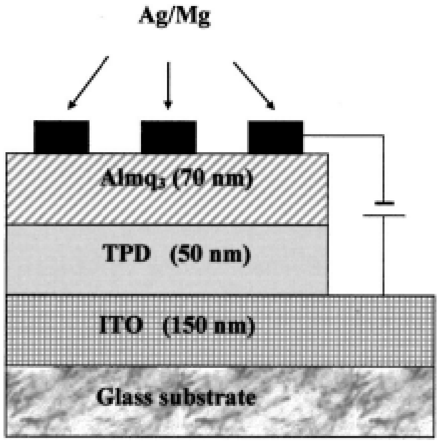

Figure 1.5: Organic Light Emitting Diode With an ITO Anode [7].

The layers in Figure 1.5 are defined as follows: Almq$_3$ is an electron transport and emitting layer made of 4-methyl-8-hydroxyquinolinolato aluminum(III); TPD is a hole transport layer comprised of

N,N-Bis(3-methylphenyl)-N,N-diphenylbenzidine; ITO acts as a hole injector into the organic hole transport layer [7]. The holes recombine in Almq$_3$ layer, releasing a photon. The electro-optical devices described above are either dependent on or greatly improved by the inclusion of ITO.

1.2.2 Other Applications

Outside of microelectronics, indium tin oxide has found uses in other industries, most notably, avionics. Due to its high transmission, ITO has been used as a defrosting mechanism on airplane cockpit windows [2]. A notable use of ITO is seen in the F-22 raptor fighter jet as a reflective coating on its canopy [10], the primary role of which is to minimize the reflection of radar waves and aid in detection avoidance.

ITO has also been used in thin film strain gauges that can withstand extremely high temperatures and harsh environments [11]. These gauges are rated for use in dynamic propulsion systems, such as gas turbines and rocket engines. The electrical, optical, and structural properties have shown the strong qualities of indium tin oxide, which has led to its widespread use in microelectronic devices, aircraft, and more. While there are a wide selection of ITO applications in microelectronic devices, the devices described above, specifically the solar cell, are most relevant to this work.

Chapter 2

ITO Characteristics

The widespread use of ITO results from a combination of its optical, electronic, and structural proprieties. In this chapter various aspects of these properties are described in detail.

2.1 Optical Properties

The optical properties of a material includes its Transmittance (T), Absorptance (A), Reflectance (R), and refractive index at a given wavelength. The transmission of a film is the percentage of incident light that passes through the film. Absorption of a film is the percentage of light or energy that is absorbed into the film. The Reflectance of the film is the percentage of incident light that is reflected away from the film and not transmitted nor absorbed. Since all three metrics are percentages that describe how the incident light interacts with the material, the sum of all three add to 1, as seen in Equation 2.1:

$$T + R + A = 1 \tag{2.1}$$

The transmission of a film can also be calculated using the thickness of the film and the material's absorption coefficient as seen in Equation 2.2: [12]

$$T = e^{-\alpha t} \tag{2.2}$$

where t is the film thickness and α is the absorption coefficient. The superscript α is determined by the extinction coefficient of the material, k, and the wavelength, λ, of the incident light. This can be seen in Lambert's Law of Absorption, Equation 2.3. [12]

$$\alpha = \frac{4\pi k}{\lambda} \tag{2.3}$$

The optical spectrum of ITO is characterized by high transmission in the visible spectra, an increasing Reflectance in the infrared, and high absorption in the ultraviolet, as shown in Figure 2.1. It is this high transmission in the visible range, 380 - 750nm, that is one of the most important characteristics of ITO for photovoltaic and display applications.

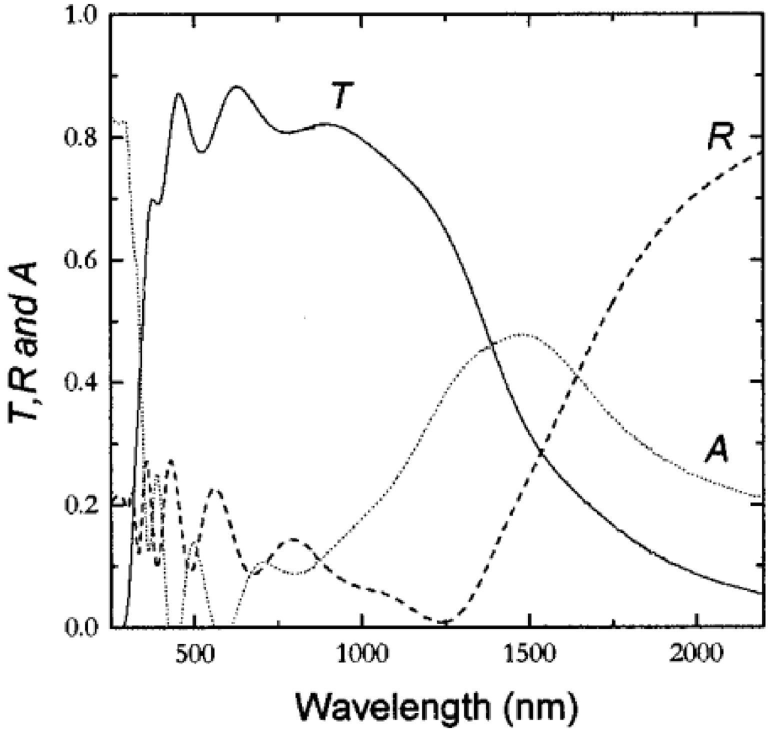

Figure 2.1: Typical Transmittance, Reflectance, and Absorptance for an ITO Film [13].

The extinction coefficient quantifies how quickly light is absorbed inside of a material and has been correlated to the oxygen content in a material [14]. The relationship between extinction coefficient, wavelength, and oxygen content can be seen in Figure 2.2. One method of altering the oxygen concentration of a material is by changing the oxygen partial pressure during the deposition. While the extinction coefficient exhibits a minimum around 450nm, Figure 2.2 illustrates an increased oxygen concentration in the material reduces k over the entire visible spectrum. This fact connects how the absorption, transmission, and extinction coefficient align with one another. As seen in Figure 2.1, around 450nm the transmission reaches its maximum while the absorption plummets to nearly zero. Since the absorption and extinction coefficient are directly correlated to one another, as seen in Equation 2.3, as the absorption decreases, so does the k value. This natural dip in k is exacerbated by the increased oxygen flow rate during deposition.

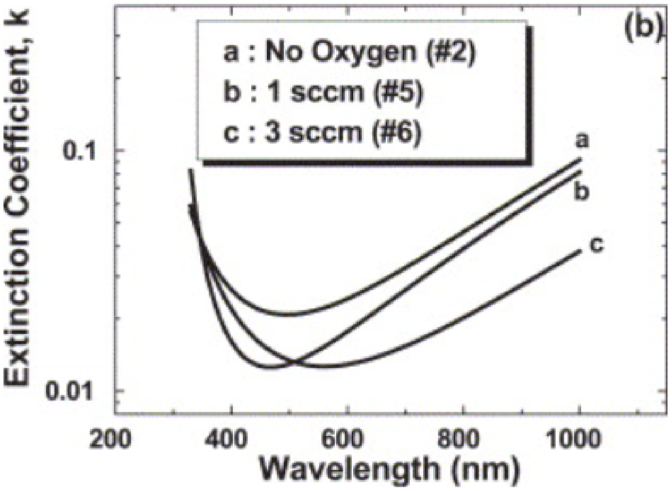

Figure 2.2: ITO Extinction Coefficient by Wavelength and Oxygen Flow [14].

The Reflectance of a film, a critical figure of merit for anti-reflective coatings, is dependent on the refractive index, n, of both the medium the light is traveling through and that of the film being measured. The Reflectance for a single interface can be calculated using Equation 2.4, where n_1 is the refractive index of the incident material and n_2 is the refractive index of the transmissive material.

$$R = \left(\frac{n_2 - n_1}{n_2 + n_1}\right)^2 \tag{2.4}$$

Using Equation 2.4, the Reflectance of an air, n_1 of 1, and silicon, n_2 of 4, Reflectance can be calculated, yielding a total value of 0.39. This Reflectance, as discussed in Section 1.2.1, can be minimized by introducing a third material with a refractive index that is inbetween air and Si, such as ITO which has a refractive index of 2. Therefore, when n_2 is 2, the Reflectance of the air to ITO interface is 0.11. For the ITO-Si interface, where n_1 is 2 and n_2 is 4, the Reflectance is also 0.11. While the sum of the air-ITO-Si Reflectances, 0.22, is already lower than the air-Si interface, 0.39, the internal reflection of the light that is initially reflected off of the Si surface back towards the substrate yields a much lower Reflectance. ITO's refractive index and its conductivity make it an ideal choice for optical applications.

Both the wavelength of the incident light and the elemental composition of the medium impact the refractive index. Figure 2.3 shows the impact of the incident wavelength on the refractive index of ITO, this is also known as dispersion. Typically, the refractive index will be cited at a specific wavelength for comparison to other mediums or when comparing the impact of other factors on n. Table 2.1 depicts the effect on n as the film composition changes by increasing SnO_2 weight%.

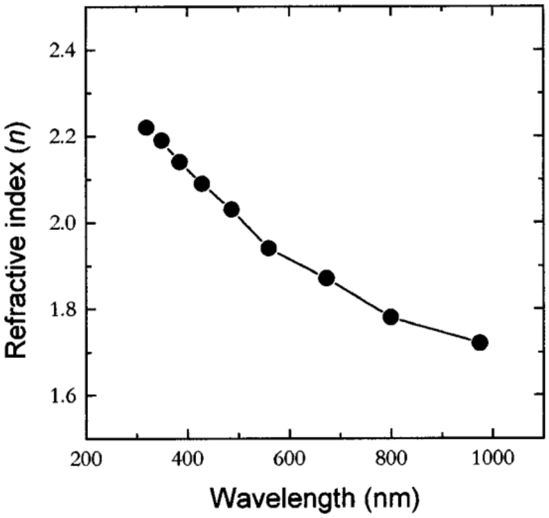

Figure 2.3: Refractive Index of ITO vs Wavelength. [7]

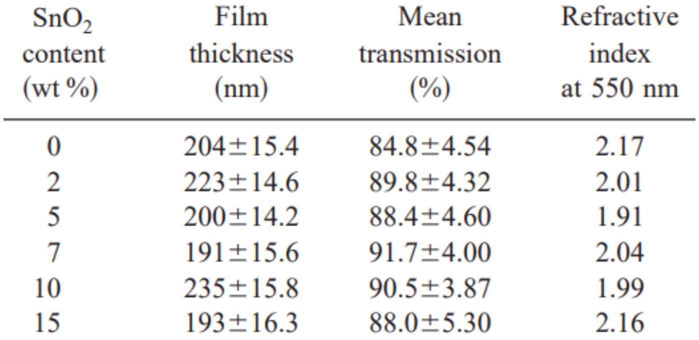

SnO_2 content (wt %)	Film thickness (nm)	Mean transmission (%)	Refractive index at 550 nm
0	204±15.4	84.8±4.54	2.17
2	223±14.6	89.8±4.32	2.01
5	200±14.2	88.4±4.60	1.91
7	191±15.6	91.7±4.00	2.04
10	235±15.8	90.5±3.87	1.99
15	193±16.3	88.0±5.30	2.16

Table 2.1: Impact of SnO_2 Content on Refractive Index. [7]

Note, a reference wavelength of 550nm was used to compare transmission and the refractive index. Depending on the application of the film, the reference wavelength will be relevant. The 550nm reference corresponds to the region in the solar spectrum with the highest energy [6] and is frequently cited for solar cells and light emitting diodes (LEDs).

Processing parameters, such as post deposition anneal, can have an impact of the measured refractive index and extinction coefficient. Figure 2.4 depicts the impact of different anneal steps and its impact on n and k for an ITO film.

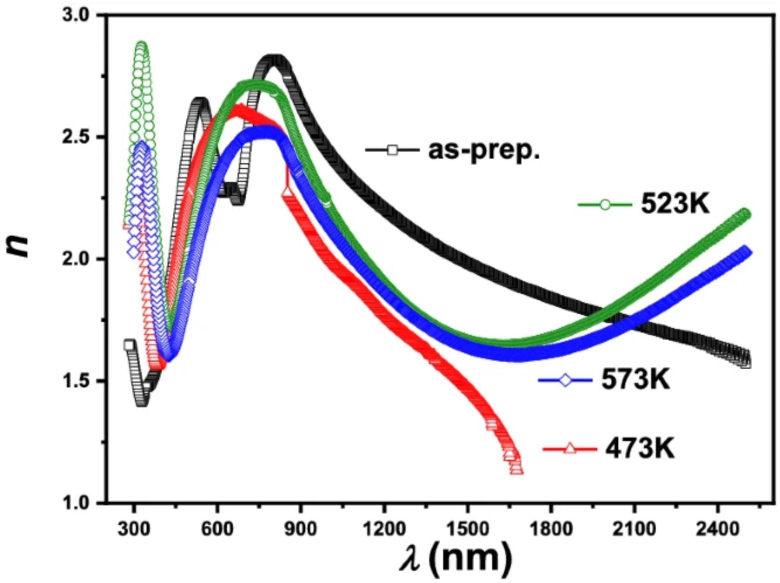

Figure 2.4: Impact of Post Deposition Anneal on Refractive Index [15].

While the refractive index of the ITO films prepared by Elnaiem et al [15] vary as the wavelength increases, its value in the visible spectra remains close to 2. The optical properties of indium tin oxide are one of its most desired features and a significant reason for its widespread and continued use. As seen from this partial review, there are many factors that impact the optical properties of ITO. The impact of varying deposition parameters, post deposition anneal, and wavelength on the films transmission, Reflectance, and other optical parameters will be further studied in Chapter 5.

2.2 Electrical Properties

The electrical properties of the ITO film, resistivity, carrier concentration, Hall mobility, and bandgap, describe how well the material conducts, the number of charge carriers, and how quickly the carriers travel through the material. These characteristics are heavily influenced by the crystal structure, deposition parameters, post-deposition anneal temperature, and elemental composition of the film. The above influences will be discussed in this section and expanded upon in Chapter 5.

The primary methods of conduction in ITO specifically, and TCOs in general, are the presence of oxygen vacancies, doping of another material, Sn in the case of ITO, and the presence of donor or impurity states close to the host (In_2O_3) conduction band [16]. As stated in Chapter 1, ITO is an n-type semiconductor which denotes the majority charge carrier, electrons. Conversely, a p-type semiconductor would have a majority charge carrier of holes. The number of charge carriers and how quickly they travel are factors that determine a key metric of a film, the resistivity.

The resistivity, ρ, of a film is an important metric to judge its quality and can also be expressed as conductivity, σ, the inverse of the resistivity. Thin films often have their sheet resistance, R_{SH}, measured, where the resistivity can be extracted from the R_{SH} value. The sheet resistance is the material's resistivity divided by the film's thickness, t. Sheet resistance is very useful when the material's resistivity varies with thickness, such as in an implanted or diffused film.

$$\sigma = \frac{1}{\rho} = qn\mu = q(\mu_n n + \mu_p p) \ \ [\Omega^{-1}cm^{-1}] \tag{2.5}$$

$$R_{SH} = \frac{\rho}{t} \ \ [\frac{\Omega}{\square}] \tag{2.6}$$

Equation 2.5 shows the conductivity as a function of mobility and carrier concentration, while Equation 2.6 shows the sheet resistance and resistivity relationship where t is the thickness, n and p are the concentrations of free carriers in cm^{-3}, μ is the Hall mobility, $\frac{cm^2}{V-s}$, and q is the fundamental charge of the electron with a value of approximately 1.6x10^{-19}C.

Carrier mobility is affected by lattice impurities, as these alter the lattice spacing and if ionized, can exert a Coulombic force on the free carriers. This results in a trade-off in terms of resistivity; increasing the number of impurities to increase n or p concentrations can degrade the mobilities. Figure 2.5 illustrates this trade-off and lists various experimental resistivity values of materials.

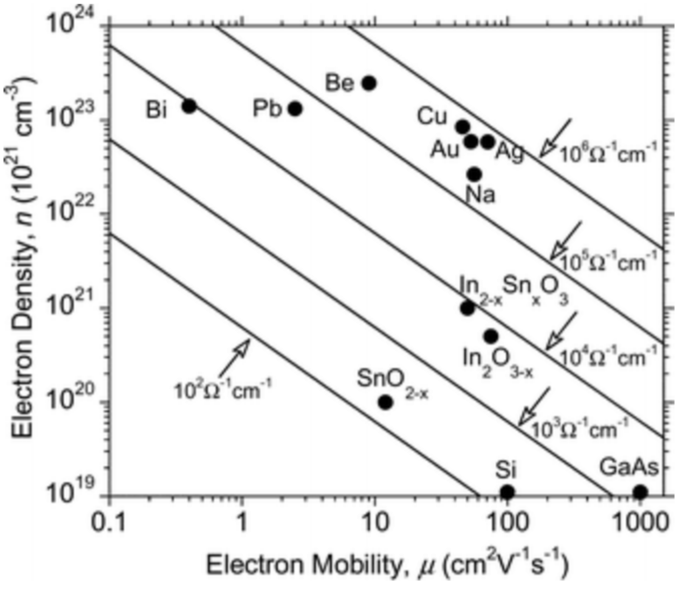

Figure 2.5: Conductivity of Various Materials by Carrier Concentration & Mobility [16].

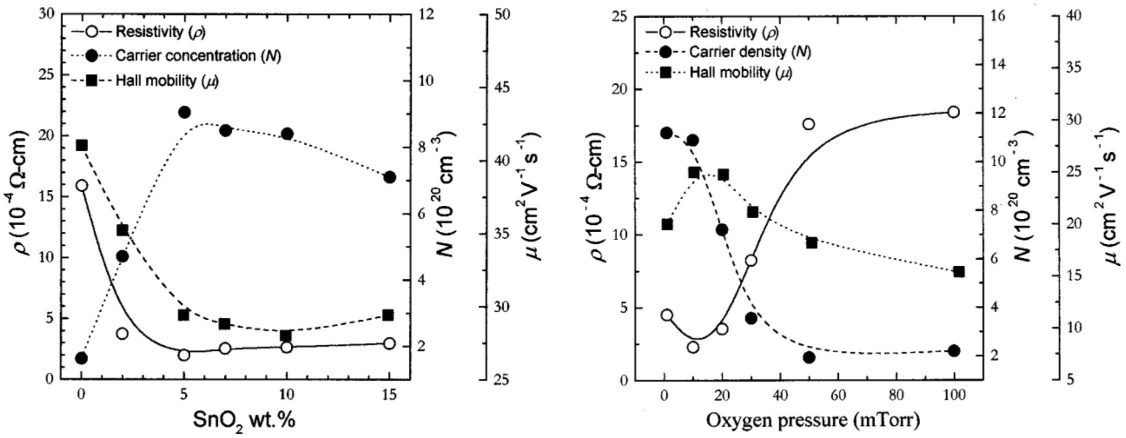

Figure 2.6: Sn Dopant and O_2 Partial Pressure Impact on ITO Resistivity & Carrier Properties [7].

Figure 2.6 captures some experimental results from an ITO deposition process. While increasing the amount of SnO_2 dopant in the ITO initially had a positive impact on the electron concentration and resistivity, it noticeably decreased the mobility of the electrons. Additionally, the resistivity reaches a minimum, before beginning to rise as the amount of Sn dopant increases. The increase in resistivity could be caused by an excess of Sn atoms, to the point where they no longer donate their electrons and instead form interstitial defects in the ITO lattice [7]. It has also been suggested that typically the Sn dopant atom must be surrounded by In_2O_3 molecules to successfully donate an electron. However, if there is an excess of Sn atoms in the ITO structure, then Sn atoms may interact with one another, negating their ability to donate electrons and instead becoming defects [17]. The impact of the O_2 partial pressure during deposition on resistivity shows a clear sweet spot around 10mT. Since oxygen tends to accept an electron, instead of donating one, any amount of excess oxygen will deplete the number of electrons and will result in a sharp increase in resistivity of the film, as it becomes more of a dielectric material instead of conducting.

The temperature at which the ITO film was deposited also has an impact on the carrier properties and resistivity, as seen in Figure 2.7. The positive impact a higher deposition temperature has on the electrical properties of the ITO can be attributed to a change in the crystalline structure of the film to a preferred orientation [7]. This change in crystal structure with temperature, in conjunction with the effects of the Sn doping, oxygen content, and deposition conditions signifies a challenge if one wishes to control the electrical properties of the film.

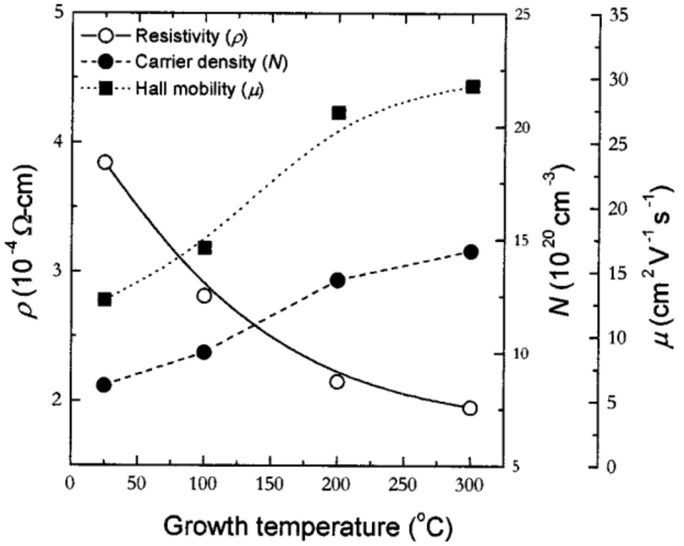

Figure 2.7: Impact of Temperature on Conductivity During ITO Growth [7].

This control also extends to both the electrical and optical bandgap of the film. The electrical bandgap is the amount of energy required to create a free electron-hole pair whereas the optical bandgap is the energy minimum for photons to be absorbed [18]. ITO is considered a large optical bandgap material, with a range of 3.8-4 eV [2]. The bandgap is dependent on the structure of the film and since the number of carriers can be altered through structural change, the bandgap can be as well.

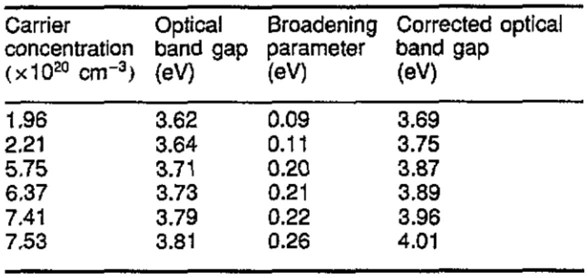

Carrier concentration ($\times 10^{20}$ cm^{-3})	Optical band gap (eV)	Broadening parameter (eV)	Corrected optical band gap (eV)
1.96	3.62	0.09	3.69
2.21	3.64	0.11	3.75
5.75	3.71	0.20	3.87
6.37	3.73	0.21	3.89
7.41	3.79	0.22	3.96
7.53	3.81	0.26	4.01

Table 2.2: Optical Bandgap for ITO at Various Carrier Concentrations [19].

Table 2.2 shows that as the concentration of carriers rises, the optical bandgap also increases. This effect on the bandgap can be explained by the Burstein-Moss (B-M) shift, where an increase in carrier density fills the lower levels on the conduction band, blocking the lowest states [20]. The B-M shift can be accounted for by adding a broadening parameter which is dependent on the concentration of carriers. The equations for these relationships can be seen in Equations 2.7 and 2.8 [20],

$$E_g = E_{g0} + \triangle E_g^{BM} \tag{2.7}$$

$$\triangle E_g^{BM} = \left(\frac{\pi^2 h^2}{2m_{vc}^*}\right)\left(\frac{3N}{\pi}\right)^{2/3} \tag{2.8}$$

where E_g is the corrected bandgap, E_{g0} is the bandgap of the undoped material, $\triangle E_g^{BM}$ is the B-M shift value, h is Planck's constant with a value of $4.135 \mathrm{x} 10^{-15}$ eV-s, N is the carrier concentration in atoms per cm^{-3}, and m_{vc}^* is the reduced effective mass of an electron [19].

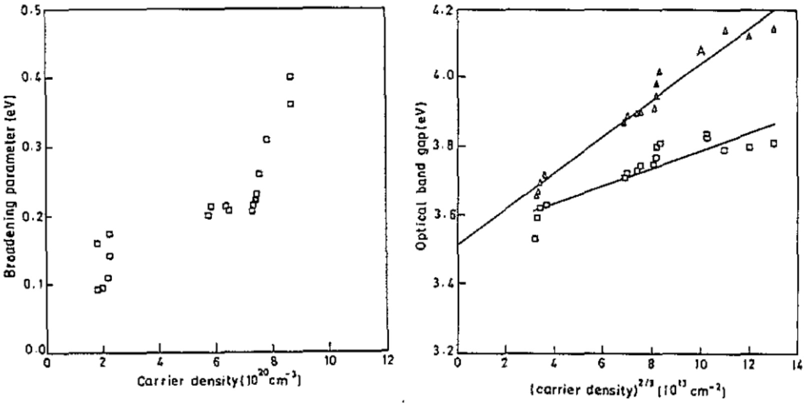

Figure 2.8: Impact of Carrier Concentration and B-M Shift on Optical Bandgap of ITO [19].

As shown in Figure 2.8, the expressed relationships in Equations 2.7 and 2.8 can be shown graphically to emphasize the impact of the B-M shift on the optical bandgap of ITO. Since the amount of carriers in the ITO film are directly impacted by the amount of Sn doping, as the Sn concentration increases, not only will the excess of Sn mitigate its own electron donor ability, but also increase the carrier concentration to the point of filling the lower conduction bands and thereby raising the bandgap.

The impact of the Sn doping on the band gap structure of the In_2O_3 gives ITO its unique carrier conduction properties. The parabolic nature of the lower conduction band in the In_2O_3 bandgap structure, depicted in Figure 2.9a, is caused by a combination of the indium 5s and oxygen 2s energy states. However, when the tin doping is added, the 5s energy state of the tin contributes to the conduction band, maintaining the parabolic shape and increasing the Fermi level into the conduction band, shown in Figure 2.9b. The unique parabolic shape and Fermi level of ITO allows it to behave as a degenerate n-type semiconductor or as a low-carrier-concentration metal while achieving a high transmission in the visible spectrum [21].

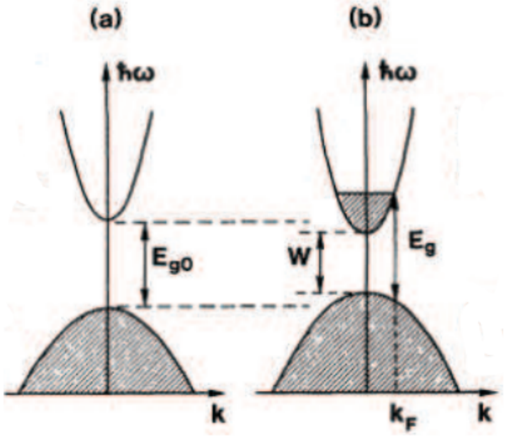

Figure 2.9: Bandgap Structure of In_2O_3 (a) & ITO (b) [21].

It is evident that all of the electrical and optical properties of ITO are impacted by its crystallographic orientation and other structural properties which are further discussed in Section 2.3. When all these factors are considered, the best films deposited in the literature have a resistivity of $10^{-4}\Omega$-cm and transmission of 90.6% [19].

2.3 Structural Properties

The structural properties of ITO have a significant impact on the electrical and optical properties of the film [19, 7, 17]. Listed in Table 2.3 are the common values for some of the properties of ITO. The films used to collect the Young's modulus, Poisson ratio, and stress were sputtered and consisted of 10wt% SnO_2 and the thickness of the film used in the tensile strength testing was 105nm. While these values are not constants and may change with the deposition process and subsequent heat treatments of the sample, they do provide a point of reference for comparison.

Table 2.3: Physical Properties of ITO.

Property	Value	Unit
Density [22]	6.8	g/cm^3
Young's Modulus [23]	116	GPa
Poisson Ratio [23]	0.35	-
Tensile Strength [24]	0.022	-
Stress [22]	-2.1 - -2.3	GPa

Post deposition, ITO films are primarily arranged in a body centered cubic (BCC) crystal structure but, as the Sn doping level increases above 6wt%, rhombohedral (RH) orientations also begin to form [25]. Figure 2.10 illustrates this orientation for both indium (IO) and indium tin oxide (ITO).

As the Sn atoms are added to the IO structure in Figure 2.10, the lattice adjusts to conform to the additional dopants. This adjustment can be seen in the creation of oxygen dimer and trimer as well as additional In atoms at the surface of the structure. This new crystal formation allows for the Sn dopants to donate their electrons, giving ITO its sought after conductivity. This shift also effects the lattice constant, a_0, which is the distance between the two corners of a unit cell for an atomic structure. ITO has an ideal lattice constant of 10.118Å, but the crystal plane, lattice strain, post deposition anneal, and Sn doping concentration can all impact this value, creating a range from 9.97Å to 10.24Å [26, 27, 7].

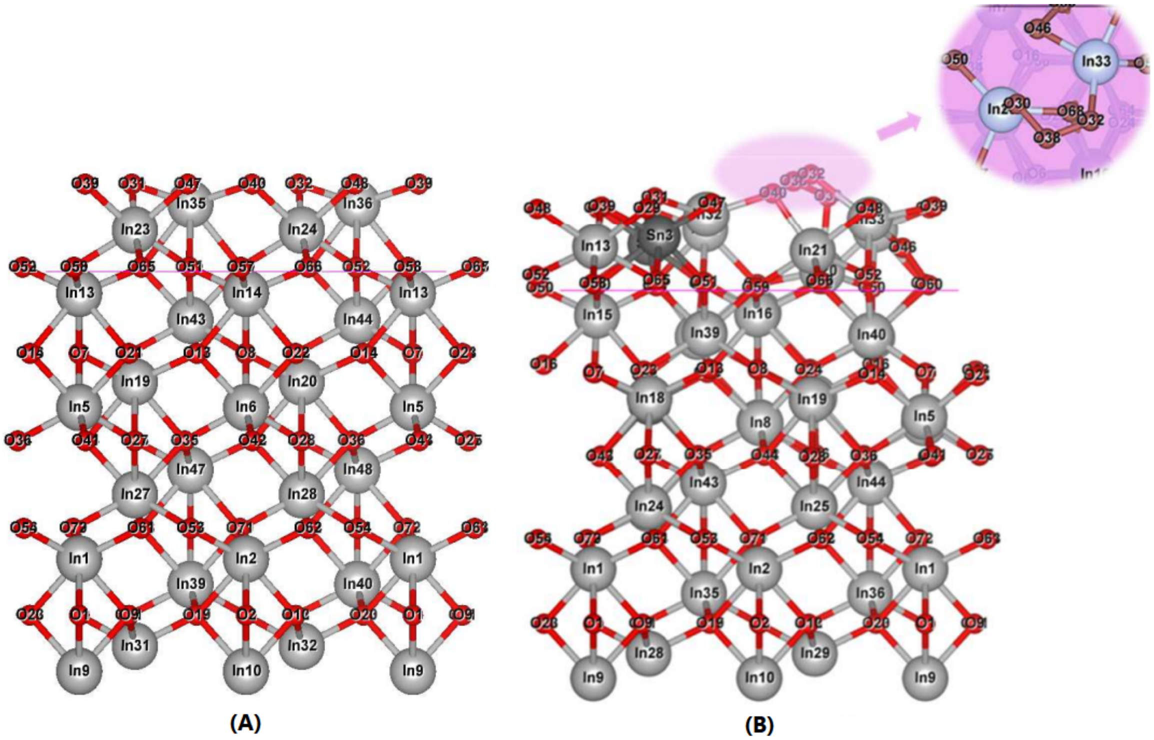

Figure 2.10: Rhombohedral Indium Oxide and Indium Tin Oxide Atomic Structure [25].

The crystallographic planes of ITO are also tied to its conductivity and are impacted by the deposition parameters, anneal temperature, and Sn doping concentration as shown in the XRD spectra in Figure 2.11. As can be seen, ITO has an XRD pattern exhibiting peaks at approximately 30, 35, 50, and 61 degrees assigned to the (222), (400), (440), and (622) planes respectively. The (222) and (400) planes in particular have been correlated to decreased resistivity and carrier mobility as well as increased carrier concentration [28]. The method used to collect crystallographic plane data, X-ray diffraction, will be discussed in Chapter 4 and the impact of deposition and anneal parameters on the orientations of the film will be further elaborated on in Chapter 5.

A unique feature of ITO is its ability to withstand compressive and tensile stress without failing. This makes it a favored material when paired with polymer substrates for use in flexible flat panel displays and organic solar cells [29]. A common polymer substrate used in these applications is polyethylene terephthalate (PET). It has been shown that an ITO/PET device stack can withstand hundreds of bending cycles without cracking or large changes in resistance while maintaining good adhesion to the PET substrate [30].

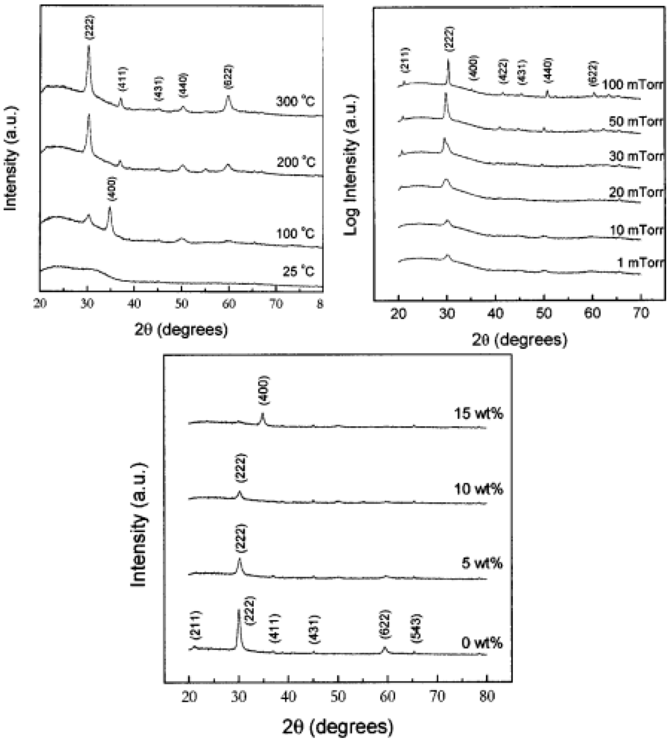

Figure 2.11: Impact of Sn Doping, O_2 Partial Pressure, and Anneal Temperature on Preferred Orientations [7].

One of the chief properties of ITO that sets it apart from its TCO competitors is its etchability, with the ability to achieve sharp lines and features [2]. In terms of wet etching, the following chemicals have been used: Oxalic acid, $C_2H_2O_4$, with slight agitation; Hydrochloric acid, HCl; Hydrobromic acid, HBr; Mixtures of HCl and HBr with nitric acid, HNO_3 [31, 32]. ITO was also plasma etched using a gas flow of $5CH_4/15H_2/20Ar$ with the fastest etch rate occurring with high RF power and higher etch pressure [33]. The combination of favorable transmission, conductivity, and etchability makes ITO a widely used material in microelectronic or display applications. In Chapter 3, a review of the various deposition techniques used to deposit ITO films is undertaken.

Chapter 3

Deposition Techniques

Indium tin oxide is most used as a thin film and will be investigated as such in this work. Thin film deposition techniques are generally broken down into two separate categories, physical vapor deposition, PVD, and chemical vapor deposition, CVD. Beyond these two categories, there are numerous CVD and PVD forms such as spray pyrolysis, atomic layer deposition, molecular beam epitaxy, evaporation, and sputtering. The pros and cons of these techniques will be discussed with an emphasis on sputtering.

3.1 Vacuum Systems

Most of the deposition techniques discussed in this chapter rely on a vacuum system to pump out the ambient atmosphere, creating a controlled environment where deposition can occur. Figure 3.1 highlights the necessary segments of a vacuum system. The roughing valve, line, and pump are utilized for lowering the pressure of the processing chamber from atmosphere, 760 Torr, down to a crossover pressure, typically around 40 to 100 mTorr.

At that crossover pressure, the roughing valve will close, preventing any back flow from the rough pump into the chamber. If using a hi-vac pump or a displacement pump (oil diffusion or turbo-molecular), the foreline valve will open so the rough and hi-vac pumps are in series. If it is an entrainment pump (cryogenic or ion) the rough pump can be turned off. The hi-vac valve will open and the processing chamber is evacuated down to its base pressure, between 10^{-6} to 10^{-7} T. The isolation the valves provided for each pump are crucial. If the hi-vac valve opens at too high a pressure, then the large flow of gas could damage the pump. If the roughing valve stays open while the chamber is pumped down to a low pressure, then the oil used to lubricate the pump could flow back through the now mostly empty roughing line and contaminate the chamber. Chamber cleanliness depends upon proper pumpdown operation.

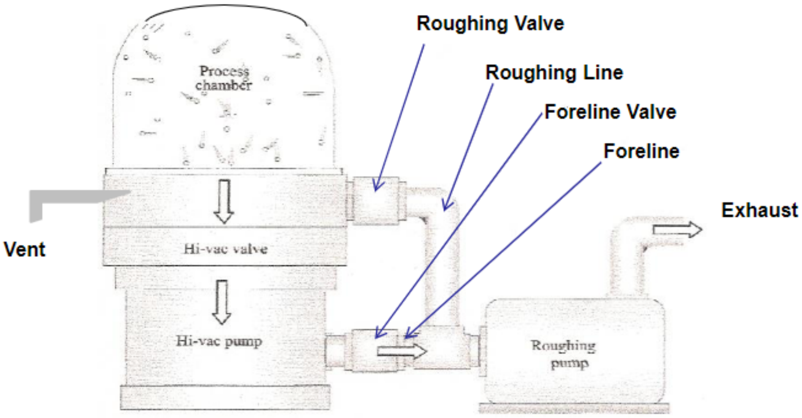

Figure 3.1: Layout of A Basic Vacuum System [34].

In Figure 3.2 are visual representations of the different flow regimes. The bottom graphic in Figure 3.2, illustrates the molecular flow regime, when the mean free path length of the gas is greater than the diameter of the pipe. Therefore, the gas is more likely to collide with the pipe itself than other gas molecules. This is the reason why oil from the rough pump could back flow into the processing chamber, as mentioned above. In the viscous flow regime, if oil made it back into the roughing line, the gas molecules would collide with, and direct, it back into the pump.

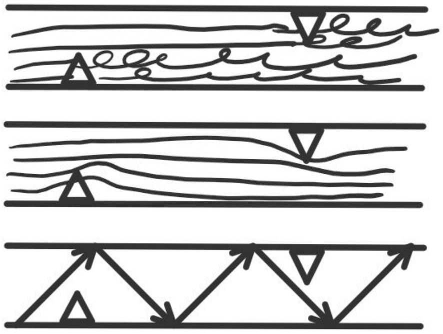

Figure 3.2: From Top to Bottom: Turbulent Viscous, Laminar Viscous, and Molecular Flow Regimes.

The top two graphics in Figure 3.2 show the difference between the laminar and turbulent flow. Laminar flow is characterized by smooth, streamlined gas flow whereas turbulent flow consists of chaotic eddy currents. Successful operation of the vacuum system requires the crossover from the rough pump alone, to the high vacuum pump, with or without the rough pump, to occur before the transition from laminar to full molecular flow is completed. Because the transition occurs over two orders of magnitude in pressure, a 40 to 100 mT crossover range is used.

3.2 Chemical Vapor Deposition

CVD is a thin film deposition technique that relies on using precursor chemicals reacting in gas form and adhering to the wafer surface. These reactions can be described by the species involved in the reaction. A reaction that happens between the gas molecules and the substrate's surface is a heterogeneous reaction, whereas one that occurs between two molecules in the ambient is a homogeneous reaction. Heterogeneous reactions are more favorable and produce higher quality films than homogeneous ones, which may be plagued by particulate formation in the ambient, which upon incorporation into the film can lead to poor adhesion, lower density, and higher defects [35].

There are five basic reactions that can take place to generate a film: pyrolysis, where heat is used to make a compound decompose; photolysis, which uses radiant energy to break bonds and cause a compound to decompose; reduction, a reaction that results in the gain of an electron; oxidation, a reaction that results in the loss of an electron; and reduction-oxidation(redox), reactions which combines reduction and oxidation [34].

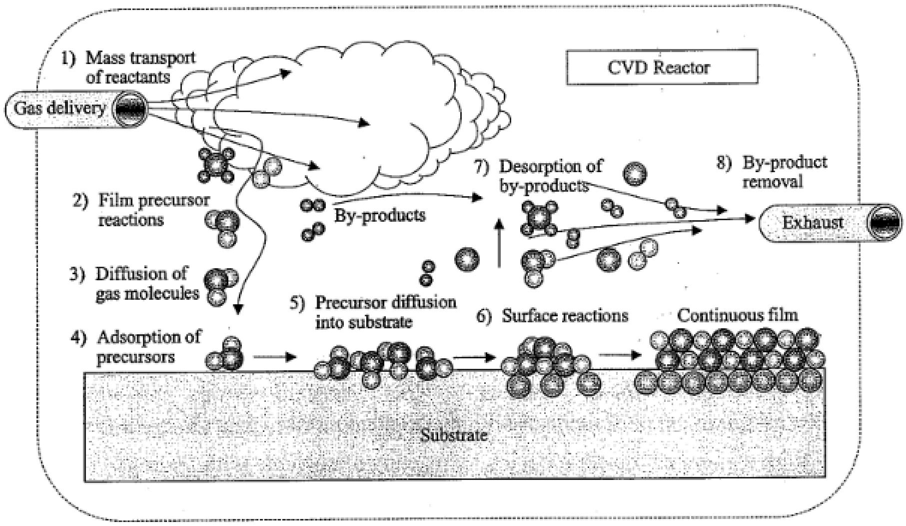

Figure 3.3: Reactions Steps Involved in Chemical Vapor Deposition [34].

Figure 3.3 illustrates the 8 general reaction steps involved in a CVD process. Firstly, the reactants are introduced into the CVD reactor in a gaseous form. Next, the different reactants interact with one another forming the molecules that will make the film, the precursors. The precursors then diffuse towards the wafer surface. Once these molecules reach the surface, they adsorb, react, diffuse across the surface, and collect at film nucleation sites. When the precursors react with one another, by-products are generated. The by-products on the surface desorb and join the ambient. Finally, all of the by-products and unreacted precursors are transported out from the reactor. The speed at which this process occurs is dependent on its slowest step out of the 8 described above. While increasing the temperature of the substrate can increase the reaction rate, generally the speed at which the gaseous reactants arrive at the wafers surface dictates the growth rate [34]. The steps described above are fairly general and apply to all of the CVD techniques to be discussed.

3.2.1 Spray Pyrolysis

Spray pyrolysis is a method where precursor chemicals are sprayed onto a heated substrate at atmospheric pressure, where they react and deposit a thin film. The substrate is typically kept at or above 400°C, which is used to provide energy and drive a chemical reaction between the precursor chemicals. These chemical constituents typically contain a solvent that is used as a carrying agent for the reactants prior to the reaction. The primary components used in spray pyrolysis are a spray nozzle, liquid flow meter, gas flow controller, and a temperature controller arranged as shown in Figure 3.4.

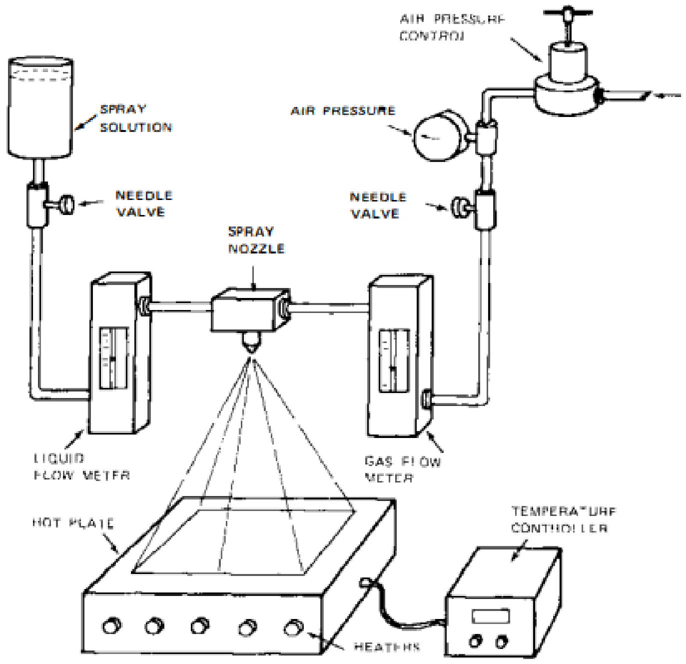

Figure 3.4: Basic Arrangement of A Spray Pyrolysis Tool [36].

In order for the liquid chemical precursors to be sprayed onto the substrate, they first need to be propelled by a compressed gas. Considerations need to be taken when choosing a gas propellant as some, such as oxygen, could cause unwanted interactions between the precursors or the film itself

[36]. The compressed gas and the liquid chemicals it carries are applied to the substrate, which is heated through a hotplate or other means. The heated constituents undergo a chemical reaction and form the desired compound on the surface. There are two primary reaction processes that are used when discussing spray pyrolysis, either the sprayed chemicals sits on the surface while any solvents are evaporated, leaving behind a solid that could still react, or the solvent evaporates before reaching the substrate and the powder that remains lands on the surface and begins to decompose [36]. Ideally, any by-products from this reaction are desorbed and are carried away from the reaction area using ventilation systems.

When using spray pyrolysis to deposit ITO films, the precursors typically used are tin(IV) chloride, $SnCl_4$, and indium(III) chloride, $InCl_3$ with a substrate temperature between 350 to 600°C. These precursors are combined with a methanol-water mixture, methanol was chosen due to its high volatility and water is necessary to form the indium and tin oxides [37]. When this mixture is applied to a high temperature substrate, the following reactions take place: the methanol evaporates, leaving the tin and indium chlorides and water; the tin chloride and indium chloride react with the water to form tin oxide, SnO_2, and indium oxide, In_2O_3, respectively. The reaction equations are as shown: $SnCl_4 + 2H_2O \rightarrow SnO_2 + 4HCl$ and $2InCl_3 + 3H_2O \rightarrow In_2O_3 + 6HCl$. Since these films are deposited at a high temperature, the resulting film typically does not require any post-deposition anneal steps and its conductivity is $3\text{x}10^{-4}\Omega$-cm, and is 90% transparent at 450nm [37].

While the tool in Figure 3.4 looks simple, there are a number of different variables that all have a drastic impact on the deposited film. These variables include the ambient temperature, carrier gas flow rate, distance between the spray head and substrate, radius of the spray droplet, type of spray nozzle head, reactant concentration, reactant flow rate, and substrate temperature [36]. While these variables can be fine tuned to allow for great control of the deposited film, some issues or defects in the film could be difficult to trace back to a specific source. Some advantages of spray pyrolysis over other CVD techniques are as follows: the speed that films can be deposited, which can be around 4 cm^3 per minute; its relatively easy setup; its cost-effectiveness, since little of the reactants is wasted and does not require a vacuum system; and the uniform films it produces. However, spray pyrolysis' dependence on a high temperature limits its useful for processes with a low thermal budget or with materials that are sensitive to higher temperatures. Additionally, some of the chemicals used as precursors or their by products can be dangerous and require special handling, ventilation, and disposal. For example, tin(IV) chloride is a strong irritant, is corrosive, and was used as a chemical weapon in world war I [38] and its by product, hydrochloric acid, can cause serious skin burns.

3.2.2 Atomic Layer Deposition

Atomic layer deposition (ALD) is a form of CVD where precursor chemicals are individually used to grow a film atomic layer by atomic layer, allowing for extremely thin and precise film thicknesses and compositions. Usually, there are two reactant compounds used to form the monolayer. This process is broken down into individual steps, each taking a few seconds. An example of these steps and their functions are shown in Figure 3.5. The ALD process begins with a heated clean substrate, with only OH bonds available at the surface. The system is pumped down to a low base pressure to ensure purity before introducing nitrogen as a carrier gas to achieve a specified deposition pressure. The first reactant is then added into the chamber, which reacts with the surface. In the case of $Al(CH_3)_3$, the Al bonds with the oxygen, generating CH_4, which is volatile. The excess reactants are purged. Next H_2O is pumped in, reacting with the $(CH_3)_2$, to create volatile CH_4 and complete the layer with a new OH bond for the next layer to grow from. This process is self limiting, with the result being the growth of a single layer of Al_2O_3. The cycles can be repeated to achieve a desired thickness with great precision.

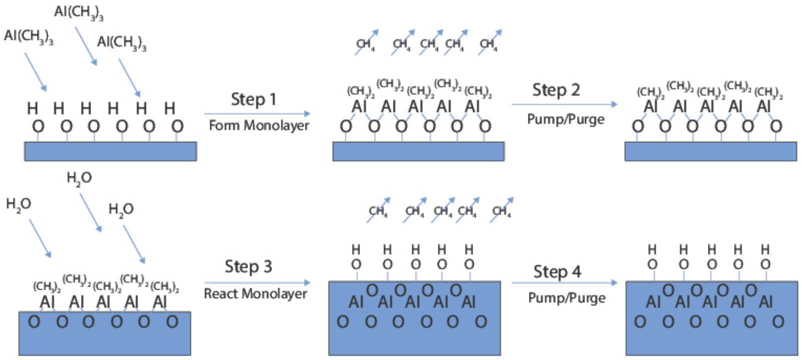

Figure 3.5: The Reaction Cycles In a Typical ALD Process [39].

Since ITO is comprised of tin oxide and indium oxide, the ALD is done in staggered layers. In other words, both the indium oxide and tin oxide are grown as individual layers stacked on top of one another. The ratio of SnO_2 to In_2O_3 can be altered by growing more layers of one oxide than the other. Common precursor reactants for tin oxide is Tetrakis(dimethylamino)tin(IV), TDMASn, and either hydrogen peroxide, H_2O_2 at 150°C, or H_2O at 225°C. TDMASn has a chemical formula of $Sn(N(CH_3)_2)_4$. Indium oxide was grown using either cyclopentadienylindium(I), C_5H_5In, with ozone, O_3, at 150°C or trimethylindium, TMIn, with H_2O at 225°C. TMIn has a chemical formula of $In(CH_3)_3$ [40, 41]. The deposition process using both sets of precursors can be seen in Table 3.1:

Table 3.1: ALD Processes To Deposit ITO.

Process	Film	Step Num	Gas Flow	Duration [s]	Temperature [°C]
Process 1 [41]	SnO_2	1	TDMASn	2	225
		2	N_2	-	
		3	H_2O	1	
		4	N_2	-	
	In_2O_3	1	TMIn	0.625	
		2	N_2	-	
		3	H_2O	0.75	
		4	N_2	-	
Process 2 [40]	SnO_2	1	TDMASn	1	150
		2	N_2	5	
		3	H_2O_2	1	
		4	N_2	5	
	In_2O_3	1	InCp	2	
		2	N_2	4	
		3	O_3	2	
		4	N_2	2	

While ALD can achieve extremely precise films at a relatively low temperature, this process occurs slowly. As shown, in Table 3.1, in process 2, a complete cycle of both indium and tin oxides takes 22 seconds to deposit around 3 Åof material [40]. Additionally, since the surface of the wafer needs to be very clean and clear of native oxide, great care needs to be taken to clean the wafer, usually coming at a higher cost. Another disadvantage of ALD is the limitations of viable precursors, for example, the chemicals used for Si, Ge, and Si_3N_4 ALD are expensive and may not be cost effective for use in manufacturing [42].

3.2.3 Molecular Beam Epitaxy

Epitaxy is a form of CVD that deposits a single crystal thin film, an epilayer, that matches the crystal structure of the substrate using high temperature. Molecular beam epitaxy, MBE, is a form of epitaxy that operates under a high vacuum, 10^{-10} to 10^{-11} Torr, and a temperature of 500 to 900°C. Where other forms of CVD and epitaxy depend on a high flow of gas reactants to form a film, MBE utilizes a beam of sputtered or sublimed molecules to deposit a film. Sputtering is discussed in Section 3.3.2. Sublimation is a process where a material transitions from a solid state directly to its gaseous state. While this beam of molecules limits the growth rate in comparison to other CVD techniques, it allows for uniform, atomic-layer-by-atomic-layer deposition of single crystal films [43]. MBE can also be used to dope the film being grown. An example of a MBE system is shown in Figure 3.6, where there are three source ovens for variable film compositions. Shutters can be used to instantaneously cut off the molecular beam from any of the three source ovens, allowing for precise thickness control and the ability to change the material or dopant being deposited. Surrounding the source ovens are liquid nitrogen cooled panels, which serve as condensing surfaces and help form the beam of molecules. The RHEED gun and screen (reflection high energy electron diffraction) is an analytical technique where electrons are fired at a glancing angle across the films surface. The reflected electrons collide with a phosphorus coated screen, yielding real time crystallinity data that allows for in-situ analysis as the film is grown. This feature coupled with the shutters immediate response time allows for great control and uniformity of the deposited material. The primary downsides of this technique are the slower deposition rates, costs associated with an ultra high vacuum environment, and a limitation on substrate size.

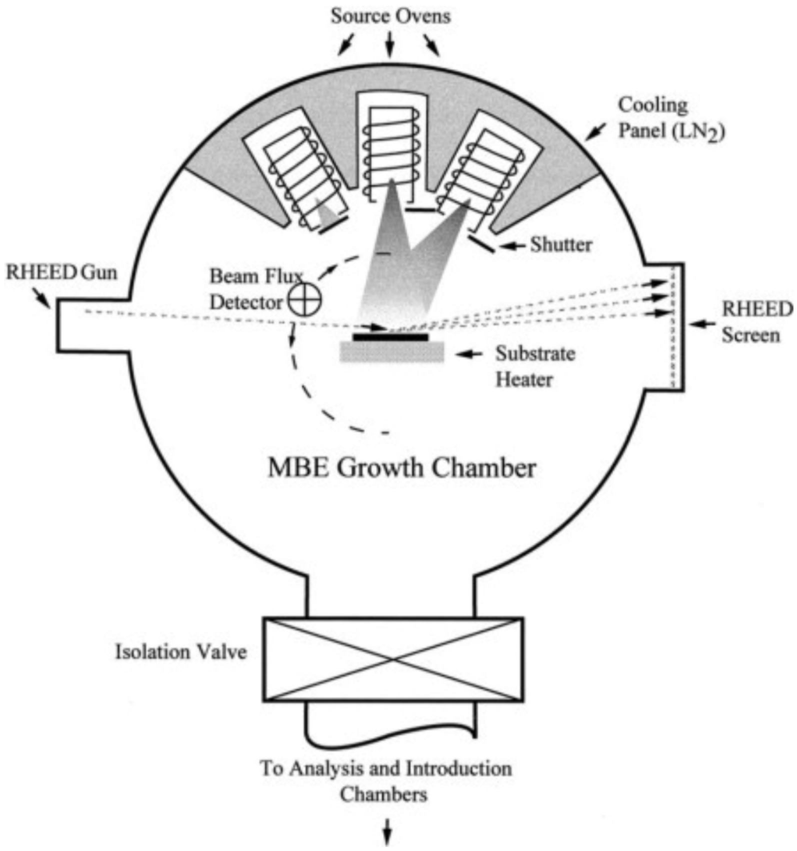

Figure 3.6: Molecular Beam Epitaxy System Cross Section [43].

Indium tin oxide films have been grown using MBE with a 9:1 In_2O_3:SnO_2 ceramic source [44]. The MBE system used had a base pressure of 10^{-8} Torr, substrate temperatures between 200 to 400°C, and varied deposition pressures from 0.01 to 0.1 Torr. The impact of the growth conditions were monitored using the RHEED screen shown in Figure 3.7.

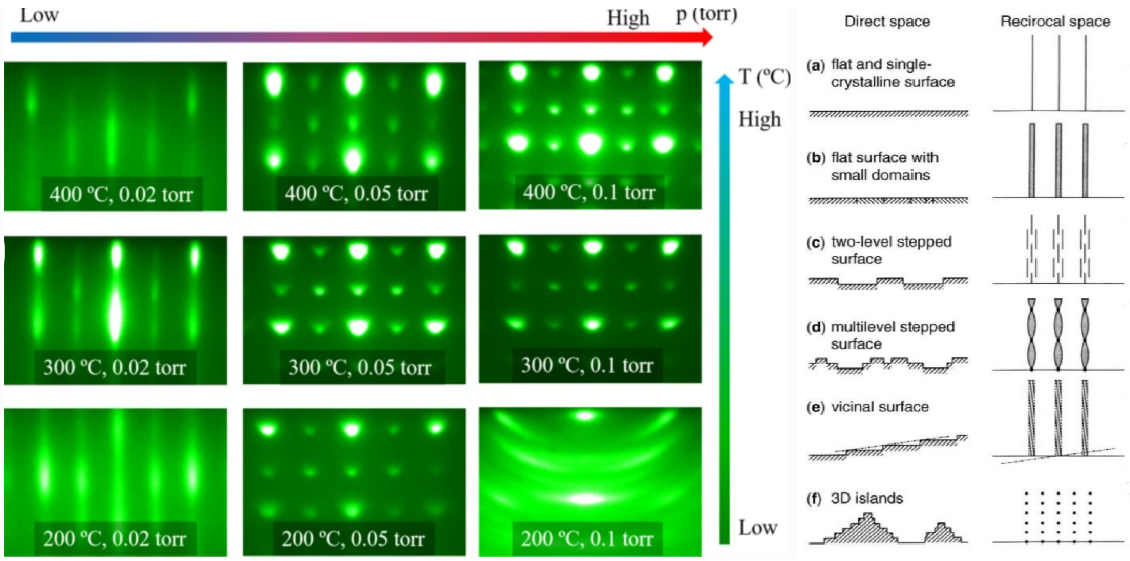

Figure 3.7: RHEED Screen Display of ITO Films Grown Under Different Conditions & A Key to Interpreting RHEED Screen [44, 45].

Where the diffraction patterns signify various crystal structures. The guide in the figure on the right shows how the surface of the film correlates to the reflected image. The ideal film is a flat, uniform surface which correlated to even lines and spaces in the RHEED screen. Using this guide, the best deposition conditions for ITO using MBE is a high temperature, low pressure chamber. The high temperature allows for greater diffusion of the ITO adatoms while a high pressure leads to a rougher surface and reduced uniformity. ITO thin films grown via MBE have been shown to have consistently high transmission, 95%, and sheet resistance values ranging from 40 to 400 $\frac{\Omega}{\Box}$ [44].

3.3 Physical Vapor Deposition

Physical vapor deposition, PVD, is a thin film deposition technique that requires a solid target or starting material that is then turned into a gaseous form which diffuses and then condenses on a substrate. Similar to CVD, PVD has many different forms, however, only evaporation and sputtering will be discussed, with the focus on sputtering as it is the deposition technique used in this work.

3.3.1 Electron Beam & Resistive Heating Evaporation

Evaporation is the process of heating a source material to its vapor-pressure point, where it enters the gas phase, diffuses, and coats the inside of the chamber and substrates in the source material when it condenses. The evaporation chamber, usually a bell jar, is always pumped down to a low base pressure to avoid unwanted interactions between the ambient and evaporated molecules. The evaporation can be performed either at the base pressure or a pure gas can be introduced into the chamber with the intention of it interacting with the evaporated material. This process of desired gas-molecule interactions is known as reactive evaporation. In the case of ITO, an oxygen evaporation ambient is frequently used to achieve more desirable film properties.

The two most widely used methods of evaporation are electron beam (e- beam) and resistive heating evaporation. An e- beam tool passes a directed beam of electrons through the source material, whereas resistive heating evaporation uses a resistor to hold the source material, and indirectly heats it. Figure 3.8 is a side to side comparison of an e- beam and resistive heating evaporators.

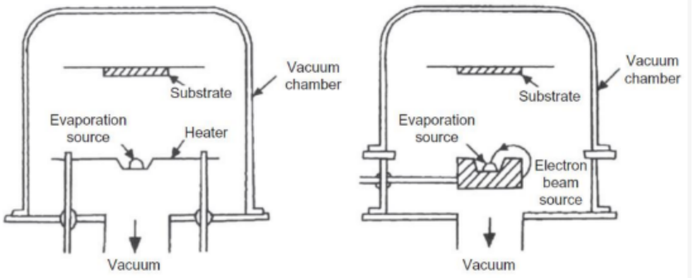

Figure 3.8: Thermal Evaporator (Left) vs Electron Beam Evaporator (Right) [46].

Overall, the two systems have a fairly similar configuration, with a multi-substrate holder that is capable of rotating for added uniformity. Both systems also have the capability to contain multiple sources, which allows for either different material or a larger amount of one material to be evaporated at a time. The primary difference is the method of heating the source material. Thermal evaporation uses a simple metal crucible, usually made of molybdenum, tungsten, or tantalum [46], that can withstand high temperatures. Achieving a moderate deposition rate of 10-100 nm/min, thermal evaporation is typically inexpensive and is suitable for large scale manufacturing. The primary limitations is the uniformity of the deposited films and the small range of materials that can be evaporated thermally [46]. The e- beam evaporation achieves a higher energy output than resistive heating evaporation, and can therefore vaporize a wider range of materials at a greater efficiency. While e- beam is a more expensive technique, the greater power output of the electron beam allows for a faster deposition rate. That being said, the decision to use resistive heating or e- beam evaporation typically comes down to the material being vaporized, if the material has a high vapor pressure, then resistive heating evaporation is typically used and vice versa for a material with a low vapor pressure.

Evaporation of alloys and compounds can be challenging, especially if the vapor pressure of the various elements differ greatly. With resistive heating, the element with the lowest vapor pressure will evaporate first, preventing the proper stoichiometry in the film from being achieved. The higher power in the electron beam reduces this effect, but does not eliminate it. For this reason, sputtering is often preferred for alloys and compounds.

When evaporating ITO, the source materials used are either metallic InSn or ceramic indium oxide and tin oxide, usually with a 10% SnO_2 composition [19]. It is common to either anneal the evaporated ITO films or deposit them onto heated substrates. For example, films that were deposited via e-beam evaporation in an oxygen gas at a temperature of 225°C yielded highly conducting and transparent films, 2.5x$10^{-4}\Omega$cm and 92% transmission at 500nm.

3.3.2 Sputtering

Sputtering is physical vapor deposition via momentum transfer between an ionized atom and a target atom. Seen in Figure 3.9 are the two primary methods of sputtering, sputtering via a DC bias or an RF source.

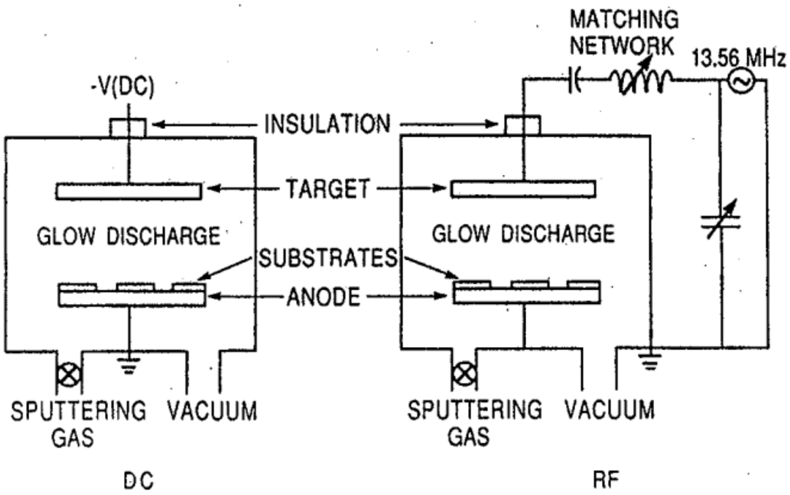

Figure 3.9: Cross Section of A Basic DC (Left) and RF (Right) Sputter System [47].

The basic components of a sputter system are the target cathode, a rotatable substrate holder anode, and the vacuum system. Two additional, and vital, components not shown are the shutter, which is a movable shield that slides in between the target and substrate which prevents deposition, and the throttle valve. The shutter is primarily used during the presputter, blocking any sputtered material from collecting on the substrate. The presputter is a preliminary step done prior to deposition to clean the target surface of any oxides or other contaminants that may have collected while the substrates were being loaded. The throttle valve is placed between the processing chamber and the high vacuum pump, controlling the rate that the gas in the processing chamber is removed by the hi-vac pump. In this manner, a range of processing pressures can be achieved from the same gas flow, reducing wear on the hi-vac pump.

In order to understand sputtering, first the plasma used to enable this process must be discussed. A plasma is an electrically neutral region of partially ionized gas. The gas, typically argon, contains free electrons which are acted upon by an electric field. These electrons are drawn towards the anode, gain momentum, and collide with the process gas. These collisions can result in different interactions, as shown in Table 3.2 [48]:

Table 3.2: Results of Collisions in Sputtering Plasma.

Label	Reaction
Simple ionization	A + e^- $\rightarrow A^+ + 2e^-$
Excitation	A + $e^- \rightarrow A^* + e^- \rightarrow A + e^- + hv$
Recombination	$A^+ + e^- \rightarrow A$
Attachment	$A + e^- \rightarrow A^-$
Dissociation	$AB + e^- \rightarrow A + B + e^-$

The reactions listed in Table 3.2 occur when an inelastic collision takes place between the molecule and electron. Multiple reactions can occur at once. For example, dissociative ionization result in the following: AB + e^- $\rightarrow$ A + B^+ + $2e^-$, where molecule AB collides with an electron, the molecule separates into A and B, with B being ionized as well. For sputtering, ionization is most desired since the generated ion can be directed into the cathode target, releasing target material, and generating electrons that replenishes any electrons that are lost at the anode. The generated electron is also referred to as secondary electron emission, to distinguish it from the primary electrons that exist in the ambient.

Other methods of sputtering, such as rf and magnetron sputtering, have been developed to improve the efficiency of the process. RF sputtering uses an RF source instead of a DC that allows for sputtering of insulating materials that do not emit second electrons. Magnetron sputtering uses magnets place beneath the target to generate an additional magnetic field in the plasma. This field causes the electrons to travel in a helical motion, increasing the distance they travel and causing more collisions. This raises the efficiency of the ionization process thus increasing deposition rates. The downside to this method is the creation of racetracks on the targets surface. The race track, seen in the shallow regions of the target in Figure 3.10, is an area of preferential sputtering caused by the added magnetic field. As the racetrack grows deeper, the deposition rate can be affected and the target can be worn down prematurely, ultimately requiring replacement.

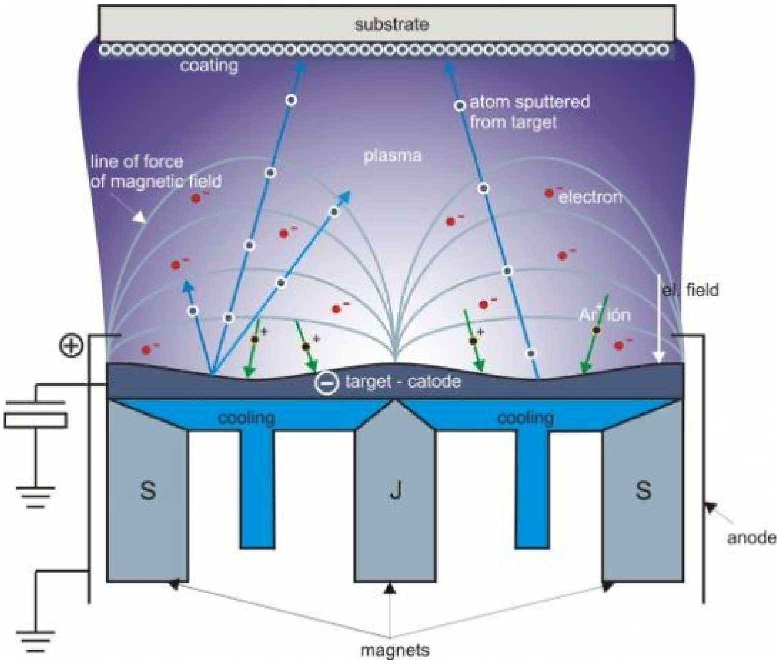

Figure 3.10: Magnetron Sputtering Diagram [49].

Similar to the gas molecule and electron interactions, the interaction between the ion and the target can result in a few different reactions. As the positively charged ion is propelled by the electric field into the target anode, the ion can reflect back (backscatter), reflect back as a neutral, stick (adsorb), implant (absorb), or forward scatter. Upon collision, the momentum of the ion could cause the target atoms to be ejected, secondary electrons can be emitted, or cause some other physical or chemical effect [48]. The ideal reaction between the ion and the target would be for the ion to bounce off or be re-emitted from the target so that it can reenter the plasma and possibly be re-ionized. Depending on the energy of the ion, it can enter and interact with the target as depicted in Figure 3.11:

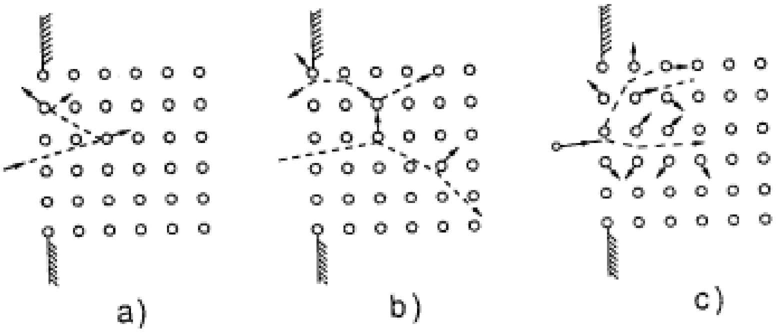

Figure 3.11: Different Ion-Target Interactions Depending on the Energy of Ion [47].

The reaction shown in Fig.3.11 depicts three primary ion energy brackets, low, medium, and high ion energy. The specific energy for these brackets varies with the material of the target and the composition of the plasma. At a low energy, as shown in the left diagram of Figure 3.11, a single knock-on interaction takes place. This interaction occurs when the low momentum ion penetrates the surface, backscatters, and dislodges the surface atom. The primary ion did the actual sputtering. The next bracket, medium energy, results in a linear cascade interaction. The linear cascade is multiple collisions between a moving atom and a stationary atom, but it is a moving target atom which dislodges the sputtered atom. The linear cascade process is typically the most desired and studied energy bracket [47]. The diagram on the right shows a spike interaction, which occurs at high energy. Instead of the moving atom to stationary atom interactions seen in the linear cascade model, spike collisions can occur between moving atoms in the target lattice. Spike collisions can lead to sputtering, but also cause damage to the surface of the target and generate excess heat.

The ratio between incident ions and sputtered atoms is referred to as sputter yield, S, denoting the efficiency of the process. The sputter yield, which can range from 0.1 to 10 [47], depends on the composition and energy of the plasma as well as the target material itself. Since materials have different sputter yields, an alloy target composed of two or more materials may experience different sputter rates for each material. This fact is crucial when dealing with ITO, since most targets used are either metallic, InSn, or ceramic, In_2O_3:SnO_2. Seen in Figure 3.12 is the sputter rate for In, Sn, O, and the total for a 9:1 In_2O_3:SnO_2 Cermaic Target. As seen, oxygen has the highest sputter yield followed by indium then tin. This difference could be related to mass of the atoms, since oxygen has a much smaller atomic mass of 16 compared to indium's 115 and tin's 119, but it also depends on the bonding energies between the target atoms.The net result of the varied sputter yields is that alloy targets require an initial conditioning sputter during which the elemental concentrations of the surface change from their bulk values to steady-state values for that process. Changes to the process that change the sputter yield will require another conditioning sputter.

For sputtered ITO, films are typically annealed after or during deposition with temperatures ranging from 100 to 400°C which result in conductivity of $10^{-3}\Omega$cm, and transmission of 90% at 500nm [28]. However, it has also been demonstrated that ITO films with similar properties, 4.76x$10^{-4}\Omega$cm and 90% at 500nm, can be sputtered at room temperature using an Ar - H gas combination [28]. Sputtering may require a low base pressure to achieve good, repeatable results. The target used can be expensive depending on the material, especially if a large target is required. Sputtering also has relatively slow deposition rates, ranging from 0.07 to 21 Å/s depending on the target material and sputtering conditions for ITO, compared to other deposition techniques.

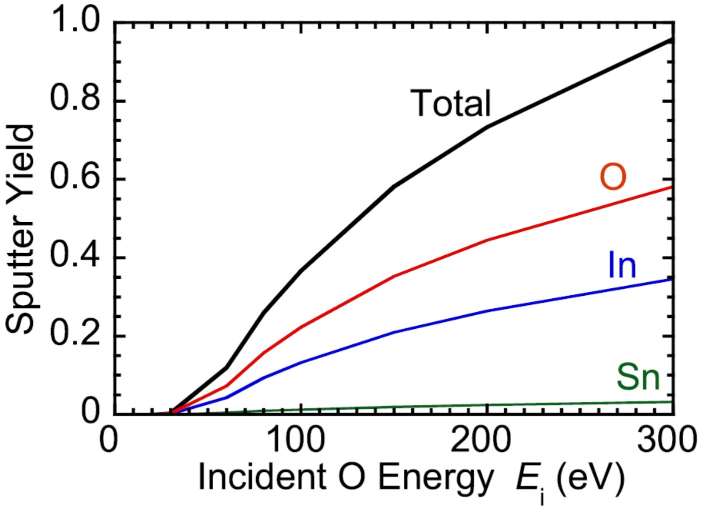

Figure 3.12: Sputter Yield of In, Sn, O, and Combined Total for 9:1 In_2O_3:SnO_2 Ceramic Target [50].

Once sputtered, the various species need to reach the film and condense. For oxygen this is unlikely, so a reaction between the film and the ambient environment is needed. For this reason, O_2 is often added to the sputter ambient environment. The impact of this is further elaborated in Chapter 5.

Chapter 4

Experimental Design & Methods

The goal of this work was to decrease the heat and time, also referred to as the thermal budget, used in the deposition of thin film indium tin oxide, specifically for use in Rochester Institute of Technology cleanroom. The motivation for this experiment originated from a need for a low heat process to deposit ITO on heat-sensitive materials that other research projects utilized. The results of this work were intended to expand the use of ITO in current and future projects in the RIT cleanroom by reducing the thermal budget of the current process. In Section 4.1, the system configurations for the sputter tool, the baseline processing steps, screening experiments, and anneal studies are discussed. In Section 4.2, the methods and tools used to characterize the sputtered ITO are discussed, including the films effect on fabricated devices.

4.1 Deposition Experiments

The method of deposition for this work is sputtering, using a CVC601 sputter system located in the RIT Semiconductor and Microsystems Fabrication Laboratory (SMFL). The CVC601 is a DC magnetron sputtering system with 4 target heads, three of which have a diameter of 8 inches and one 4 inch target head. The 4" head has the flexibility to switch between targets, allowing for a wide range of material to be sputtered. Three different gases, argon, oxygen, and nitrogen, can be flowed into the chamber to generate a plasma. The rate of flow of these gases are controlled by mass flow controllers (MFC). These gauges measure gas flow in standard cubic centimeters per minute, sccm. During deposition, a throttle valve is used to limit the pumping speed of the hi-vac pump, a cryogenic pump, allowing for the desired sputtering pressure to be achieved. A cryogenic, or cryo, pump uses liquid nitrogen cooled fins to trap molecules via cryosorption. The roughing pump, a rotatory vane pump, pumps the chamber down from atmosphere to a crossover pressure. During the pump-down and deposition process the pressure in the chamber is monitored by two pressure gauges. The first, used during the sputtering process, is a Baratron gauge, which is accurate in the 0.1 to 100mT range. The second gauge is a cold cathode gauge and is used below 10^{-3}T [51]. The DC power supply used to strike the plasma has a maximum power output of 2000W for 8" targets and 500W for the 4" target. This power supply also has a pulsed mode where the DC supply produces an asymmetric square wave at an adjustable frequency, 25 to 250 kHz, and duty cycle, allowing for dielectric targets to be sputtered. Figure 4.1 shows a schematic of the CVC601 system.

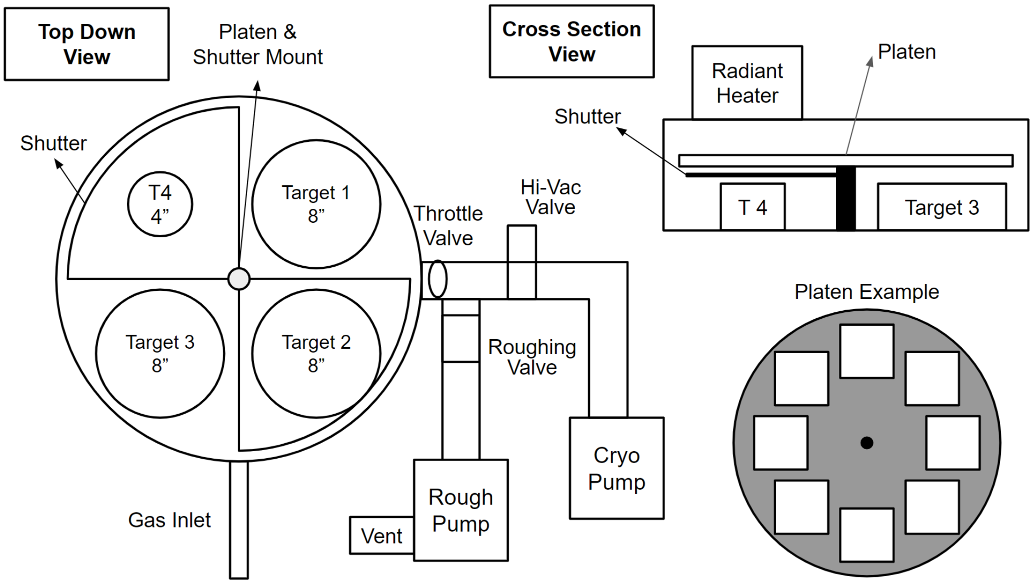

Figure 4.1: CVC601 Cross Section, Components, & Configuration

In Figure 4.1, the shutter covers two targets simultaneously and can be moved 90° to cover the other two. As mentioned in Section 3.3.2, the shutter is primarily used during the presputter to clean the targets surface while protecting the substrate. Mounted above the shutter, on a separate, grounded rod, is the platen. The platen is the substrate holder and the CVC601 comes with different configurations, one for 6” wafers, one for 4” wafers, and one for 5” by 5” substrates. Since the substrate in sputtering is part of the grounded anode, the platen and the rod the platen connects to must be conducting and connected to ground. One of the primary features of the platen is its option to rotate, increasing the uniformity of the sputtered film at the cost of reduced deposition rate. The CVC601 also has a radiant heater placed above target 4. This attachment allows for the heating of substrates, which can improve the film properties.

Two targets could be used to sputter ITO, an 8” ITO dielectric target, comprised of 90:10 In_2O_3:SnO_2, and a 4” 90:10 In:Sn target. The 8” target is sputtered in pulsed mode since it contains oxygen while the 4” target can be reactively sputtered with an Ar:O_2 ambient, since the target lacks oxygen, in either DC or pulsed mode. The primary parameters explored with this work are: deposition power, oxygen gas content, DC or pulsed deposition, stationary or rotating platen, post deposition anneal time and temperature, and anneal tool. The baseline process to be improved is defined in Section 4.1.1.

4.1.1 Baseline Deposition Parameters

The baseline ITO sputtering process uses the 8 inch dielectric ITO target and a 2 hour, 400°C post deposition anneal to achieve a film with high transmission and low resistivity. The deposition uses a power of 180W, a rotating platen, a sputter pressure of 5mT, a 20 minute presputter, and 40 sccms of argon. With a deposition rate of around 0.55Å per second, an hour sputter time was typically used to achieve a 2000Å film. This process has been used to create ITO back gates for thin film transistors [52]. A request for ITO on a HgTe detector exposed a limitation to this process. The 400°C anneal would cause the Hg in the device to out-diffuse and be released into the annealing tool used, so the film could not be annealed.

The as-deposited films typically resulted in a resistivity of 8.4x$10^{-3}\Omega$-cm and a transmission of 62%. The annealing process resulted in a resistivity of 5x$10^{-4}\Omega$-cm and a transmission of 79%. Initial depositions were done to recreate this baseline, verifying that the processing window used in previous work had not changed. Additional, smaller screening experiments investigated varying oxygen content, Ar flow rate, and sputter pressure conditions were also done. The aim of these experiments was to see if there was any room for improvement of the baseline process using the 8" dielectric target.

The post deposition anneal step was done using tube 5 of the Bruce furnace stack. The recipe used a 2hr, 400°C anneal in air. The Bruce furnace required time to ramp up to the anneal temperature and slowly ramp down afterwards. In total, the anneal recipe took 4 hours to run, with 2 of those hours committed to the 400°C anneal.

The total time used to deposit an ITO thin film with this baseline process is at least five and a half hours, not including the time to pump down the sputter chamber to an appropriate base pressure. This long processing time and relatively high temperature anneal are the main parameters to be improved in this work.

4.1.2 Initial Screening Depositions

Reactive DC sputtering using the 4 inch InSn alloy target was seen as an opportunity for potential improvement. Since oxygen needed to be added to film, the reactive sputter may engineer better film properties. The oxygen concentration of the film, as discussed in Section 2.2, heavily impacts the transmission and conductivity of the film. Therefore, an ideal combination of oxygen flow during deposition may enable one to achieve the desired conductivity and transmission properties.

A thorough characterization of the metal target was done in 1994 by Infante [53]. However, due to hardware updates to the CVC601 sputter system, Infante's settings no longer worked so a new processing region needed to be defined for the 4" target. This was accomplished by first determining the best Ar + O_2 partial pressure combination via screening depositions. Prior to this work, the 4" target had not been used for a number of years, leaving the target with an oxidized top layer. To clean the surface for sputtering, first the target was wiped down with isopropyl alcohol to remove any loose particles. Then, after the target had been loaded and the chamber pumped to a base pressure of $9.7\text{x}10^{-6}$T, a presputter with Ar was done. Initially, a power of 100W, sputter pressure of 12mT of argon, and a flow rate of 30 sccms were used, but the high number of arcs occurring between the target and plasma forced the power supply into a protected state. Arcing of the target surface during sputtering could be indicative of particles on its surface. The power was lowered to 80W and a 2 minute presputter was attempted again. While there was significant arcing, the power supply was not forced to stop the sputter. The power was then stepped up to 90W for another 2 minute presputter. This same process of short, 2 minute presputters was done from 80 to 180W, with 10W steps. By increasing the power of the target clean, contaminants or moisture trapped deeper in the target was sputtered off.

With the target now sufficiently cleaned, the desired sputtering conditions could be established. The deposition power was set to 100W, the sputter time was set to 5 minutes, and the platen of substrates was kept stationary. The stationary platen allowed for individual samples to be sputtered with different parameters, meaning multiple settings could be tested with only one pump down. Glass slides were primarily used as substrates to allow for transmission measurements to be made. A total sputter pressure of 12mT was chosen to enable more control over the oxygen partial pressure. With a set sputter pressure, the O_2 partial pressure was stepped from 0 to 1.5 mT, with 0.5mT increments. It was found that between 0.5 and 1mT of oxygen, the as deposited film went from a metallic film with no transmission and high conductivity to almost essentially glass-like, with high transmission in the visible spectrum and high resistivity.

Using the 0.5mT of oxygen as the lower boundary, another sputter was performed to narrow in on an optimal oxygen partial pressure. Similar sputtering conditions were used, 100W sputter power, 5 minute sputter time, stationary platen, and 12mT sputter pressure. The oxygen partial pressure was set to 0.5, 0.65, and 0.8mT, investigating the area of interest identified in the previous deposition test. A 10 minute, 100W presputter was done prior to the deposition, cleaning the target surface. It was found that the 0.8mT of oxygen sputtered a film with acceptable conductivity and transmission.

Subsequent runs would be done to verify this result, testing the 0.65 and 0.8mT oxygen partial pressures, as well as varying the deposition power using an oxygen partial pressure of 0.8mT. The results of these sputters and a more in-depth analysis of the depositions described above are discussed in Chapter 5.

4.1.3 Anneal Studies

To study the impact that the deposition power, post deposition anneal temperature and time had on the ITO film, a slightly modified 2^3 full factorial design of experiments was created and run. Three main effects were used. Main effect A, the anneal temperature had three levels, 0, 200, and 230 °C, where the 0 setting designates the un-annealed or as-deposited. Main effect B, the anneal time, also had three values, 0, 1, and 2 hours. Main effect C, the deposition power, had two levels, 95 and 100 Watts. The goal of this design was to maximize the transmission and minimize the resistivity of the film. Other metrics that were also investigated were the non-uniformities of both the sheet resistance and thickness. The sputters were carried out with a partial pressure combination of 11.2mT Ar and 0.8mT of oxygen, a rotating platen, and a 10 minute, 110W presputter. The substrates used were Swiss Glass slides. The anneals were done in Blue M Ovens, using a gas flow of compressed dry air. The 200°C anneal setting was chosen since it was half of the baseline anneal, while 230°C was chosen as it was between the 200°C setting and the maximum temperature of the Blue M Oven used, 250°C. In order to minimize the amount of substrates used, the slides were broken into three pieces, one of which remained un-annealed as a control. Figure 4.2 shows how the slides used in Designs A and B and the wafers used in Design C were cleaved.

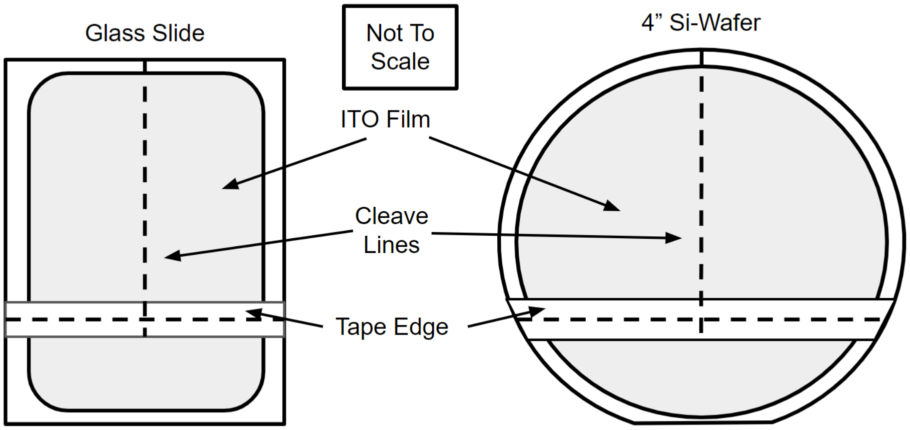

Figure 4.2: Substrates Used For Anneal Studies.

As shown in Figure 4.2, the glass slides and wafers were broken into three separate pieces, with the piece by the wafer flat and shortest piece of the slide being kept as un-annealed control substrates. The tape edge noted is a strip of Kapton tape placed on the deposition area. Once the ITO film has been sputtered, the tape is peeled off creating a strip of bare substrate in the film. This strip is used to collect thickness measurements using profilometry. The tape is placed off to one side to allow for a greater, uninterrupted area to collect sheet resistance measurements using an automated CDE Resmap tool. Shown Table 4.1 are treatment combinations, TC, of the three factors for Design A.

Table 4.1: Treatment Combinations for Design A.

TC	A - Temperature [°C]	B - Time [hr]	C - Power [W]
-	as-deposited	0	95
-	as-deposited	0	95
-	as-deposited	0	100
-	as-deposited	0	100
(1)	200	1	95
A	230	1	95
B	200	2	95
AB	230	2	95
C	200	1	100
AC	230	1	100
BC	200	2	100
ABC	230	2	100

An ITO deposition was done with the intention of replicating the parameters used for the 100W samples above in Design A. However, due to an unforeseen change to the MFC of the CVC601 sputter system, the flow rate of the argon was displayed differently. Instead of the value corresponding to a percentage of the maximum flow, it showed the actual flow rate in sccms. This was an issue as the MFC had a 200 sccm maximum, so 40% would be an actual flow rate of 80 sccm. This change resulted in an unintentional lowering of the oxygen flow rate. The remaining deposition parameters were unchanged, 100W power, 11.2mT of Ar, 0.8mT of O_2, rotating platen, and 30 minute sputter time. While unexpected, this opportunity allowed for the impact of the flow rate of the gas on the film to be characterized and studied. This new design was labeled Design B. The goal of Design B was the same as Design A, maximize the transmission while minimizing the resistivity and non-uniformity of the sheet resistance and thickness. The same 0 settings were used for the as-deposited films. Seen in Table 4.2 are the treatment combinations for Design B.

Table 4.2: Treatment Combinations for Design B.

TC	A - Temperature [°C]	B - Time [hr]	O_2 Gas Flow [sccm]
-	as-deposited	0	8.16
-	as-deposited	0	8.16
-	as-deposited	0	5.5
-	as-deposited	0	5.5
(1)	200	1	8.16
A	230	1	8.16
B	200	2	8.16
AB	230	2	8.16
C	200	1	5.5
AC	230	1	5.5
BC	200	2	5.5
ABC	230	2	5.5

An additional 2^4 full factorial design was also performed. This larger design used the 2^3 full factorial shown above in Design A and added a fourth main effect, D, the type of substrate used. Instead of just using glass slides, 4 inch silicon wafers with 3500Å of SiO_2 were also used as substrates. This variable was added to test if the type of substrate used influenced the film nucleation or subsequent annealing steps. The oxide layer was used to electrically isolate the ITO film from the Si surface. The new factorial design with the added effect, labeled Design C, is described in Table 4.3.

The goal of this design was to maximize the transmission and minimize the resistivity and non-uniformity of both the sheet resistance and thickness. To supplement the designs shown above, an anneal study was also done of the baseline process. The films were annealed for 1 or 2 hours at 230°C and for 2 hours at 400°C. This provided a comparison for the higher temperature setting of the other designs and more data for the baseline process. Other, one off anneal tests at 250 and 300°C were also done on the 95 and 100W samples. Fused silica wafers were used for the anneals at or above 300°C, since the glass slides used for the lower temperature anneals could begin to out-gas boron, potentially contaminating the Bruce tube furnace used to anneal at the higher temperatures. Bare Si wafers were also included in all three designs, used to determine the refractive index via ellipsometry.

Table 4.3: Treatments Combinations for Design C.

TC	A - Temperature [°C]	B - Time [hr]	C - Power [W]	D - Substrate
-	as-deposited	0	95	Slide
-	as-deposited	0	95	Slide
-	as-deposited	0	100	Slide
-	as-deposited	0	100	Slide
-	as-deposited	0	95	Wafer
-	as-deposited	0	95	Wafer
-	as-deposited	0	100	Wafer
-	as-deposited	0	100	Wafer
(1)	200	1	95	Slide
A	230	1	95	Slide
B	200	2	95	Slide
AB	230	2	95	Slide
C	200	1	100	Slide
AC	230	1	100	Slide
BC	200	2	100	Slide
ABC	230	2	100	Slide
D	200	1	95	Wafer
AD	230	1	95	Wafer
BD	200	2	95	Wafer
ABD	230	2	95	Wafer
CD	200	1	100	Wafer
ACD	230	1	100	Wafer
BCD	200	2	100	Wafer
ABCD	230	2	100	Wafer

4.2 Film Characterization

This section and its subsections focus on detailing the tools and methods of characterizing the ITO films sputtered in Sections.4.1.1 & 4.1. Table 4.4 lists the tools used, their method of operation, and the film property that they measure.

Table 4.4: Metrology Tools Used & Method of Operation

Film Property	Tool Name	Method of Operation
Thickness	Tencor P2	Profilometry
Sheet Resistance	CDE Resmap	4-point Probe
Transmission, Reflectance, Absorption	PE-Lambda	Spectroscopy
Crystallinity	Bruker D8 Advance	X-Ray Diffraction
Refractive Index	Rudolph IV	Ellipsometry
Composition	Tescan Bruker Vega 3	Electron Dispersive Spectroscopy

Using a Tencor P2, 5 profilometry measurements were taken for each sample. These measurements were used to calculate the mean, a standard deviation, and non-uniformity, NU, of the thickness of the film. The NU can be calculated using Equation 4.1, where σ is the standard deviation and *barx* is the mean. A CDE resmap was used to automatically take 4-point probe measurements at 25 to 49 sites, depending on the size of the sample. The tool then automatically calculated the mean, standard deviation, and NU for each sample based on sheet resistance data.

$$NU = \frac{\sigma}{\bar{x}} * 100\% \tag{4.1}$$

A Perkin-Elmer (PE) Lambda is a UV-Vis spectrophotometer and is configured to allow for transmission, reflection, and absorption to be measured. Glass slides and fused silica wafers were used for these measurements. While the tool could take transmission, absorption, and reflection data, it was only used for transmission and absorption measurements. The reflection data was calculated using Equation 2.1. This was done to save time, as each scan took around 5 minutes, with another 10 minutes dedicated to extracting and converting the data into an excel file format. Additionally, the scanned region was limited to wavelengths from 200 to 800 nm, with the primary interest in the visible spectrum. The visible spectrum was defined to 380 to 750nm, with the average of this range being used for transmission data.

4.2.1 Figures of Merit

Figures of merit, FOM, are used to combine key metrics into a single value to judge a film. The key metrics used to assess the ITO films are the sheet resistance, R_{sh}, and transmission, T. Three FOMs found in the literature, are shown in Equations 4.2 to 4.4 [52, 54, 55].

$$FOM(P) = \frac{T}{R_{sh}}\ [\Omega^{-1}] \tag{4.2}$$

$$FOM(H) = \frac{T^{10}}{R_{sh}}\ [\Omega^{-1}] \tag{4.3}$$

$$FOM(G) = -\frac{1}{R_{sh} ln(T)}\ [\Omega^{-1}] \tag{4.4}$$

With all 3 FOMs, the higher the value, the better the film properties. However, some of these FOMs do not weigh the sheet resistance and transmission equally. This can be best seen graphically, and is illustrated in Figure 4.3.

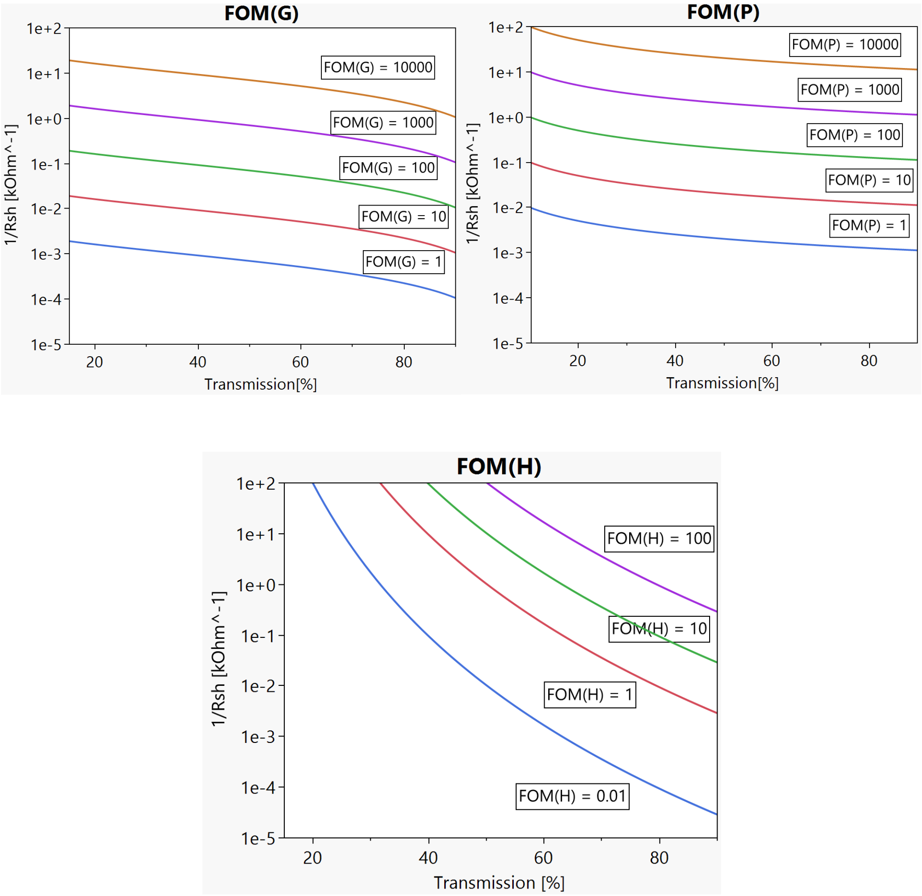

Figure 4.3: FOM(G), Top Left, FOM(P), Top Right, and FOM(H), Bottom, Graphed.

It can be noted that both FOM(G) and FOM(P) show similar patterns. This highlights the primary disadvantage of these two FOMs. They both place a higher emphasis on the sheet resistance of the films rather than the transmission. For example, a very high FOM(G) film can be achieved with a film with 20% transmission. So while the FOM may designate this film as one of high quality, in reality it would not be usable for many purposes due to the poor transmission. That being said, the FOM(H) shows a more even weight of the sheet resistance and transmission, with a high FOM(H) value occurring at transmissions at or greater than 50%. Therefore, only the FOM(H) value will be used in this work.

4.2.2 p-Si Solar Cell Process Flow

As a proof of concept, the lower thermal budget ITO film was used in a temperature sensitive device. The device used was a solar cell fabricated via an updated RIT Turnkey Solar Cell fabrication process. This process flow was designed as a rapid method to fabricate Si solar cells in the RIT cleanroom. It was first developed in 2014 by M. Bohra [56] and was last worked on by R. Kamat in 2016 [57].

Significant revisions were needed to update the process flow to meet current fabrication capabilities in the RIT cleanroom. A general overview of the process flow used can be seen in Figure 4.4.

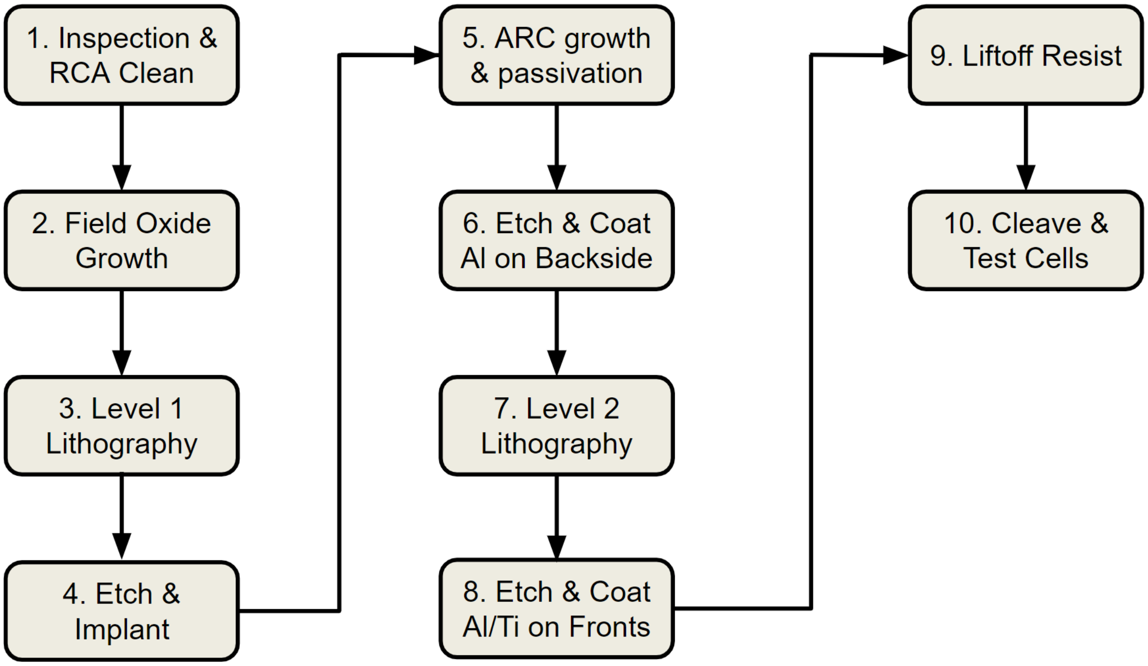

Figure 4.4: 4 Inch p-Si Solar Cell Fabrication Flow.

While Figure 4.4 is a broad glance at this process, a more in depth description of processing parameters can be found in Appendix A. Ultimately, the completed solar cell cross section and wafer layout can be seen in Figures 4.5 and 4.6.

For this work, the most notable component in Figure 4.5 is the anti-reflective coating (ARC), which is labeled as 95nm of SiO_2. However, an ITO ARC will also be used and compared to the baseline SiO_2 ARC. The anti-reflection coating, as discussed in Section 1.2, works to mitigate reflections caused by a change in refractive index. The ARC thickness was calculated using Equation 4.5 [12].

$$t_{ARC} = \frac{\lambda}{4n_{ARC}} \tag{4.5}$$

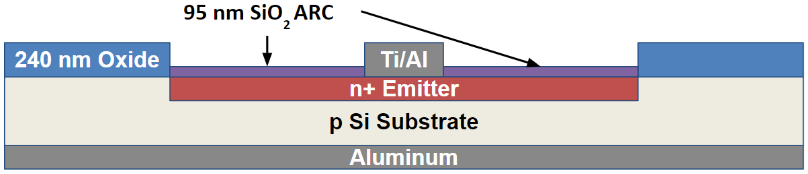

Figure 4.5: Cross Section of Completed p-Si Solar Cell.

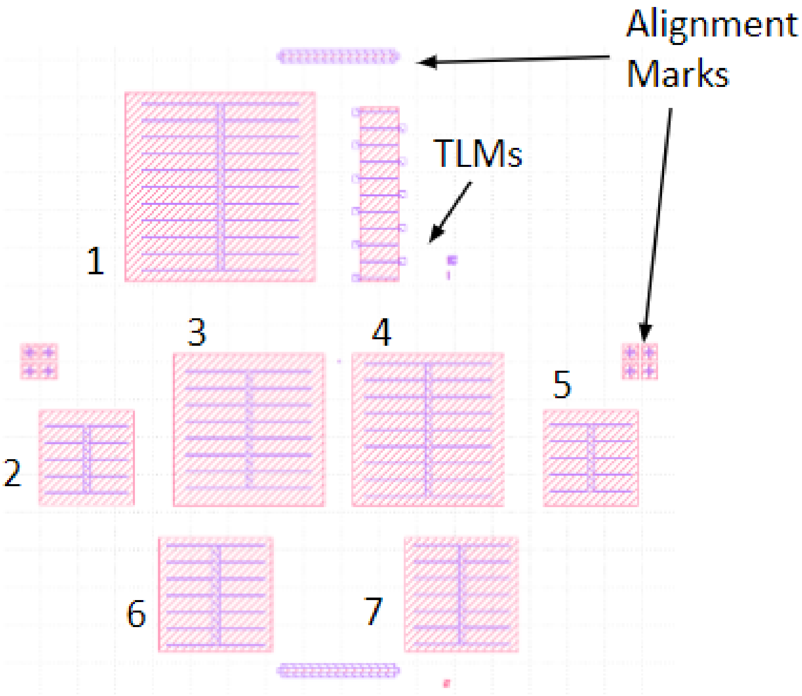

Figure 4.6: Mask Design Used in Turnkey Solar Cell Fabrication.

Fused silica, SiO_2, has a refractive index of around 1.47. Since interaction between different wavelengths of light and the ARC are dependent on the thickness, the ARC thickness is typically optimized for a specific wavelength. In this case, the ARC thickness was set using a wavelength of 550nm, one of the highest energy points in the solar spectrum [6]. Doing the same for ITO, which has a refractive index of around 2, yields an ARC thickness of 69nm for a wavelength of 550nm. ITO has two advantages over oxide in terms of an ARC application. Since ITO's refractive index is almost perfectly in between the indices of air and Si, 1 and around 4 respectively, it lessens the reflection between the air-ITO and ITO-Si interface. Additionally, since ITO is also conductive, it lessens the resistance of the emitter. These two effects should improve the efficiency of the solar cell over all.

The mask design seen in Figure 4.6 was updated and adapted from Kamat(2016) [57]. The solar cells, labeled 1-7, all have a finger widths of 100μm and a finger spacing of 2100μm. This was done to minimize the number of variables in the design. Seen in Table 4.5 are the dimensions for the 7 solar cells.

Table 4.5: Dimensions of Solar Cells Used.

Cell #	# of Fingers	Area [cm^2]	Bus Bar Width [μm]	Shadowing [%]
1	11	6.25	850	6.88
2	5	1.5625	850	8.18
3	8	4	750	6.11
4	9	4	750	6.92
5	5	1.5625	850	8.18
6	7	2.25	1025	9.94
7	7	2.25	680	8.18

While some of the cells shown in Table 4.5 have the same area, there are subtle differences between them. Cells 3 and 4 have the same area, but cell 4 has an additional row of fingers. This additional row works to decrease the resistance of the emitter by creating another path for carriers to be collected. However, by adding more metal to the solar cell, the shadowing increases. Shadowing in a solar cell is the total area of metal over the total area of the cell. Therefore, while the added finger aids in carrier collection, it blocks some light from reaching the silicon. This same concept can be seen in cells 6 and 7, where cell 6 has a thicker central bus bar than cell 7. These two pairs of cells are aimed to determine if the increase in carrier collection is worth to cost of shadowing. Cells 2 and 5 are exactly the same and are typically used to test for variance. However, in this work, these cells will be used to test the ITO ARC and compare it to the baseline SiO_2 ARC.

Three p-Si wafers were used to fabricate solar cells to evaluate ITO as an ARC coating. Each wafer had a distinct doping profile, using either a new combination or one repeated from Kamat [57]. The repeated profiles were used to ensure there was no performance degradation between the updated and old process while the new doses explored areas for possible improvement. Table 4.6 lists the implant doses for the three wafers fabricated.

Table 4.6: Doping Profiles for 4" p-Si Wafers With an ITO ARC.

Wafer #	Net Dose [cm^2]	D_1 [cm^2]	E_1 [KeV]	D_2 [cm^2]	E_2 [KeV]	Repeated?
3	2x10^{15}	2x10^{15}	55	0	0	Yes
4	2x10^{15}	1x10^{15}	55	1x10^{15}	35	No
5	6x10^{15}	2x10^{15}	55	4x10^{15}	35	Yes

The split emitter implants for wafers 4 and 5 are also referred to as engineered emitters. By splitting the dose at a high and lower energy, the doping profile is shifted, as seen in Figure 4.7.

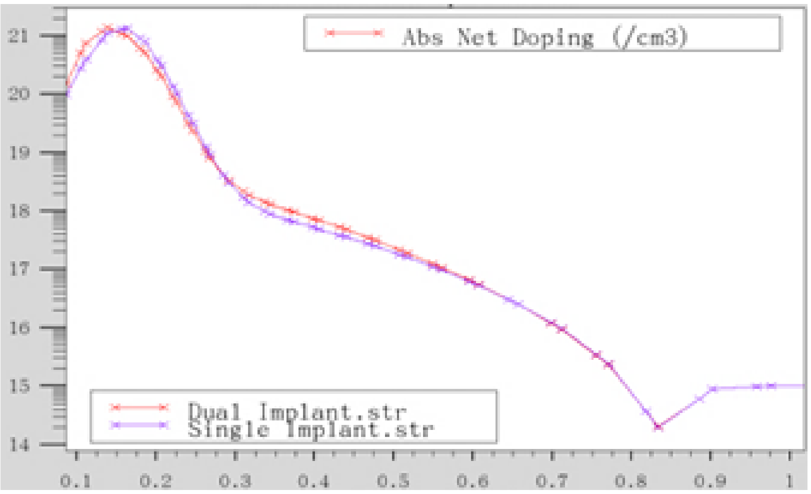

Figure 4.7: Comparison Between Split and Whole Doping Profiles for p-Si Emitter Implant.

Seen in Figure 4.7, the single implant profile had a dose of 1x10^{16} cm^2 and voltage of 55 KeV. The dual implant had a net dose 1x10^{16} cm^2, with 6x10^{15} cm^2 implanted at 35 KeV and 4x10^{15} cm^2 implanted at 55 KeV. The subtle shift in the dual implant profile towards the surface of the substrate leads to higher carrier mobility and therefore increased carrier collection [57]. Wafers 3 and 4, with the same net dose, were included to further characterize this effect.

The transmission line measurement (TLM) structures are shown in Figure 4.8 and are used to analyze the contact resistance of a metal layer. The standard TLM method of extracting the contact resistance or other metrics are depicted in Figures.4.8 and 4.9.

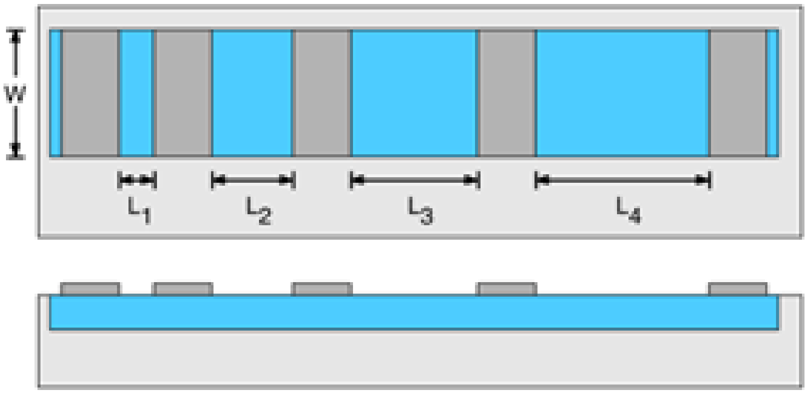

Figure 4.8: Standard Design for TLM Features [58].

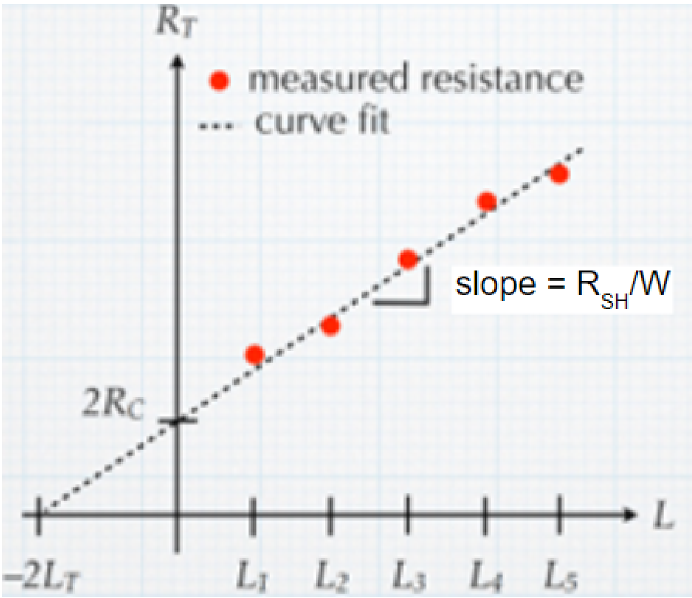

Figure 4.9: Theoretical Graphical Analysis of TLM Resistance Measurements [58].

By measuring and graphing the resistance (R_T) between contact pads as a function of the spacing between pads, key metrics can be extracted and calculated. The R_C is the resistance of the contact and can be extracted by dividing the y-intercept by 2. The L_T is the transfer length or the average distance charge carriers travel beneath the contact before flowing up into it. This value can be graphically determined by dividing the x-intercept by negative 2. R_{SH} is the sheet resistance of the substrate and can be extracted from the slope or calculated using Equation 4.8 [58].

$$L_T = \sqrt{\frac{\rho_C}{R_{SH}}}\ [\mu m] \tag{4.6}$$

$$R_C = \frac{R_{SH} L_T}{W}\ [\Omega] \tag{4.7}$$

$$R_T = \frac{R_{SH}}{W}(L + 2L_T)\ [\Omega] \tag{4.8}$$

$$\rho_C = R_C L_T W\ [\Omega cm^2] \tag{4.9}$$

The ρ_C seen in Equations 4.6 and 4.9 is the contact resistivity , a common figure of merit for contacts. The lower the ρ_C value, the better the contact. These TLM structures will be used to characterize the contact resistance before the ITO is applied and after. Ideally, the ITO will decrease the R_C, mitigating the parasitic resistance.

The process flow shown in Figure 4.4 had to be altered slightly to allow for sputtering of the ITO directly onto the cells without any patterning, resulting in a simpler process. This was accomplished by first covering cell number 2 with Kapton tape. The wafer was dipped into buffered oxide etch at a concentration of 10:1 for 3 minutes, etching the oxide ARC. However, since the taped cell was covered, it was not etched and retained its oxide ARC. The wafer was then processed normally, forming both the front and back contacts. After the cell was completed, the ITO was sputtered onto the front, with the taped cell covered again. With the tape removed, the covered cell still retained its SiO_2 ARC where as the the other 6 cells have an ITO ARC. Cells 2 and 5 could then be tested and compared to one another, determining the impact of a conductive ARC.

This process requires a low thermal budget ITO due the grid contact on the n-type emitter, a titanium-aluminum film stack. By placing a 500Å layer of Ti in between the Al and n-type Si, Kamat [57] found that the contact resistance was reduced. The work function of Ti, as opposed to Al, provides a better ohmic contact. However, when introduced to a high temperature, the Ti and Si could interact and form a silicide, typically seen in a TiSi or $TiSi_2$ composition. This Ti silicide has a larger lattice constant, 8.27 Å [59], and therefore forms a worse interface between the n-Si and Al, increasing stress and mitigating the carrier collection ability. Silicides has been noted to form during a 320°C, 1.5 hour anneal [60]. Therefore, using the 400°C and 2 hour anneal from the ITO baseline process would result in the formation of TiSi. To test this hypothesis the finished solar cell was tested as-deposited and after an anneal.

Chapter 5

Results & Discussion

This chapter details the results and analysis of the experiments described in Chapter 4. JMP was used for making the graphs and statistical analysis.

5.1 Baseline Process Results

The baseline ITO process, as described in Section 4.1.1, was last used in Packard et al [52]. To determine if the processing window was still viable, or if there was any room for immediate improvement, the sputter pressure, argon gas flow, and oxygen partial pressure were all varied. These test depositions used the 8 inch In_2O_3:SnO_2 dielectric target and were carried out using the following parameters: sputter power of 180 Watts, pulsed sputter mode with a 1616ns pulse width, 20 minute presputter, 5 minute sputter time, and a stationary platen. Glass slides were used as substrates for these depositions. Seen in Table 5.1 are the summarized results of varying the sputter pressure and Ar gas flow.

Table 5.1: Initial ITO Baseline Sputter Experiments

Pressure [mT]	Ar Flow [sccms]	t [Å]	ρ [Ωcm]	Transmission [%]	R_{sh} NU [%]	t NU [%]
2.5	27	-	-	-	-	-
*5	40	1740	0.017	86.09	15.13	20.4
5	50	1997	0.0499	-	4.16	15.43
5	60	1687	0.029	72.78	12.16	13.4
5	70	1819	0.806	-	12.43	13.41
5	80	1969	0.024	52.74	13.91	10.94
10	80	2039	0.051	52.37	4.82	15.3
15	80	1815	0.0587	81.65	10.65	28.2

As seen in Table 5.1, the gas combination used in the previous work is indicated with an asterisk in the pressure column. Most noticeably, at the lowest sputter pressure, no film was deposited with the plasma that was generated. Comparing the baseline parameters to the varied gas flow results, it is clear that there is little immediate opportunity for improvement when compared to the baseline. While the film sputtered using a higher pressure and gas flow had good transmission, its resistivity and thickness non-uniformity were subpar, especially since its transmission was still less than that of the baseline. Adding oxygen to the chamber was attempted as well. It was found that while adding 0.5mT of oxygen to the flow drastically increased the transmission, it resulted in totally non-conductive glass-like films. The post deposition anneal step was also investigated as an area of possible improvement.

In order to achieve uniform starting samples for multiple anneal temperatures, the baseline process indicated by an asterisk in Table 5.1 was sputtered again, but with a moving platen. The moving platen ensured all of the substrates received a more uniform film than doing the samples one at a time. The substrates used were 2 glass slides, a 4 inch fused silica wafer, a bare 4 inch Si wafer, and a 4 inch Si wafer with 3500Å of SiO_2 thermally grown on its surface. The fused silica wafer was intended to be used for transmission measurements of samples heated to high temperature, since the glass slides would out gas contaminants into the furnace ovens. The bare wafer was included for refractive index data collected via ellipsometry as well as XRD scans. The wafer with oxide was included for additional data points and to gauge the impact, if any, of the substrate on the sputtered sample. The films were cleaved into separate pieces as shown in Figure 4.2, which were then annealed at 230 or 250 °C in a Blue M Oven, or 400°C in a furnace tube. Sheet resistance, transmission, absorption, and thickness measurements were taken on each of the sputtered samples. Figures 5.1 and 5.2 show the spectral responses of the ITO on the fused silica wafer after being annealed at 230 and 400°C.

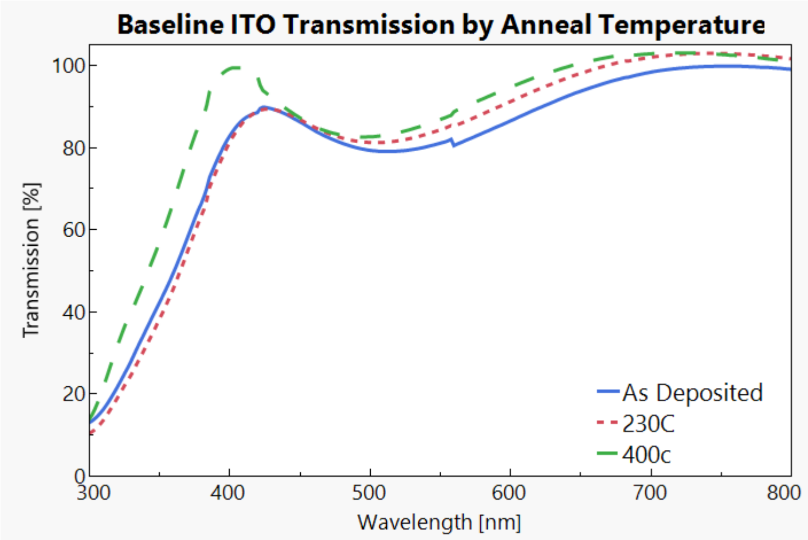

Figure 5.1: Baseline ITO Transmission by Anneal Temperature.

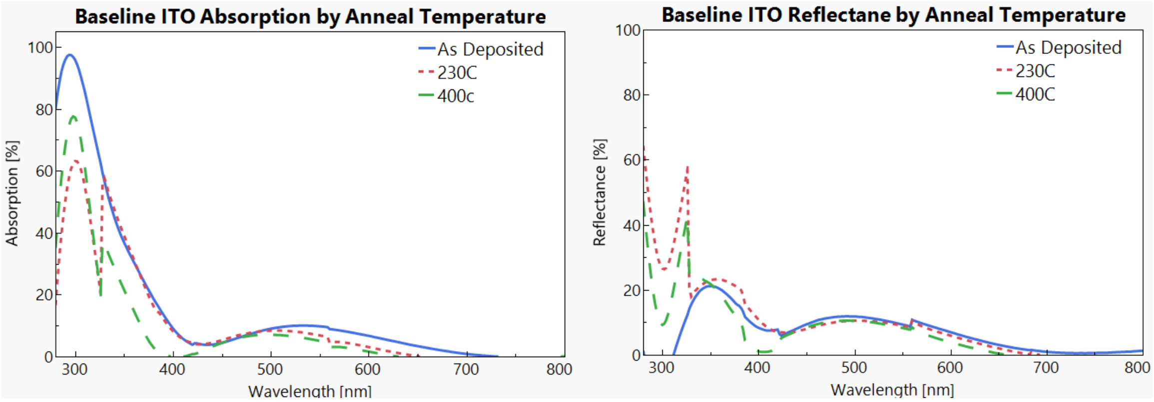

Figure 5.2: Baseline Reflectance and Absorption by Anneal Temperature.

While there is a small increase in the transmission of a film from the 500 to 800nm range, the most noticeable improvement came after the 400°C anneal, with an increase in transmission at 400nm. While the increasing anneal temperature decreased the absorption and Reflectance in the 400 - 800nm range, it had a varied impact below 400nm. As the wavelength of light reaches the ultraviolet range, the absorption and reflection of the films increases greatly. This is expected and is seen in most ITO samples as discussed in Section 2.1. The transmission data plotted above was used to calculate the mean transmission of the films, using a range from 380 to 750nm. The results of those calculations, as well as the corresponding resistivity data for those samples can be seen in Figure 5.3.

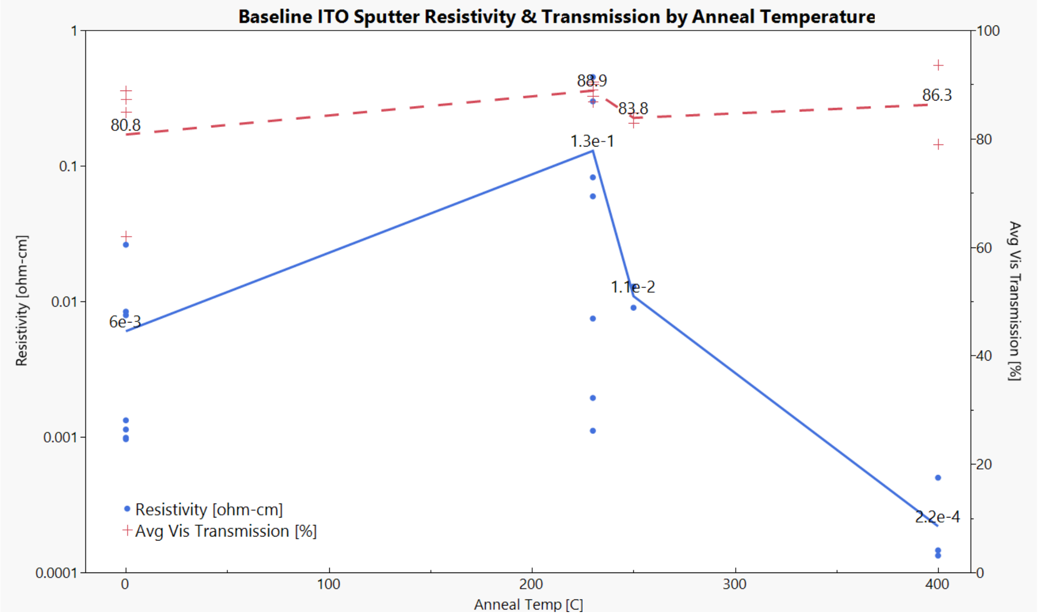

Figure 5.3: Impact of Post Deposition Anneal Temperature on Baseline ITO Resistivity and Transmission.

Depicted in Figure 5.3, the crosses and dashed lines are the transmission measurements from the glass slides and fused silica wafer while the dots and solid line are from all of the substrates. While the first anneal at 230°C yielded an improvement in transmission, it resulted in a noticeable increase in resistivity. Increasing the anneal temperature to 250°C reduced the resistivity slightly, it coincided with a decrease in transmission. This could indicate a region of transition, where the film is shifting from one phase or crystal structure to another. Once the film was annealed at 400°C, both the transmission and ρ drastically improved, yielding a high quality film. To study if there was any correlation between the change in T and ρ, crystallinity and crystal phase data was collected for the bare Si and fused silica wafer substrates.

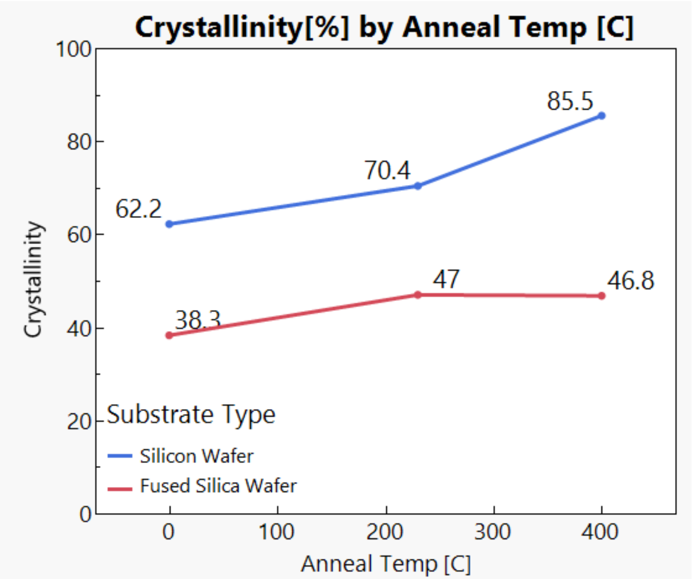

Figure 5.4: Baseline ITO Crystallinity by Anneal Temperature.

The impact of the substrate on the crystallinity of the film is apparent in Figure 5.4. While the crystallinity of both films increases as they are annealed, the films on the fused silica wafer appears to have a maximum crystallinity at around 47% whereas the films on Si achieved up to 85%. The substrates are similar in that their as deposited films are more amorphous, as a result of using sputtering as the deposition method. This promotion of crystallinity by the Si wafer could be due to its own crystal structure, with the ITO film naturally aligning to the Si structure to better adhere to the surface. The opposite of this could be true for the fused silica substrate. The crystallinity values used in Figure 5.4 were calculated using XRD scans of the samples. To better understand and account for the impact of the substrates on the crystal structure of the film, a bare (100) Si wafer and fused silica wafer were scanned. The results of this scan can be seen in Figure 5.5.

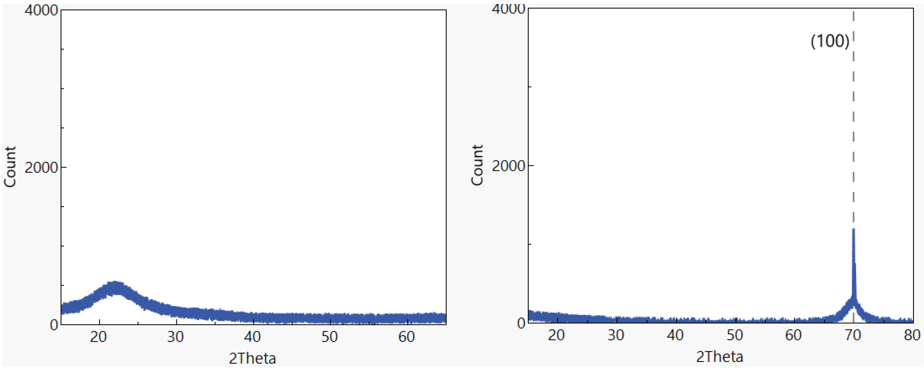

Figure 5.5: XRD Scans of Bare Fused Silica and (100) Si Wafers.

As expected, the bare Si wafer showed a peak at around 69° which corresponds to the (100) phase of Si whereas the fused silica wafer was almost completely amorphous. To ensure the Si peak did not impact the results of XRD scans, the ITO films were only scanned using a range of 5 to 65 2Theta. This negated the Si peak and produced accurate readings of only the ITO peaks. While there could be some ITO peaks at or beyond 69°, most of the literature regarding ITO XRD focuses on the 5-65 2Theta range [28] allowing for easy comparison. The complete scans for the annealed ITO samples on both substrates can be seen in Figures 5.6 and 5.7.

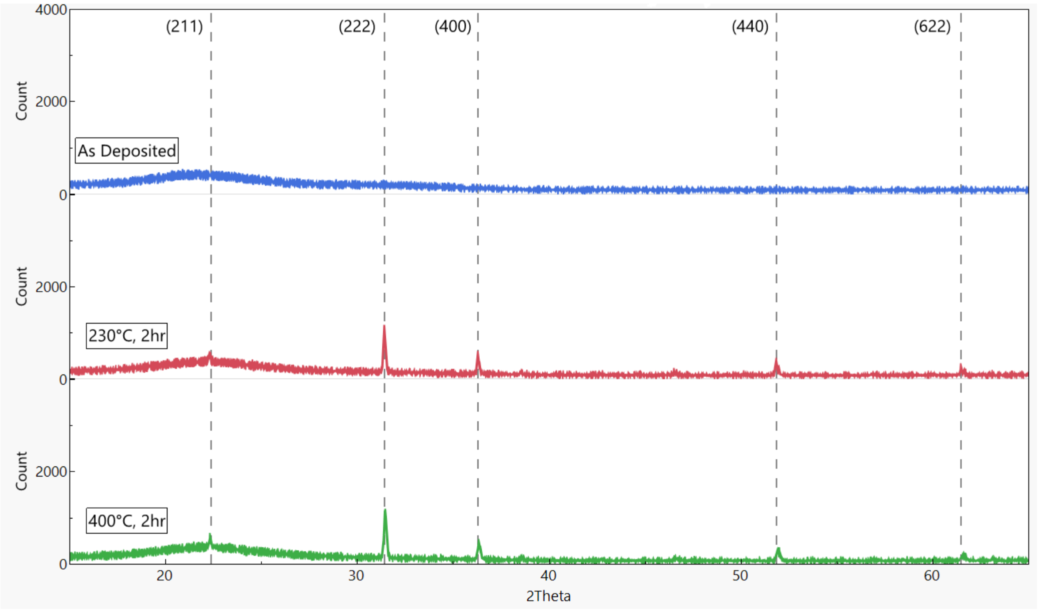

Figure 5.6: X-Ray Diffraction Results by Anneal Temperature on Fused Silica Wafer.

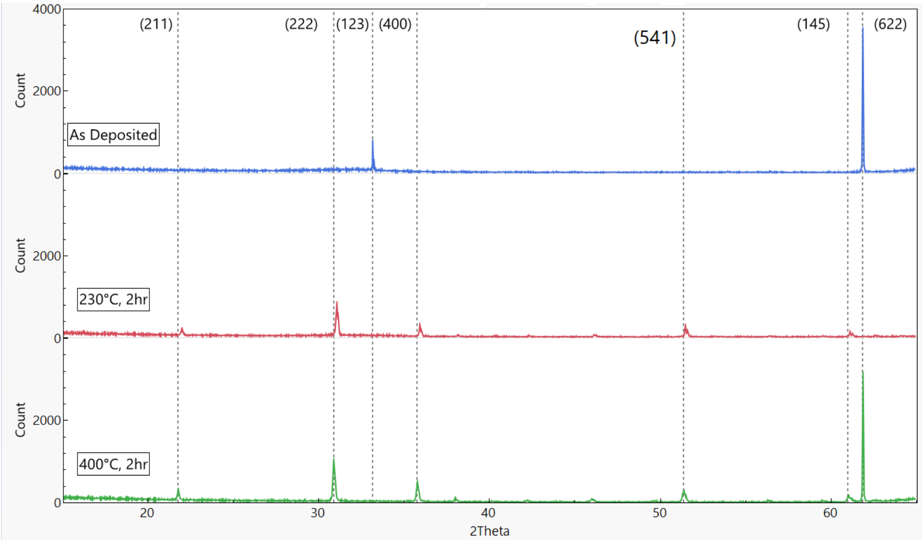

Figure 5.7: X-Ray Diffraction Results of Baseline ITO by Anneal Temperature on Si Wafers.

While both substrates demonstrate similar peaks, the largest differences are the presence of a preferred (622) peaks in the Si wafer films and increased noise surrounding the (211) peak in the fused silica samples. While the as deposited fused silica sample is very amorphous, without any peaks, the annealed results show some crystal formation. The formed peaks are not noticeably impacted by the increased annealing temperature, possibly indicating that the film has reached a stable structure. The same cannot be said for the Si samples. When the as deposited film is annealed to 230°C, the (123) and the (622) peaks are both lost with the formation of peaks at 21, 31, 35, 51, and 60°. When a sample with the same film is annealed to 400°C the (123) peak is still lost with the formation of the other peaks. The preferred peak at 61° is unchanged at the high temperature anneal. The loss of the (622) peak in the 230°C film does coincide with an increase in the resistivity. As seen in Banerjee et al [61], the 222, 440, and 622 peaks are derived from the indium oxide present in the film. Further similarities with Banerjee can be seen in Table 5.2 [61].

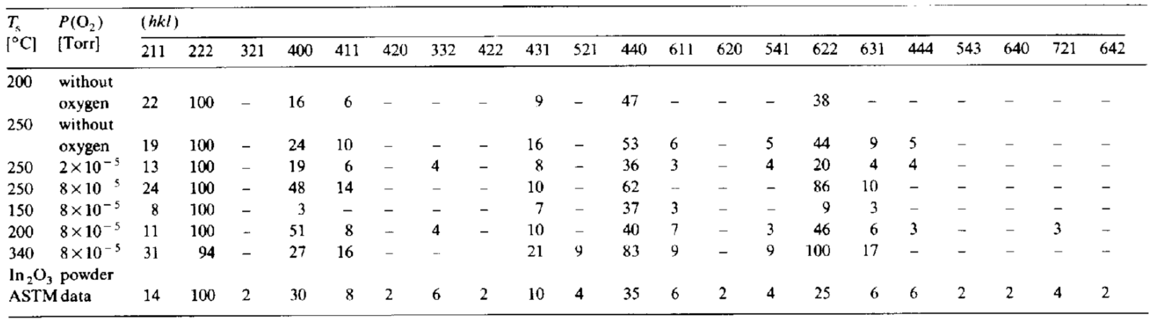

T_s [°C]	$P(O_2)$ [Torr]	(*hkl*) 211	222	321	400	411	420	332	422	431	521	440	611	620	541	622	631	444	543	640	721	642
200	without oxygen	22	100	–	16	6	–	–	–	9	–	47	–	–	–	38	–	–	–	–	–	–
250	without oxygen	19	100	–	24	10	–	–	–	16	–	53	6	–	5	44	9	5	–	–	–	–
250	2×10^{-5}	13	100	–	19	6	–	4	–	8	–	36	3	–	4	20	4	4	–	–	–	–
250	8×10^{5}	24	100	–	48	14	–	–	–	10	–	62	–	–	–	86	10	–	–	–	–	–
150	8×10^{-5}	8	100	–	3	–	–	–	–	7	–	37	3	–	–	9	3	–	–	–	–	–
200	8×10^{-5}	11	100	–	51	8	–	4	–	10	–	40	7	–	3	46	6	3	–	–	3	–
340	8×10^{-5}	31	94	–	27	16	–	–		21	9	83	9	–	9	100	17	–	–	–	–	–
In_2O_3 powder ASTM data		14	100	2	30	8	2	6	2	10	4	35	6	2	4	25	6	6	2	2	4	2

Table 5.2: Indium Tin Oxide X-Ray Diffraction Reference Results.

The values listed for each of the peaks in Table 5.2 are a percentage of the maximum intensity of that scan. Table 5.2 demonstrates the impact of the anneal temperature and oxygen partial pressure on the XRD peaks. Notably, the same drop in the (622) peak can be seen when the sample is annealed at a temperature less than 250°C. Additionally, the resurgence of that peak seen at the 340°C matches the 400°C anneal shown in Figure 5.6. All of the peaks listed in Table 5.2 correspond to the cubic bixbyite formation of ITO(c-ITO) [61]. This demonstrates that as the samples are heated to a higher temperature, the c-ITO orientation increases.

The deposition and anneal experiments based off of the baseline ITO sputter process demonstrate that the original parameters yield the best film. Since the lower anneal temperatures yielded films of worse quality than the baseline, our focus shifted to reactive sputtering of the metallic target. These films and their results are discussed below in Sections.5.2 & 5.3

5.2 Screening Depositions

Initial screening depositions with the goal of sputtering oxygen starved ITO films were done using a 90:10 In:Sn metallic 4" target. This target was last characterized in 1994 by Infante [53]. However, significant changes to the sputter tool made the processing window established unusable, primarily due to the high gas flow rates that exceed the maximum flows of the current oxygen supply. The first test sputters with this target focused on identifying a partial pressure combination of argon and oxygen that yielded transmissive and conductive films. The net sputter pressure was set to 12mT to give better control over the O_2 partial pressure. The deposition power was set to 100W and a 10 minute presputter with the same power at a pressure of 12mT of Ar was done. Seen in Table 5.3 are the resulting properties of the sputtered films as the oxygen content was varied.

Table 5.3: Results of Varying the Oxygen Partial Pressure on Key Film Metrics.

Power [W]	O_2 PP [mT]	t [Å]	ρ [Ωcm]	Transmission [%]	t NU [%]	R_{sh} NU [%]
100	0	15008	0.00012	0	6.43	14.87
100	0.5	5560.7	0.0091	0	7.07	7.64
100	0.65	4887.7	0.1377	1.68	10.01	32.38
100	0.8	3227.4	0.0192	82.31	16.72	32.77
100	1	3226.8	6.131	84.67	9.05	85.79
100	1.5	1932.4	-	89.89	11.15	-
90	0.8	3365	-	84.41	11.14	-
110	0.8	6310	0.001	15.38	9.5	6.66

All of the depositions were done with a net sputter pressure, of 12mT, a stationary platen, and a 5 minute sputter time. As shown in Table 5.3, the oxygen partial pressure has a drastic impact on the deposition rate, the resistivity, and transmission of the ITO films. Additionally, as the films became more glass-like in their conductivity and transmission, the R_{SH} non-uniformity increased greatly. A sweet spot was identified at an oxygen partial pressure of 0.8mT, with a high transmission and good conductivity. The power was then varied at this partial pressure. The lower power resulted in a slower deposition rate and glass-like, non-conductive films. At 110W, the deposition rate increased and yielded a more metallic film, with higher conductivity and less transmission. In subsequent depositions, the power was adjusted by 5W increments from 95 to 110W. The results of which can be seen in Figure 5.8.

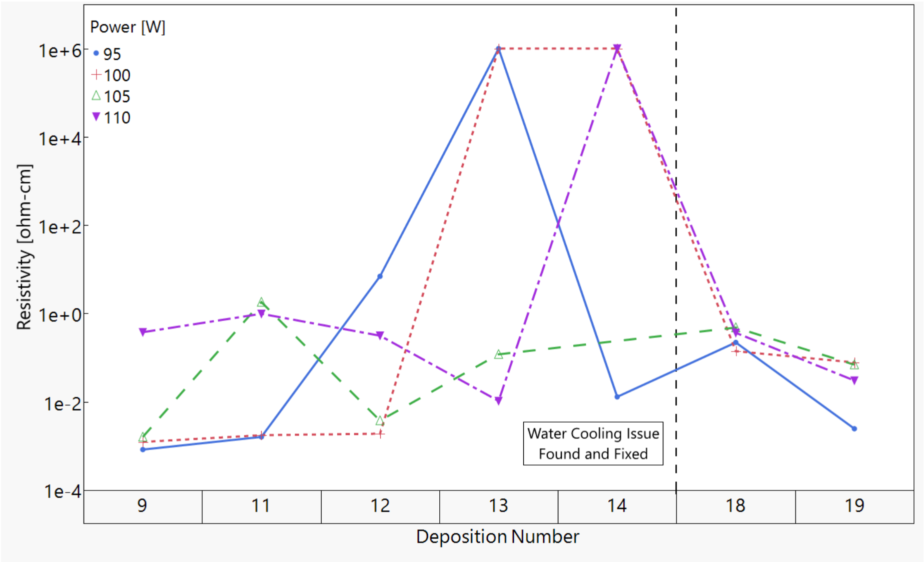

Figure 5.8: Resistivity by Deposition Run and Power.

In total, 7 depositions, or runs, were done with the same 11.2mT Ar and 0.8mT O_2 gas combinations, 95 to 110W deposition power, with a stationary platen and 5 minute sputter time per substrate. During the course of these sputters, significant variation between the results of each power setting across runs was noted. This is most apparent for runs 12, 13, and 14 as seen in Figure 5.8. Inbetween runs 14 and 18, the water cooling system that runs under each of the targets was found to be clogged, which was discovered when the piping burst. While it is apparent that the water cooling blockage impacted runs 12-14, it was initially unclear when the issue first began and which depositions could be used or needed to be excluded. The heating of the target, due to restricted cooling, not only impacted the repeatability of the depositions, but their sputter rate as well.

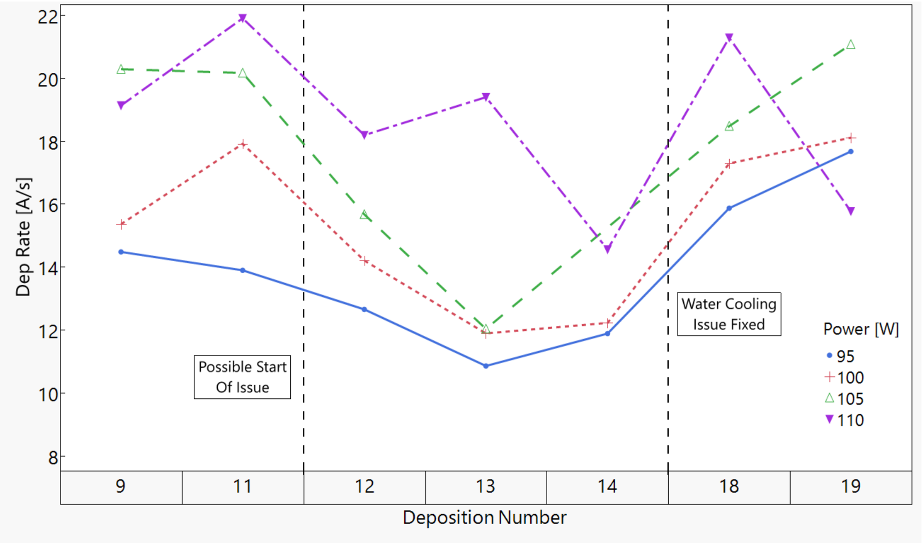

Figure 5.9: Impact of 4” Water Cooling Issue on Deposition Rate.

Using the deposition rates of runs 18 and 19 as a baseline, there is a clear dip seen in runs 12 to 14, shown in Figure 5.9. Prior to that dip, runs 9 and 11 appeared to be at a comparable deposition rate as the baseline runs after the cooling system was fixed. It can be concluded that the only impacted deposition experiments were runs 12, 13, and 14. There appears to be some variation with the 110W deposition rate, even after the fix. This can be attributed to the nature of the higher power deposition. When compared to the lower powers, both before, during, and after the cooling issue, the 110W deposition rate can be seen constantly fluctuating from one run to the next. With the range of the water cooling issue determined, the impacted data was excluded from further analyses. The results of the varied deposition power can be seen in Figure 5.10.

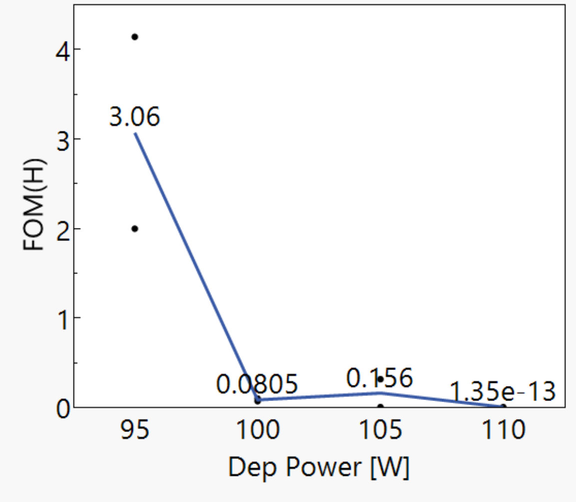

Figure 5.10: Results of Screening Depositions with Impacted Data Excluded.

Using FOM(H), it is clear that the 95W deposition power produced both conductive and transmissive ITO samples. While the 105W samples had a higher mean FOM(H) than 100W films, this was driven primarily by one sample, while the other 105W sample had a significantly lower FOM(H) value. Only the 95 and 100W set points were used in further experiments, due to their repeatable results. The screening experiments showed the following deposition parameters yielded the best as deposited films using the 4" metal target: Presputter of 110W for 10 minutes; Deposition power of 95W; 11.2mT of Ar and 0.8mT of O_2 as the ideal gas combination. Using these conditions, the films were annealed at various temperatures to study their improvement and the driving factors of those changes.

5.3 Anneal Studies

Since the baseline ITO deposition process utilized a 400°C anneal step, a lower anneal temperature was investigated to achieve similar results using the parameters determined in Section 5.2. Anneal temperatures of 200 and 230°C were primarily used with one-off anneals at higher temperatures being done as well. Three depositions were broken down into three different design of experiments to better analyze and characterize the driving factors of each design. Design A was focused on the impact of deposition power, Design B was designed to investigate the impact of the flow rate of oxygen, and Design C was intended to determine if the substrate affected the resulting films. XRD scans were used to better understand how the anneal temperature and time impacts the structure of the ITO.

5.3.1 Design A

Design A, as described in Section 4.1.3, uses design of experiments (DOE) and statistical analysis to determine if the anneal time, temperature, or deposition power has a driving impact on the transmission, resistivity, or non-uniformity of the sputter films. Figure 5.11 shows the FOM(H) of depositions done at 95 and 100W. Seen in both 95 and 100W films, there appears to be a transition point in the ITO films at 230°C. At this temperature, both films perform better than those annealed at 300°C. Breaking these values down from the FOM(H) values to their transmission and ρ values for 95 and 100W allows for further characterization.

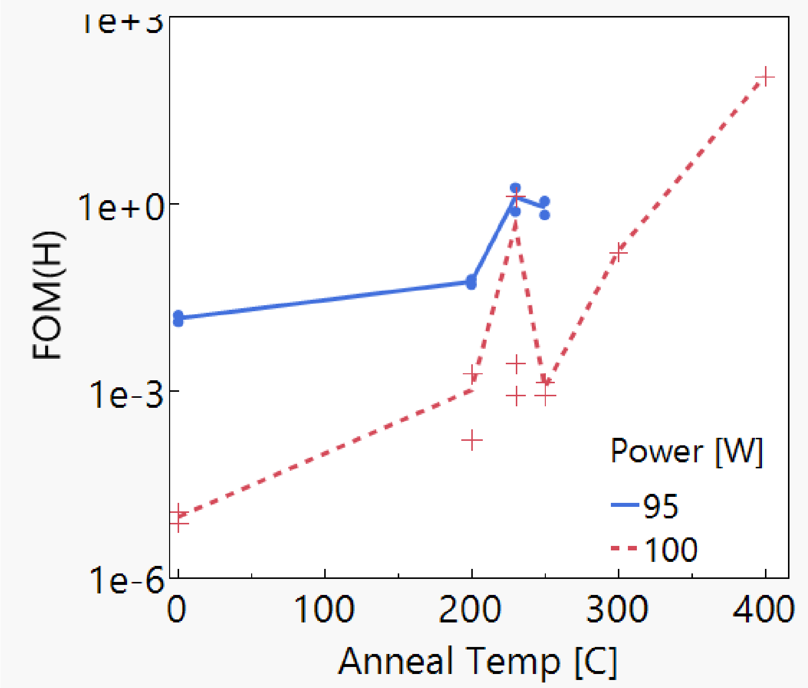

Figure 5.11: FOM(H) Results of Design A Sputters.

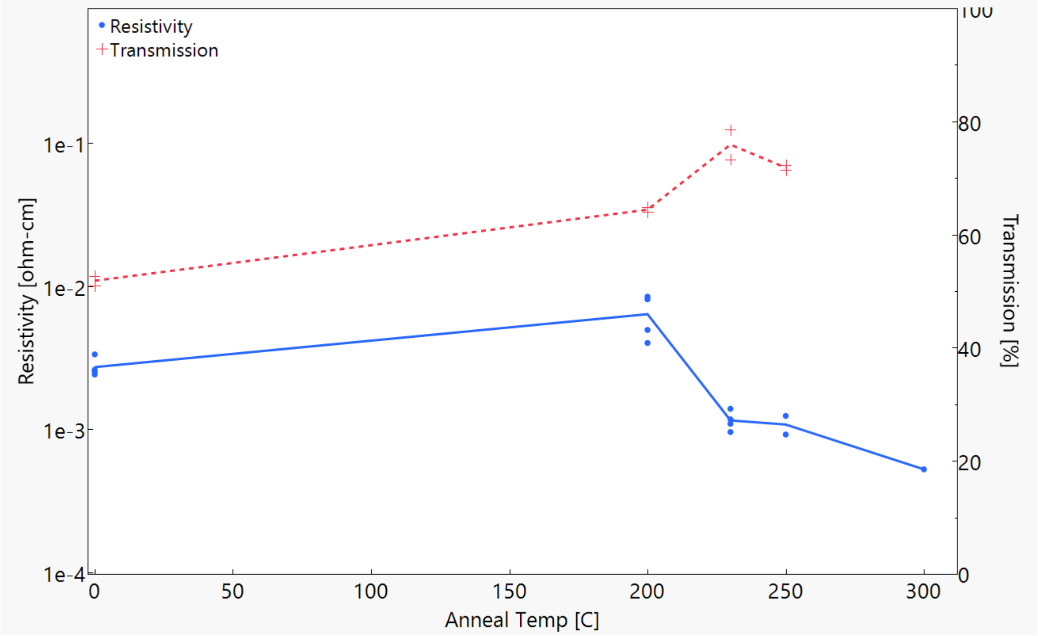

Figure 5.12: Resistivity and Transmission by Anneal Temperature for 95W Depositions.

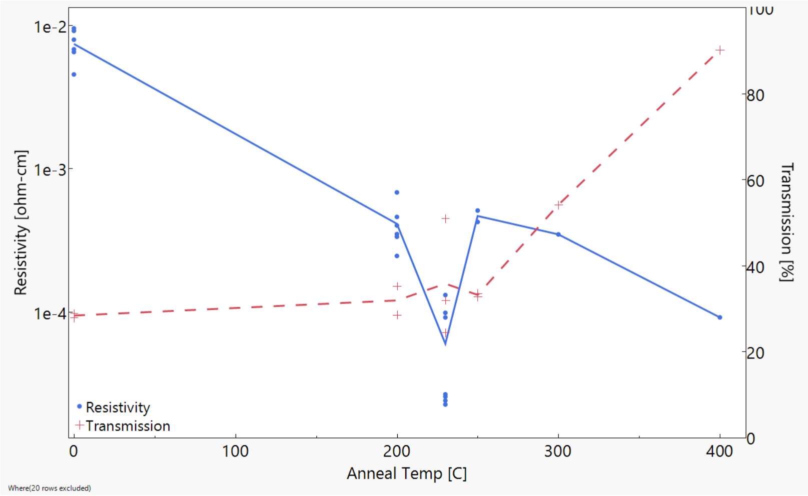

Figure 5.13: Resistivity and Transmission by Anneal Temperature for 100W Depositions.

For films sputtered at 95W, seen in Figure 5.12, at the 230°C inflection point, both the transmission and conductivity improve noticeably. In comparison, the 100W films demonstrates a significant improvement in resistivity at 230°C but barely any change in transmission. This demonstrates how FOMs can be deceptive. While the 100W, 230°C film in Figure 5.11 shows a film with good qualities, its low transmission makes it unusable in many applications. The results shown in Figures 5.11 to 5.13 are from films annealed for both 1 and 2 hours. JMP was used to generate and analyze the impact of the anneal temperature, time, and sputter power on the resistivity of the films. The resulting statistical analysis can be seen in Figures 5.14 and 5.15.

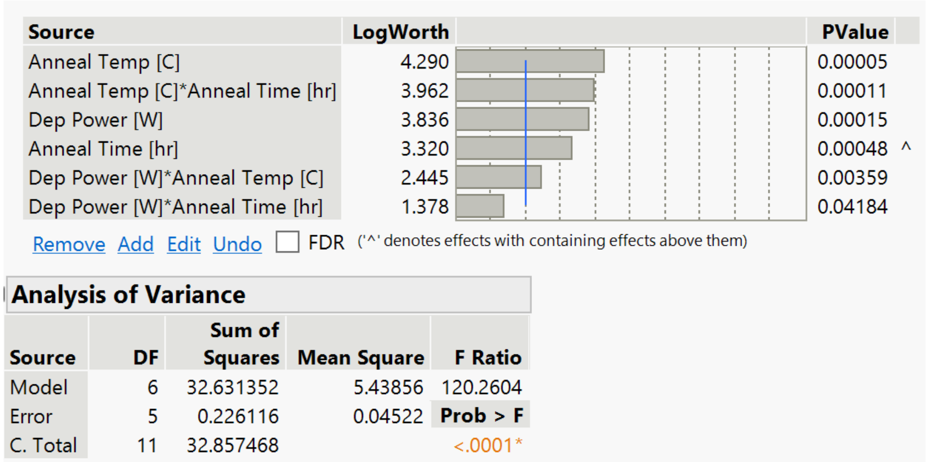

Source	LogWorth		PValue	
Anneal Temp [C]	4.290		0.00005	
Anneal Temp [C]*Anneal Time [hr]	3.962		0.00011	
Dep Power [W]	3.836		0.00015	
Anneal Time [hr]	3.320		0.00048	^
Dep Power [W]*Anneal Temp [C]	2.445		0.00359	
Dep Power [W]*Anneal Time [hr]	1.378		0.04184	

('^' denotes effects with containing effects above them)

Analysis of Variance

Source	DF	Sum of Squares	Mean Square	F Ratio
Model	6	32.631352	5.43856	120.2604
Error	5	0.226116	0.04522	**Prob > F**
C. Total	11	32.857468		<.0001*

Figure 5.14: Statistical Analysis of Design A for Resistivity.

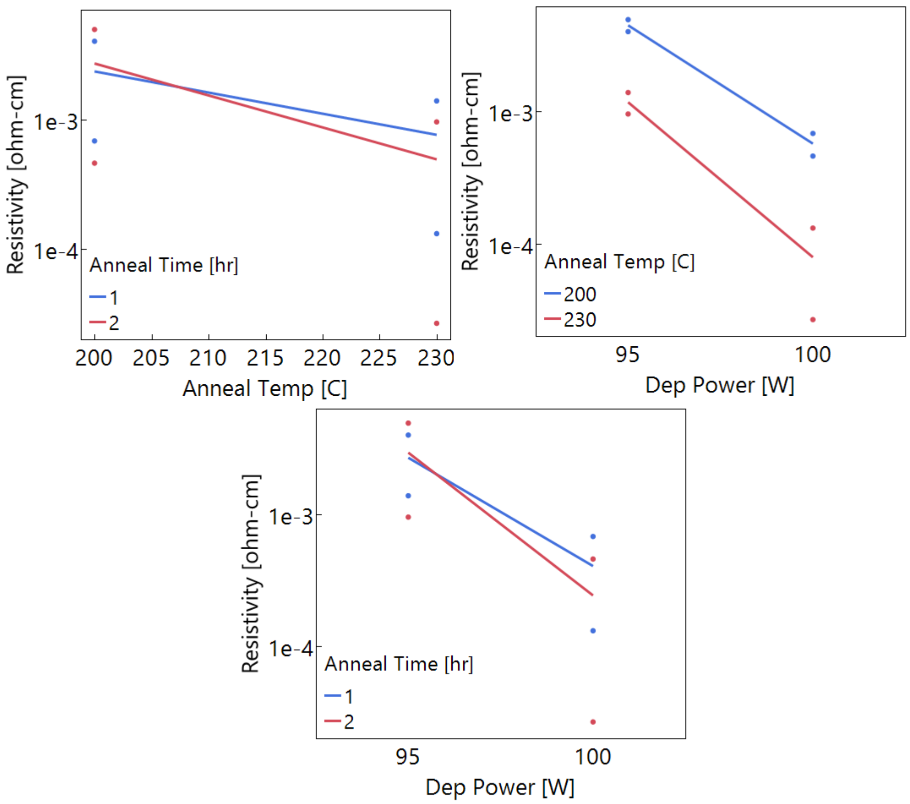

Figure 5.15: Design A Interaction Plots for 2-Factor Effects for Resistivity.

The statistical analysis above utilizes a series of t-tests to determine which means of the factors are significantly different from one another. If the calculated p-value is lower than the risk, α, of 0.05, then that factor is determined to have a statistically significant impact on the response. As shown in Figure 5.14, it appears all three main effects and all three 2-factor effects are significant. For the two factor effects, interaction plots can be generated to study if the two factors interact with one another. If the graphed lines intersect, then the two factors interact. For the anneal time-temperature and anneal time-power plots, it can be seen that the two factors have an impact on one another, with the 100W films having a stronger improvement from the increased anneal time than the 95W films. The 2 hour anneal at 230°C was also shown to produce the lowest resistance films. Using the analysis of variance table, ANOVA, in Figure 5.14, the variance of the model can be assessed. Since the calculated probability value is less than the risk, then the variance seen in this model is statistically significant and does not come from random variation. Since the goal of this design is to minimize the resistivity, the conditions used to achieve this are as follows: a power of 100W, anneal temperature of 230°C, and anneal time of 2 hours. The same analysis was done for the transmission.

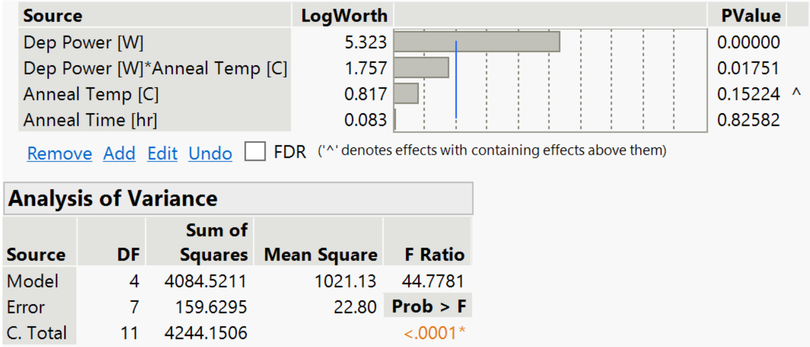

Source	LogWorth	PValue
Dep Power [W]	5.323	0.00000
Dep Power [W]*Anneal Temp [C]	1.757	0.01751
Anneal Temp [C]	0.817	0.15224 ^
Anneal Time [hr]	0.083	0.82582

Remove Add Edit Undo ☐ FDR ('^' denotes effects with containing effects above them)

Analysis of Variance

Source	DF	Sum of Squares	Mean Square	F Ratio
Model	4	4084.5211	1021.13	44.7781
Error	7	159.6295	22.80	**Prob > F**
C. Total	11	4244.1506		<.0001*

Figure 5.16: Statistical Analysis of Design A for Transmission.

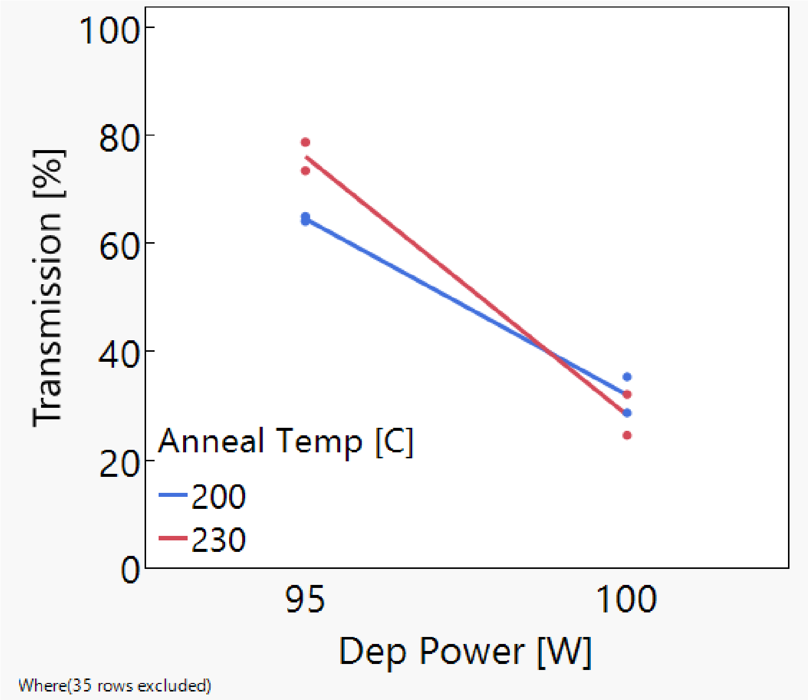

Figure 5.17: Design A Interaction Plots for 2-Factor Effects for Transmission.

The statistical analysis with the average transmission over the visible spectra as the response value is shown in Figures 5.16 and 5.17. The effects that are active in this model are primarily the deposition power and confounded power and anneal temperature. The anneal time had no impact on the overall transmission. The ANOVA table for this analysis shows statistically significant variance, indicating that the model is not caused by random variation. Looking at the interaction plot in Figure 5.17, there is a clear interaction between the power and temperature. To maximize the transmission, a deposition power of 95W and anneal temperature of 230°C should be used. It should be noted that the power is the driving factor of the transmission, having the largest impact on the resulting film.

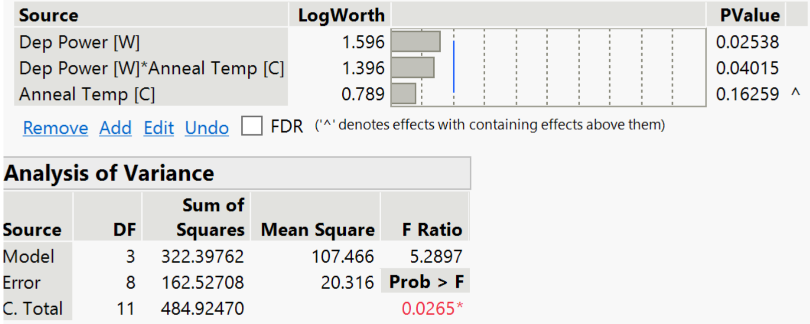

Source	LogWorth		PValue	
Dep Power [W]	1.596		0.02538	
Dep Power [W]*Anneal Temp [C]	1.396		0.04015	
Anneal Temp [C]	0.789		0.16259	^

('^' denotes effects with containing effects above them)

Analysis of Variance

Source	DF	Sum of Squares	Mean Square	F Ratio
Model	3	322.39762	107.466	5.2897
Error	8	162.52708	20.316	**Prob > F**
C. Total	11	484.92470		0.0265*

Figure 5.18: Statistical Analysis of Design A for Thickness Non-uniformity.

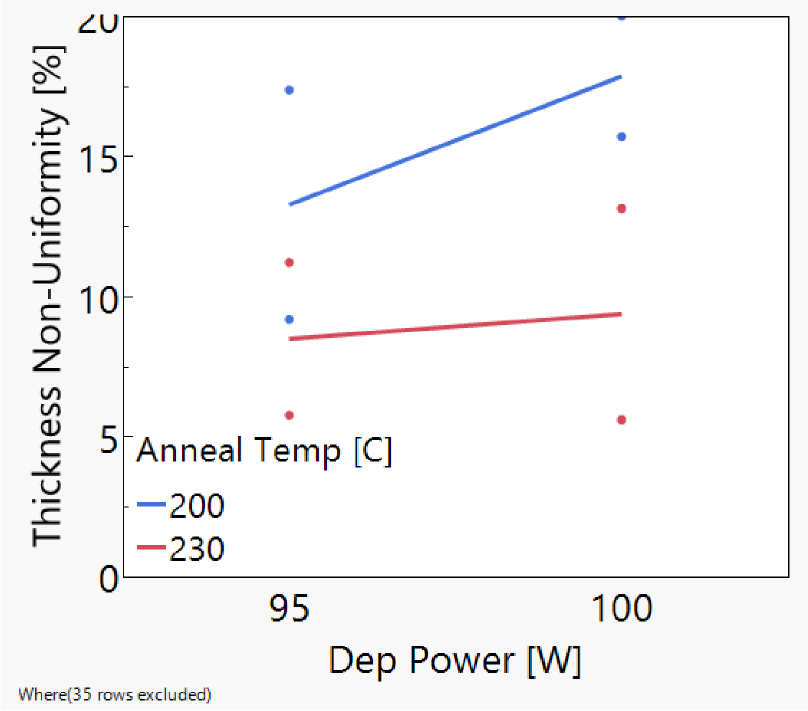

Figure 5.19: Design A Interaction Plots for 2-Factor Effects for Thickness Non-Uniformity.

Repeating the same analysis for the thickness non-uniformity of the sputtered films, the results can be seen in Figures 5.18 and 5.19. This model shows a weaker response than that of the transmission and resistivity, with the same active effects as the transmission analysis above. The ANOVA table also shows statistically significant variance between the means of the effects, but the higher p-value could indicate that there is unaccounted for variation present. The interaction plot for the power and anneal temperature 2 factor effect shows no interaction. To minimize the thickness non-uniformity, a power of 95W and temperature of 230°C should be used.

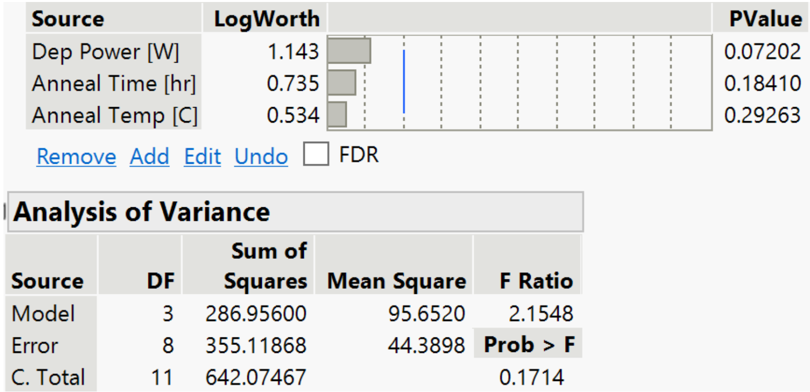

Source	LogWorth	PValue
Dep Power [W]	1.143	0.07202
Anneal Time [hr]	0.735	0.18410
Anneal Temp [C]	0.534	0.29263

Analysis of Variance

Source	DF	Sum of Squares	Mean Square	F Ratio
Model	3	286.95600	95.6520	2.1548
Error	8	355.11868	44.3898	Prob > F
C. Total	11	642.07467		0.1714

Figure 5.20: Statistical Analysis of Design A for Sheet Resistance Non-uniformity.

Using Figure 5.20, there is no statistically significant impact of the deposition power, anneal time, or anneal temperature on the R_{SH} non-uniformity. Additionally, the ANOVA table shows there is no significant difference between the means of variance for the factors analyzed. No further analysis can be done with this model to attempt to limit this response.

The overall objectives of Design A were to minimize the resistivity and non-uniformity while maximizing the transmission. There is an apparent conflict between the sputter power for the minimal resistivity, 100W, and ideal transmission, 95W. In this case, the ultimate application of this film dictates which parameter should be favored over the other. For a solar cell, if the ITO ARC has a high transmission and high resistivity, the cell can still function. While not optimal, the ITO will still provide an ideal ARC refractive index and have minimal losses due to reflection or absorption of the incident light in the ITO. On the other hand, if the ITO is very conductive but not transmissive, then the performance of the solar cell will be greatly inhibited by the lower amount of photons that are allowed into the substrate. Therefore, to obtain the best ITO film for a solar cell ARC application, a power of 95W, anneal temperature of 230°C, and either 1 or 2 hour anneal were used.

A model using the results of the resistivity and transmission DOE analyses was generated using JMP, yielding Equations 5.1 and 5.2. These models were only generated for Design A as it was focused on the main areas of interest, which are the 95W deposition power at lower anneal temperatures with ρ and transmission data. Since the resistivity and transmission DOE results showed statistically significant effects, these models can be used to potentially predict the responses of other power, temperature, or time settings. Equations 5.1 and 5.2 were graphically compared against experimental data from Figures 5.12 and 5.13, shown in Figures 5.21 - 5.23.

$$
\begin{aligned}
ln(\rho)_{Model} = -7.35 - 0.88\left(\frac{Temp-215}{15}\right) - 0.27\left(\frac{Time-1.5}{0.5}\right) - 1.27\left(\frac{Power-97.5}{2.5}\right) \\
- 0.09\left(\frac{Temp-215}{15}\right)\left(\frac{Power-97.5}{2.5}\right) - 0.27\left(\frac{Temp-215}{15}\right)\left(\frac{Time-1.5}{0.5}\right) \\
- 0.2\left(\frac{Time-1.5}{0.5}\right)\left(\frac{Power-97.5}{2.5}\right)
\end{aligned}
\tag{5.1}
$$

$$
T_{Model} = 50.2 + 0.72\left(\frac{Temp-215}{15}\right) - 20.27\left(\frac{Power-97.5}{2.5}\right) - 0.63\left(\frac{Temp-215}{15}\right)\left(\frac{Power-97.5}{2.5}\right)
\tag{5.2}
$$

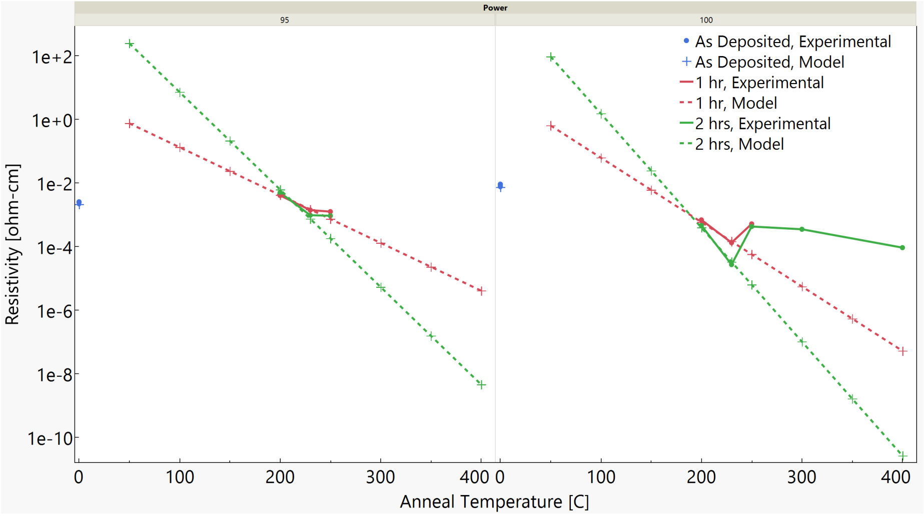

Figure 5.21: Design A Resistivity Model vs. Experimental Data at 95W (left) and 100W (right).

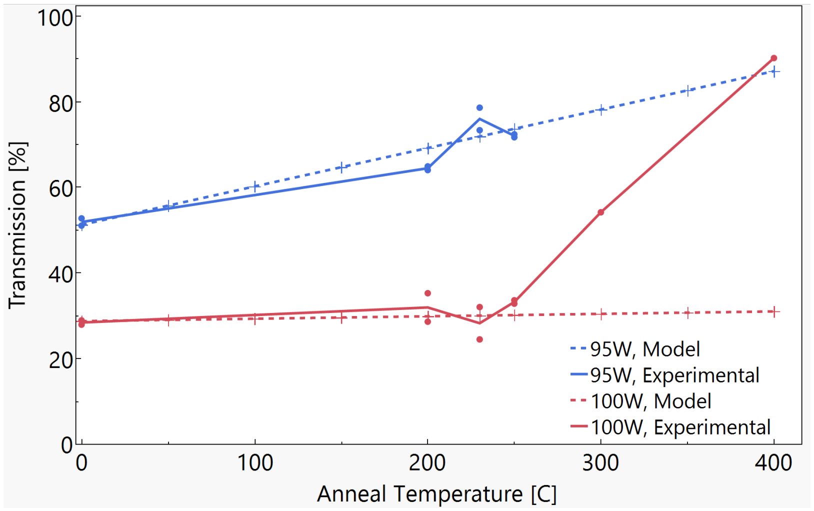

Figure 5.22: Design A Transmission Model vs. Experimental Data

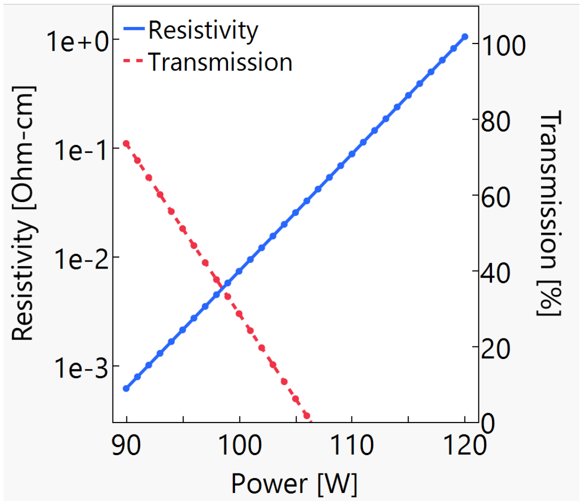

Figure 5.23: Design A Resistivity and Transmission Models at Varied Powers.

The models depicted in Figures 5.21 through 5.23 demonstrated a close match to the experimental data in Design A. However, when the models extrapolated new power, temperature, or time settings or was compared against data not included in Design A, the accuracy of the models decreased. The only notable exception to this was the 95W transmission model in Figure 5.22, which correctly modeled the anneal temperatures investigated in Design A as well as temperatures outside of the design. In Figure 5.21, the model lines were calculated using a power of 95 and 100W and an anneal time of 1 and 2 hours with the anneal temperature increased from 0 to 400°C in steps of 50. Since the model was created using data from only 3 different temperatures, 0, 200, and 230°C, it is only accurate at these temperatures, with the model deviating from experimental data as the anneal temperature increases. When other power settings were modeled without any annealing, the simulated data in Figure 5.23 did not match what was seen in the screening depositions in Section 5.2. In Table 5.3, it can be seen that the 90W power setting yielded a non-conductive film with high transmission, while Figure 5.23 simulated a high transmission and low resistivity for the same power. These results indicate that the deposition and anneal settings investigated in Design A are not suitable to predict the results of settings outside the studied values. To generate a more accurate model, Design A could be appended with a wider range of power and anneal settings.

The impact of the varied deposition and anneal parameters explored in Design A on the crystal structure of the ITO films was studied. Seen in Figures 5.24 and 5.25 are the XRD scans done on films annealed and sputtered with the conditions described in Design A.

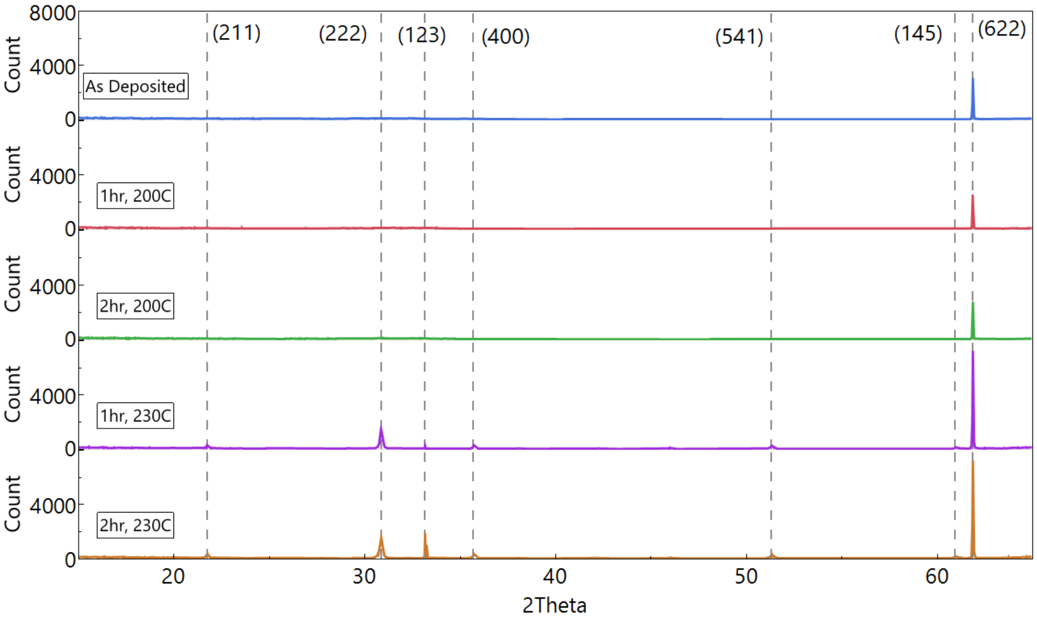

Figure 5.24: X-Ray Diffraction Results for Design A 95W Depositions by Anneal Temperature and Time.

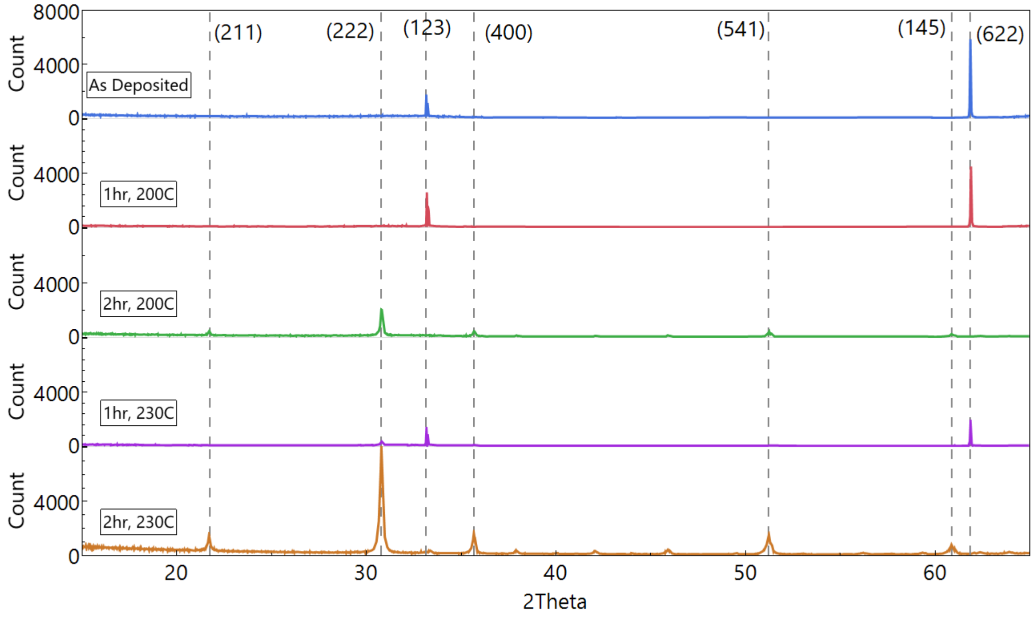

Figure 5.25: X-Ray Diffraction Results for Design A 100W Depositions by Anneal Temperature and Time.

It is evident that the power and anneal temperature have a defining impact on the crystal structure of the film, with the films deposited at different powers reacting differently to the anneal temperature. Instead of both films gradually forming towards the same preferential peaks, it appears that the 100W films gravitated towards the (222) peak whereas the 95W films grew towards the

(622) peak. This difference could be a result of the different oxygen contents of the films, with the 95W results containing a higher oxygen concentration than those at 100W. The as deposited films show a clear distinction between the two films, with the 100W ITO having a second peak at (123). This same structure was seen in the as deposited baseline ITO films in Figure 5.7. While the two films show the same peaks, the amplitude of the baseline ITO was weaker than that of the 100W films. Since the baseline as deposited films were more transmissive and less conductive than the 100W films, then it can be concluded that the increased crystallinity of these peaks could correspond to better conduction. However, since the transmission of the films increases along with the crystallinity at higher and longer anneal temperatures, the same conclusion cannot be reached for the transmission.

Additionally, the longer the anneal time allowed for greater crystal growth in both sets of films. This can be seen most clearly in Figure 5.25. After the 1 hour anneal at either temperature, the (622) peak started to lessen while other peaks emerged. After the 2 hour anneal, the (622) peak was gone, with the (222) preferential peak now the dominant signal. For the 95W films, there appears to be a transition point between 200 and 230°C. At 200°C, there is little change in the structure of the annealed samples. At 230°C, however, the (222), (123), and (400) peaks begin to form, indicating their growth is temperature dependent. Overall, the 100W, 2 hour, and 230°C film yielded the most conductive and crystalline film whereas the 95W film with the same post deposition anneal had the highest transmission.

5.3.2 Design B

The 100W deposition from Design A was compared against the same deposition done with a lower oxygen flow rate, as discussed in Section 4.1.3. The resulting films from this deposition were annealed at 200 and 230°C, with an additional 250°C anneal done as a one off test. The results of these anneals can be seen in Figure 5.26.

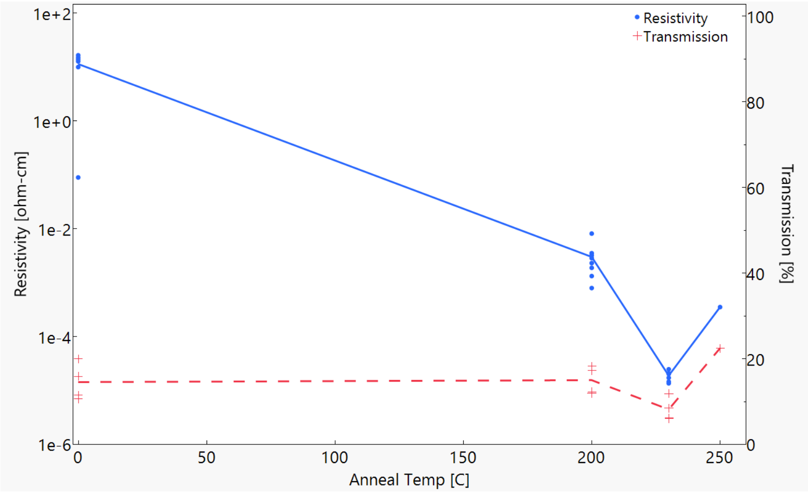

Figure 5.26: Resistivity and Transmission by Anneal Temperature for Design B Depositions, Power of 100W with Reduced O_2 Flow.

The as deposited films with low O_2 flow had poor conductivity and transmission, demonstrating that while the partial pressures remained unchanged, the flow of gas into the chamber has a drastic impact on the film quality. When comparing Figures 5.13 and 5.26, the as deposited films had comparable transmissions, yet the higher O_2 flow films had significantly lower resistivities. As both sets of films were annealed, they both displayed the same resistivity dip at 230°C, and subsequent increase at 250°C. This could be caused by additional oxygen being taken into the film at 250°C, as there are increases in transmission seen in both Figures 5.13 and 5.26. Therefore, 230°C could be a high enough temperature to shift the structure of the film, but not high enough to incorporate substantial amounts of oxygen into the film.

The same statistical analysis done in Design A was carried out for Design B, with the generated results shown in Figures 5.27 to 5.33.

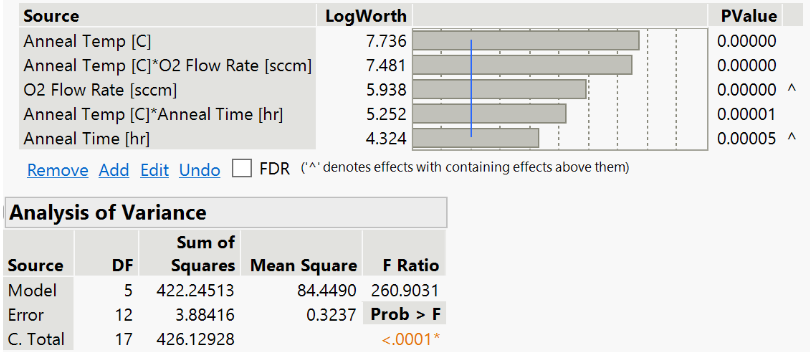

Source	LogWorth		PValue	
Anneal Temp [C]	7.736		0.00000	
Anneal Temp [C]*O2 Flow Rate [sccm]	7.481		0.00000	
O2 Flow Rate [sccm]	5.938		0.00000	^
Anneal Temp [C]*Anneal Time [hr]	5.252		0.00001	
Anneal Time [hr]	4.324		0.00005	^

('^' denotes effects with containing effects above them)

Analysis of Variance

Source	DF	Sum of Squares	Mean Square	F Ratio
Model	5	422.24513	84.4490	260.9031
Error	12	3.88416	0.3237	**Prob > F**
C. Total	17	426.12928		<.0001*

Figure 5.27: Statistical Analysis of Design B for Resistivity.

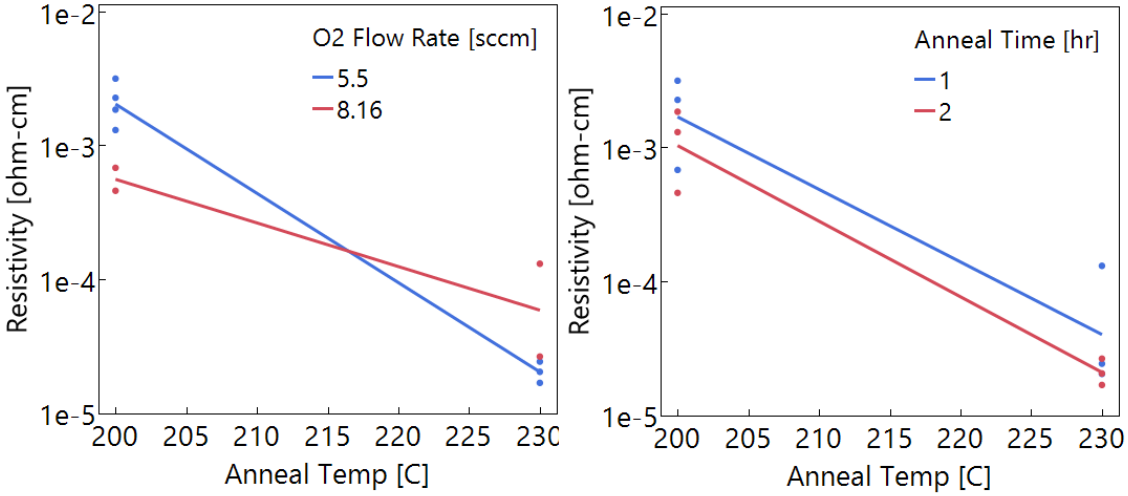

Figure 5.28: Interaction Plots for 2-Factor Effects for Resistivity.

All three main effects and two of the two factors effects were statistically significant. The anneal temperature appears to have the largest impact, followed by the change in gas flow. Seen in Figure 5.28, there is a clear interaction between the O_2 flow rate and the anneal temperature, with the lower oxygen flow films reacting more strongly to a 230°C anneal than at 200°C. There is no interaction between the anneal time and temperature, defined by the parallel lines. Additionally, the ANOVA table in Figure 5.27 shows the model is statistically significant. To minimize the resistivity of Design B, a flow rate of 5.5 sccms of O_2, anneal temperature of 230°C, and 2 hour anneal time should be used.

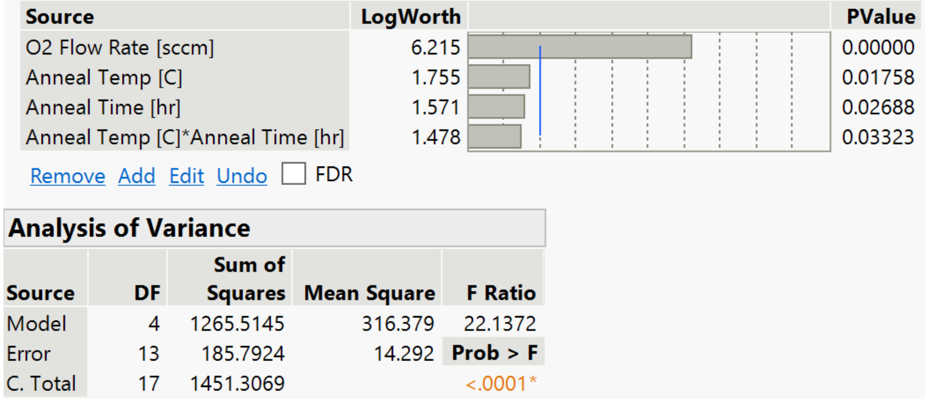

Source	LogWorth		PValue
O2 Flow Rate [sccm]	6.215		0.00000
Anneal Temp [C]	1.755		0.01758
Anneal Time [hr]	1.571		0.02688
Anneal Temp [C]*Anneal Time [hr]	1.478		0.03323

Analysis of Variance

Source	DF	Sum of Squares	Mean Square	F Ratio
Model	4	1265.5145	316.379	22.1372
Error	13	185.7924	14.292	**Prob > F**
C. Total	17	1451.3069		<.0001*

Figure 5.29: Statistical Analysis of Design B for Transmission.

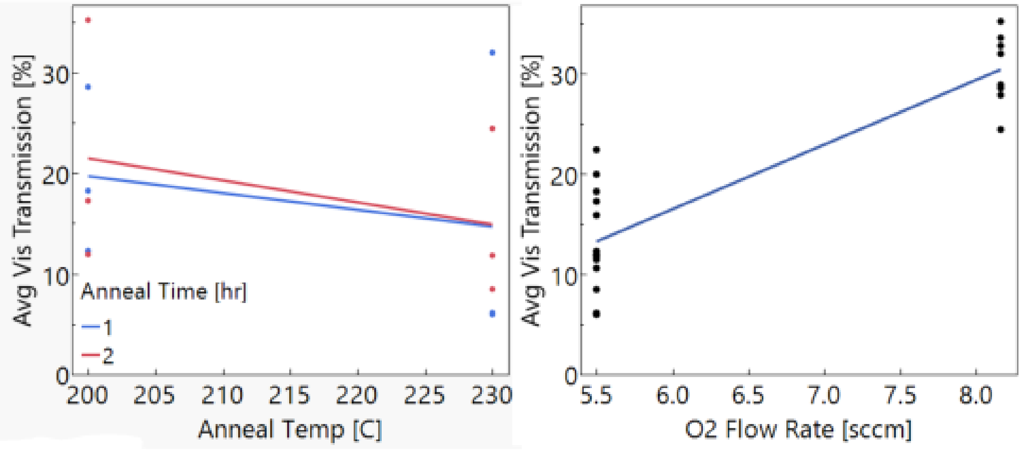

Figure 5.30: Design B Interaction Plots for 2-Factor Effects for Transmission.

For the transmission, the three main effects and the anneal time-temperature 2 factor effect are all significant, with the flow rate being the dominant effect. The ANOVA table shows a statistically significant model, allowing for continued analysis. Using Figure 5.30, there is no interaction seen between the anneal time and temperature. To maximize the transmission of the Design B films, a flow rate of 8.16 sccms, anneal temperature of 200°C, and 2 hour anneal time should be used. It should be noted that there is significant variation in the transmission of the annealed films, with the anneal time having less of an impact than the temperature. Additionally, while 230°C has typically been used to achieve the best transmission, as noted in Figure 5.26, there is a noticeable dip in the transmission at this temperature for the films deposited at 100W.

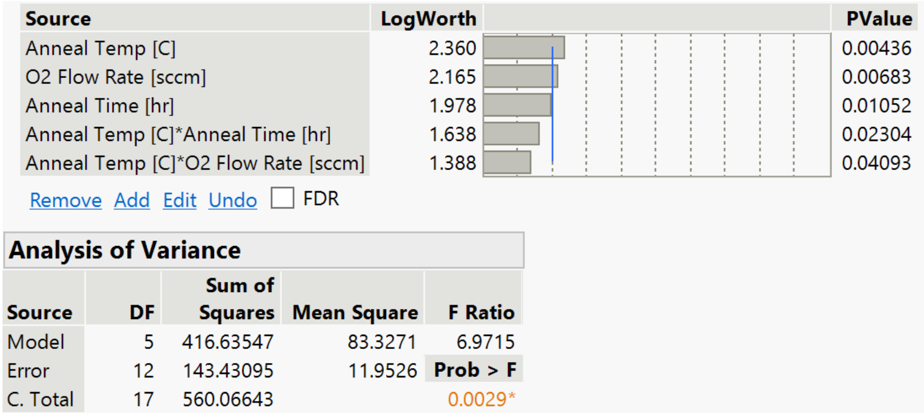

Source	LogWorth		PValue
Anneal Temp [C]	2.360		0.00436
O2 Flow Rate [sccm]	2.165		0.00683
Anneal Time [hr]	1.978		0.01052
Anneal Temp [C]*Anneal Time [hr]	1.638		0.02304
Anneal Temp [C]*O2 Flow Rate [sccm]	1.388		0.04093

Analysis of Variance

Source	DF	Sum of Squares	Mean Square	F Ratio
Model	5	416.63547	83.3271	6.9715
Error	12	143.43095	11.9526	Prob > F
C. Total	17	560.06643		0.0029*

Figure 5.31: Statistical Analysis of Design B for Thickness Non-uniformity.

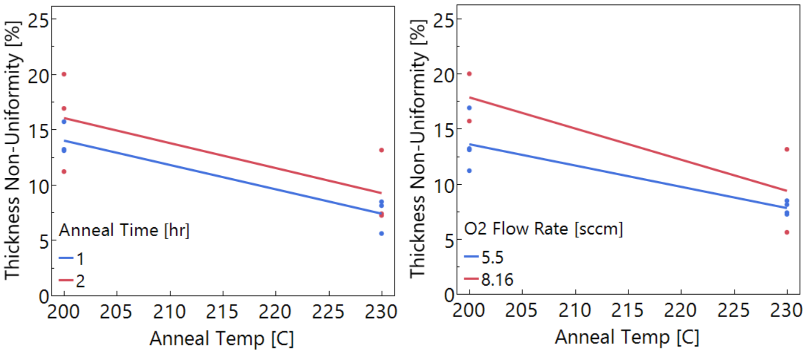

Figure 5.32: Design B Interaction Plots for 2-Factor Effects for Thickness Non-Uniformity.

For the thickness non-uniformity, all three main effects and two 2-factor effects are significant. The ANOVA table again shows the model is statistically significant. The interaction plots for both the anneal temperature by time and the anneal temperature by flow rate indicate no interaction, each having a set of parallel lines shown in Figure 5.32. The anneal temperature is the dominating factor in both of the two factor effects. To minimize the thickness non-uniformity, an O_2 flow rate of 5.5 sccms, anneal time of 1 hour, and anneal temperature of 230°C should be used.

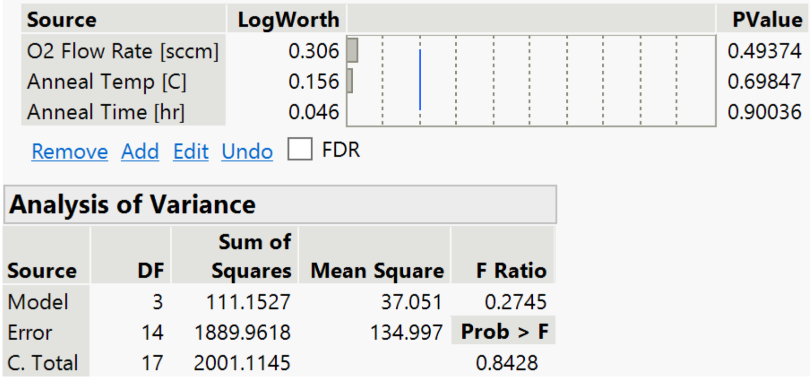

Source	LogWorth		PValue
O2 Flow Rate [sccm]	0.306		0.49374
Anneal Temp [C]	0.156		0.69847
Anneal Time [hr]	0.046		0.90036

Analysis of Variance

Source	DF	Sum of Squares	Mean Square	F Ratio
Model	3	111.1527	37.051	0.2745
Error	14	1889.9618	134.997	Prob > F
C. Total	17	2001.1145		0.8428

Figure 5.33: Statistical Analysis of Design B for Sheet Resistance Non-uniformity.

The analysis of the sheet resistance non-uniformity, shown in Figure 5.33, indicates there are no significant effects. Additionally, the ANOVA table concludes that there is not any statistically significant factors, therefore there the R_{SH} non-uniformity is primarily driven by random variation or some other factor.

Overall, there are significant conflicts when trying to both minimize the resistivity and maximize the transmission. Both call for opposite gas flow and anneal conditions to be used. The same reasoning used for Design A is applicable for Design B, with the transmission being favored over the resistivity due to its impact on the functionality of the solar cell. Therefore, for Design B, the ideal sputter conditions would be the same as those used to maximize the transmission: an oxygen flow of 8.16 sccms, an anneal temperature of 200°C, and anneal time of 2 hours. The impact of lowering the oxygen gas flow is evident in the characteristics of the film. It can also be seen in XRD scans of the crystalline structure, shown in Figure 5.34.

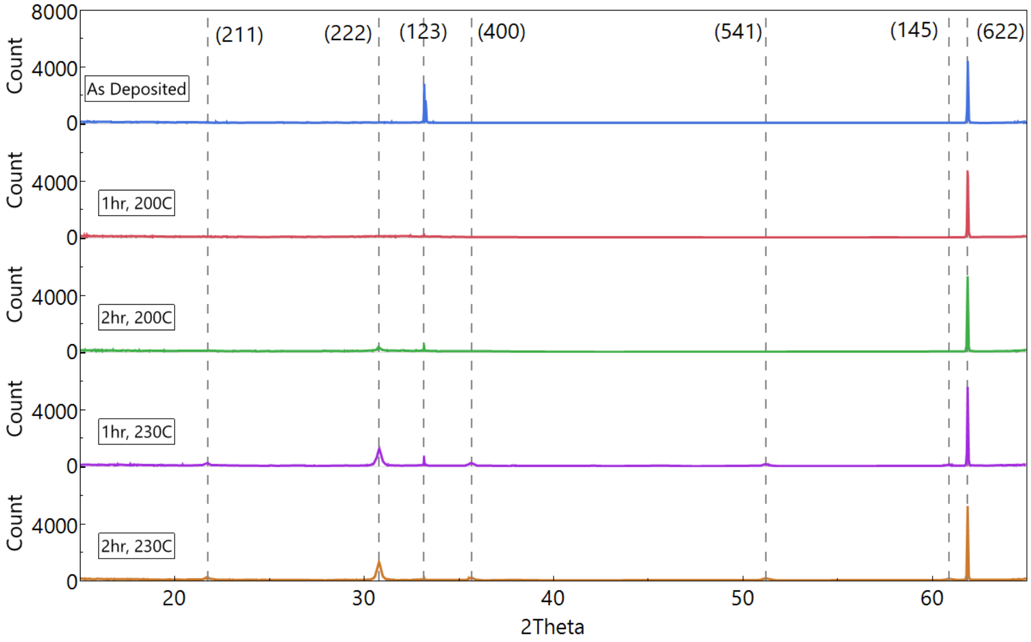

Figure 5.34: X-Ray Diffraction Results for Design B, 100W & Low O_2 Gas Flow Depositions by Anneal Temperature and Time.

While the as deposited film has the same peaks as both the higher oxygen flow film in Design A and the baseline ITO film, its reaction to the post deposition anneal is different from either. In Design A, the 100W film had its (622) peak decrease as more heat was applied. For this film, the (622) peak shows a slight decrease after 2 hours of 230°C, but is still the preferential peak. The (222) peak is also present in the 230°C anneal, but is noticeably missing at the 200°C. This pattern was also seen in the 95W Design A films, despite the 95W ITO being more transmissive and less conductive compared to the lower oxygen flow Design B film. The 230°C temperature, for the 100W films, denotes a transition point, where there is a sharp increase in conductivity and the growth of new crystallographic peaks.

5.3.3 Design C

Design C uses the same deposition parameters as Design A, but instead of only using glass slides, Si wafers with a layer of thermally grown SiO_2 were included. This was done to experimentally determine if the type of substrate used as an anode during the sputter process impacts the resulting film. The oxide layer was used to electrically isolate the ITO film from the Si wafer. Transmission measurements could not be taken for the films sputtered onto the Si wafers and is not analyzed in this design. As with Designs A and B, JMP was used to analyze the active effects of Design C, seen in Figures 5.35 to 5.38.

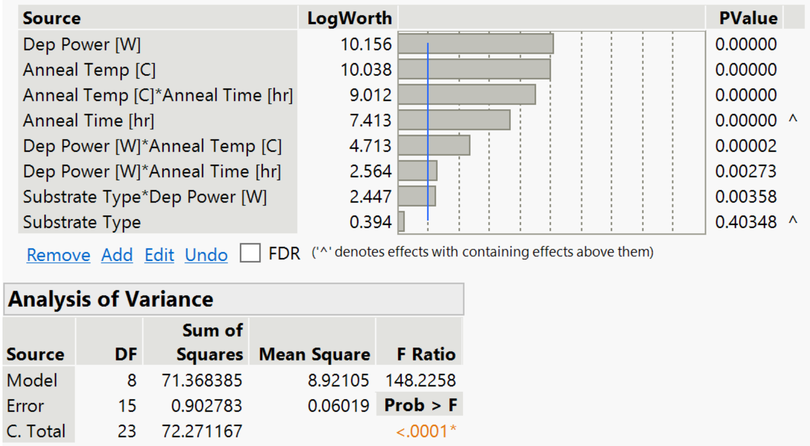

Source	LogWorth	PValue	
Dep Power [W]	10.156	0.00000	
Anneal Temp [C]	10.038	0.00000	
Anneal Temp [C]*Anneal Time [hr]	9.012	0.00000	
Anneal Time [hr]	7.413	0.00000	^
Dep Power [W]*Anneal Temp [C]	4.713	0.00002	
Dep Power [W]*Anneal Time [hr]	2.564	0.00273	
Substrate Type*Dep Power [W]	2.447	0.00358	
Substrate Type	0.394	0.40348	^

Remove Add Edit Undo ☐ FDR ('^' denotes effects with containing effects above them)

Analysis of Variance

Source	DF	Sum of Squares	Mean Square	F Ratio
Model	8	71.368385	8.92105	148.2258
Error	15	0.902783	0.06019	**Prob > F**
C. Total	23	72.271167		<.0001*

Figure 5.35: Statistical Analysis of Design C for Resistivity.

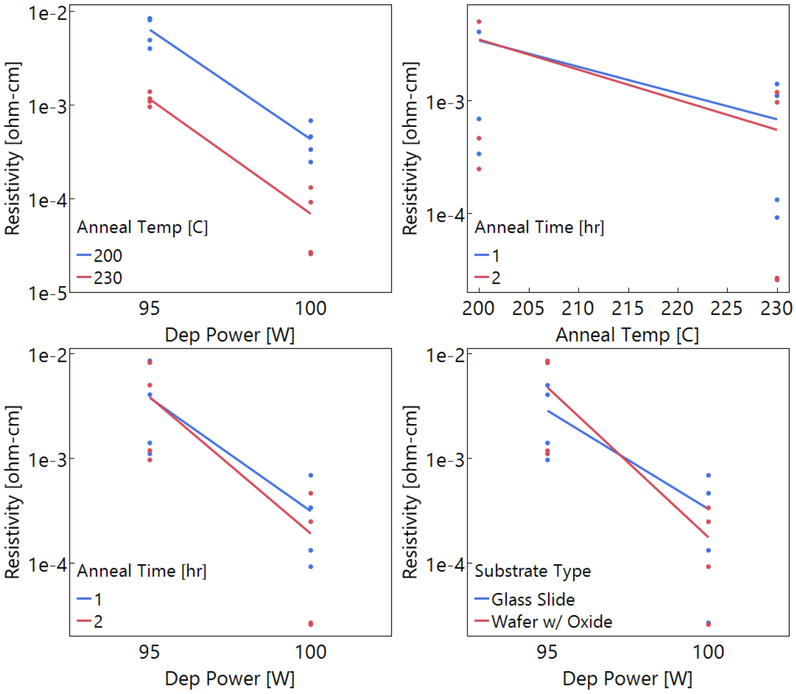

Figure 5.36: Design C Interaction Plots for 2-Factor Effects for Resistivity.

The active effects on the resistivity are fairly similar to that of Design A, with the same main and two factor effects significant. With the addition of the Si wafers, the substrate type and power two factor effect is also significant, though the substrate type on its own is not. The ANOVA table indicates a statistically significant model. Figure 5.36 depicts the interaction between the multiple significant two factor effects. The anneal temperature by power plot shows no interaction between the two effects. For the anneal time by power and anneal time by temperature interaction plots, there is no interaction as well. There is a clear interaction between the substrate type and the deposition power used. To minimize the resistivity, the following parameters should be used: a power of 100W, anneal temperature of 230°C, anneal time of 2 hours, and a Si wafer with a layer of oxide as the substrate.

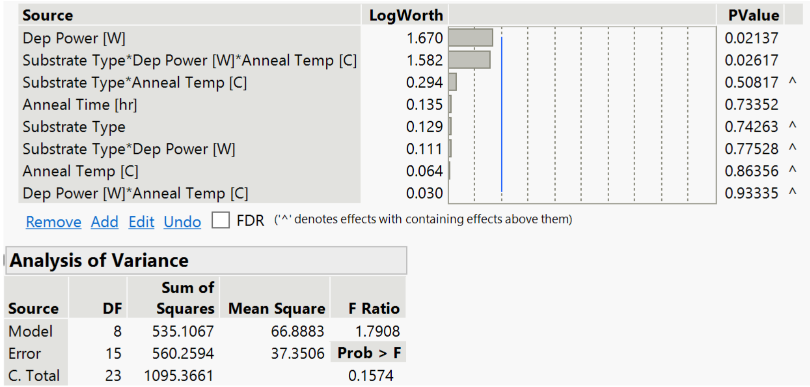

Source	LogWorth	PValue	
Dep Power [W]	1.670	0.02137	
Substrate Type*Dep Power [W]*Anneal Temp [C]	1.582	0.02617	
Substrate Type*Anneal Temp [C]	0.294	0.50817	^
Anneal Time [hr]	0.135	0.73352	
Substrate Type	0.129	0.74263	^
Substrate Type*Dep Power [W]	0.111	0.77528	^
Anneal Temp [C]	0.064	0.86356	^
Dep Power [W]*Anneal Temp [C]	0.030	0.93335	^

('^' denotes effects with containing effects above them)

Analysis of Variance

Source	DF	Sum of Squares	Mean Square	F Ratio
Model	8	535.1067	66.8883	1.7908
Error	15	560.2594	37.3506	Prob > F
C. Total	23	1095.3661		0.1574

Figure 5.37: Statistical Analysis of Design C for Thickness Non-uniformity.

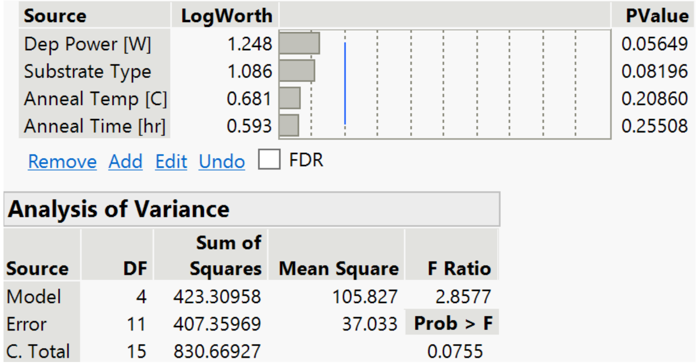

Source	LogWorth	PValue
Dep Power [W]	1.248	0.05649
Substrate Type	1.086	0.08196
Anneal Temp [C]	0.681	0.20860
Anneal Time [hr]	0.593	0.25508

Analysis of Variance

Source	DF	Sum of Squares	Mean Square	F Ratio
Model	4	423.30958	105.827	2.8577
Error	11	407.35969	37.033	Prob > F
C. Total	15	830.66927		0.0755

Figure 5.38: Statistical Analysis of Design C for Sheet Resistance Non-uniformity.

For both the thickness and sheet resistance non-uniformity analyses, shown in Figure 5.37 and Figure 5.38, the ANOVA tables indicate no difference between the means of the variance of the levels. No further analysis could be done due to this.

The results of Design C indicates that the type of substrate used impacts the sputtered film as the deposition power changes. This could indicate that the film nucleates differently on the SiO_2 film as opposed to a commercial glass slide. It appears that the non-uniformity for both thickness and R_{SH} is driven by either random variation or some other factor not included in this design.

5.4 Solar Cell ARC

Using the methods described in Section 4.2.2, three wafers, wafers 3, 4, and 5, were sputtered with ITO as an anti-reflective coating. The final results can be seen in the wafer below in Figure 5.39.

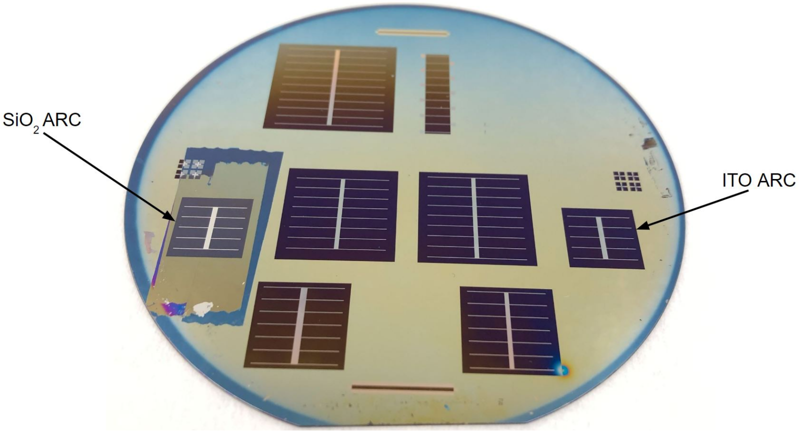

Figure 5.39: Completed Solar Cell With ITO ARC.

As discussed in Section 4.2.2, cell number 2 was taped over using Kapton tape, preserving the SiO_2 ARC. Since cells 2 and 5 have the same exact layout, the comparison between the two cells would allow the ITO's impact to be characterized. The ITO was sputtered as the last step of the process, after the front metal contacts had been lifted off and initial TLM testing was done. To determine what deposition parameters were used for the ITO ARC, Figure 5.40 was used.

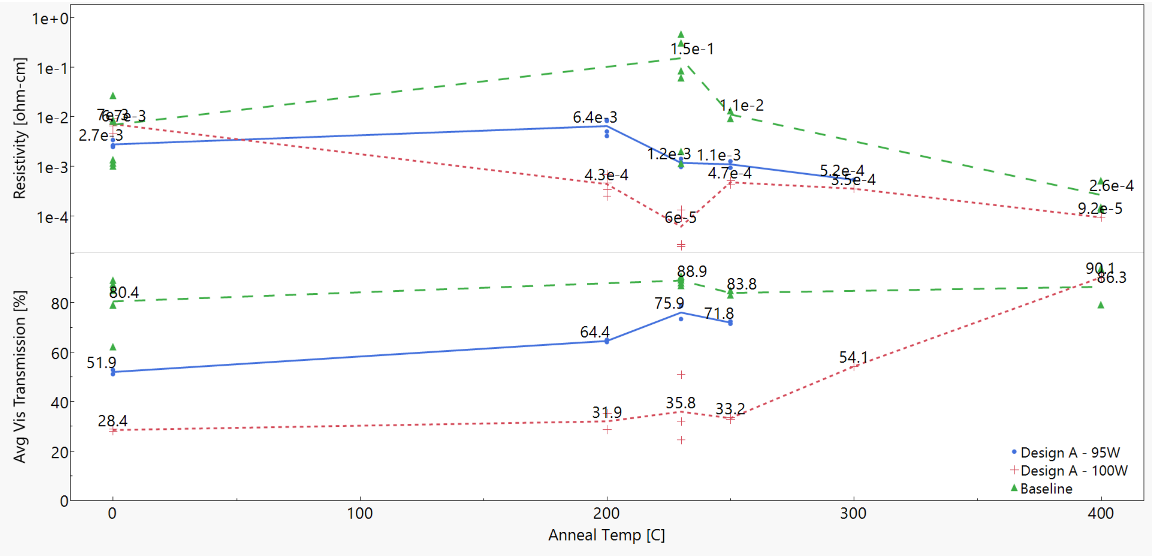

Figure 5.40: Summarized Results of ITO Anneal Studies Compared to The Baseline Process.

The optimal ARC coating of ITO would have strong transmission in the visible spectra and good conductivity. While the baseline process had good transmission at lower temperatures, the higher resistivity left room for improvement. The 100W film from Designs A and C was the opposite of the baseline, having low transmission and a very low resistivity. The 95W deposition from Designs A and C served as an intermediary, having good transmission after a 230°C anneal coupled with low resistivity. At the maximum temperature of 400°C, the Design A, 100W films outperformed the baseline films in both transmission and resistivity. That being said, it was theorized that the post deposition anneal should be no higher than 300°C, due to the possible formation of Ti silicides in the solar cell. Therefore, the 95W deposition parameters used in Designs A and C was picked to be used for the ITO ARC, with a post deposition anneal of 230°C for 1 hour. The 95W deposition process also had the advantage of being faster than the baseline process, in terms of sputter rate and length of the post deposition anneal. The sputter rate at a power of 95W with a moving platen over the target was 1.29 Å/s, significantly higher than the 0.6 Å/s rate of the baseline process. The lower deposition rate of the baseline sputter is due to the pulsed sputter mode necessitated by the dielectric target. The baseline post deposition anneal, 2 hours at 400°C, took 4 hours in total, as the furnace warm up and ramp down took 2 hours on their own. Compared to the oven used for the 230°C anneal, the small box oven could be heated up in around 30 minutes. While the 95W was less transmissive, the better conductivity and approximately 2 hours saved in processing time is substantial.

Just prior to this experiment, a power outage in the RIT cleanroom, damaged the Baratron used to track the pressure during deposition. The replacement unit was less precise as it did not measure the pressure to a tenth of a mT as the original one had. Since the ideal processing window determined in Section 5.2 was dependent on 0.8mT of oxygen, replication of this window proved to be a challenge. The gas flow of the Ar and O_2 were set to the same values used for the 95W depositions in Design A, with the throttle valve being used to achieve the proper approximate sputter pressure. This method was used for screening depositions to be done prior to sputtering of the solar cells. A glass slide and bare Si wafer were used for the test runs. The sputter test runs can be seen below in Table 5.4, with Run 30 being the sputter of the solar cells. The initial target thickness of the ITO films was set to 69nm, as calculated in Section 4.2.2.

Table 5.4: Results For Test Depositions for Solar Cell ARC.

Dep #	Time [s]	Pwr [W]	Ar [sccms]	O_2 [sccms]	t [Å]	R_{SH} [Ω/□]	T [%]	n
27	580	95	56	8	544	-	84.88	1.992
28	580	100	56	8	532	-	83.38	1.998
29	640	100	56	6	685	710	66.32	2.175
29 (Anneal)	-	100	56	6	673	60	73.30	1.873
30	600	100	56	6	622	654	63.95	2.064
30 (Anneal)	-	100	56	6	642	71.73	75.76	1.849

Sputter run 27 was using the same deposition parameters as the 95W sputters in Design A. While the net sputter pressure was consistent, 12mT, the exact breakdown between Ar and O_2 partial pressures was uncertain. The Ar gas flow consisted of at least 11mT of the sputter pressure, with the oxygen accounting for the remainder. Results of Run 27 show a non-conductive film with high transmission, indicating an over-saturation of oxygen. As seen in the screening deposition results, the difference between 0.8mT and 1mT of oxygen PP was drastic, resulting in either transmissive and conductive or glass-like films respectively. This same effect was likely at play in Run 27. For run 28, a higher deposition power was used to lessen the amount of oxygen in the film and increase the sputter rate. However, the film was still non-conductive, meaning there was a significant amount of oxygen more than initially estimated. For the subsequent deposition, the flow of oxygen was decreased, yielding a conductive and transmissive film. A 1 hour 230°C anneal was done, showing a noticeable improvement in conductivity and transmission. The refractive index was also impacted by the increased oxygen content in the film. Using the annealed refractive index from run 29, the optimal ARC thickness was recalculated to a value of 667.4 Åfor a wavelength of 500 nm. Run 30 repeated the conditions of run 29 and resulted in minor variation, ultimately yielding an annealed film with an R_{SH} of 71.73 Ω/□ and a transmission of 75.76%. Only wafer 5 was annealed in this way, with wafers 3 and 4 receiving the as deposited films of run 30.

TLM data was collected before and after the ITO was sputtered. A fit line was generated for the collected data, which is graphed in Figures 5.41 to 5.43. The contact resistance, transfer length, contact resistivity, and sheet resistance for all of the wafers were calculated and extracted from the graphed results using the equations and methods from Section 4.2.2. The extracted parameters are summarized in Table 5.5.

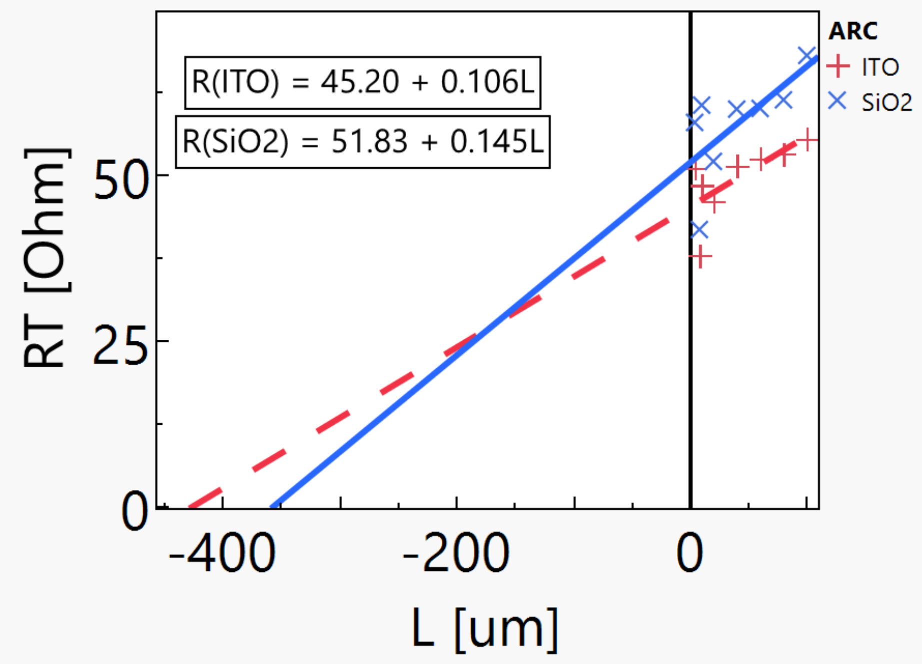

Figure 5.41: Impact of Annealing ITO on Transmission Line Measurement Results of Wafer 3.

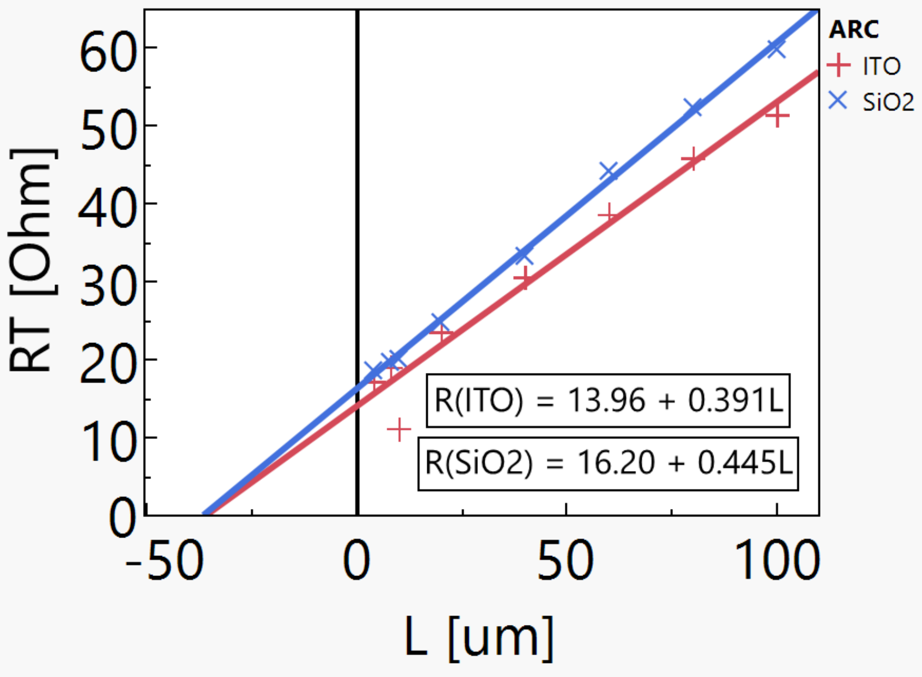

Figure 5.42: Impact of Annealing ITO on Transmission Line Measurement Results of Wafer 4.

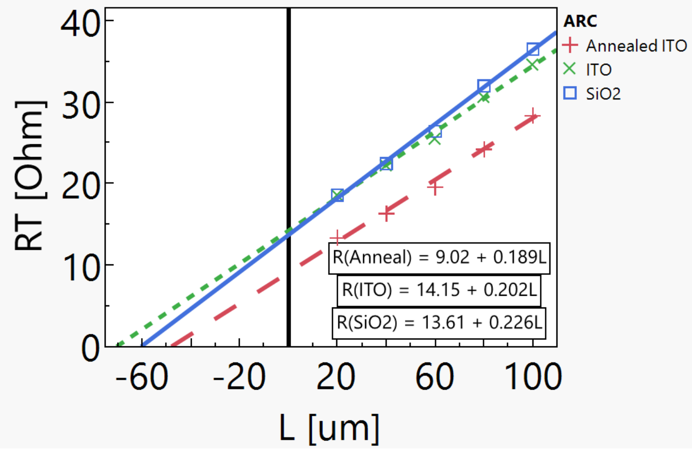

Figure 5.43: Impact of Annealing ITO on Transmission Line Measurement Results of Wafer 5.

Table 5.5: Summarized TLM Results & Impact of ARC Material

Wfr	ARC	R_C [Ω]	L_T [μm]	R_{SH} [Ω/□]	ρ_C [Ωcm^2]	Equation
3	SiO_2	25.92	178.72	14.50	$4.63\text{x}10^{-3}$	51.83 + 0.145L
3	ITO	22.60	213.21	10.60	$4.82\text{x}10^{-3}$	45.20 + 0.106L
4	SiO_2	8.10	18.20	44.51	$1.47\text{x}10^{-4}$	16.20 + 0.445L
4	ITO	6.98	17.85	39.10	$1.25\text{x}10^{-4}$	13.96 + 0.391L
5	SiO_2	6.81	30.11	22.62	$2.05\text{x}10^{-4}$	13.61 + 0.226L
5	ITO	7.08	35.02	20.22	$2.48\text{x}10^{-4}$	14.15 + 0.202L
5	Annealed ITO	4.51	23.86	18.90	$1.08\text{x}10^{-4}$	9.02 + 0.189L

The equations displayed on the plotted results and Table 5.5 are of the fitted lines generated from the resistance measurements. It is evident that the ITO had a greater impact on wafers that had a lesser emitter dose. Wafer 3 had the lowest dose, $2\text{x}10^{15}$ cm^2 at an energy of 55 KeV, and showed a 3 Ω decrease in the contact resistance with an ITO ARC. It is also important to notice, in Wafer 3, that the transfer length exceeds the length of the pads of the TLM, 75 μm. This is not possible, since the charge carriers cannot travel a distance greater than the pad length before flowing up into it. The breakdown of the TLM model could be due to the high resistance of the substrate itself caused by the low doping profile. The results of wafers 4 and 5 do not indicate a model breakdown, pointing towards an issue specific to wafer 3. Wafer 4 showed a slight but distinct improvement with an ITO ARC. Since Wafer 4 already had a higher carrier concentration at the wafer surface due to the split profile, the resistance was already low prior to the ITO deposition and was less impacted. Wafer 5 was the only film that underwent a post deposition anneal, with TLM data being collected prior to the sputter and anneal. The heat treated ITO showed a significant contact resistance and transfer length decrease, yielding a better contact overall. Using this information, it would appear the increased transmission and improved contact resistance of the annealed ITO film would yield a solar cell with high performance. This assumption was further investigated once the fabricated cells were tested using a solar simulator configured for AM1.5 illumination, the results of which can be seen summarized in Table 5.6 and graphically in the I-V curves in Figures 5.44 to 5.46.

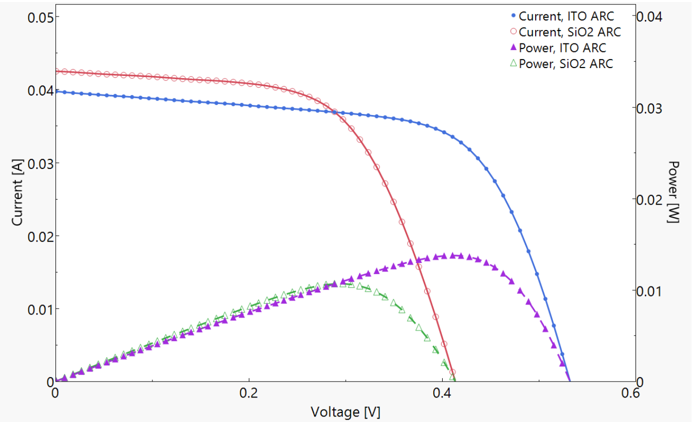

Figure 5.44: AM 1.5 I-V Curve For Wafer 3, SiO_2 vs ITO ARC.

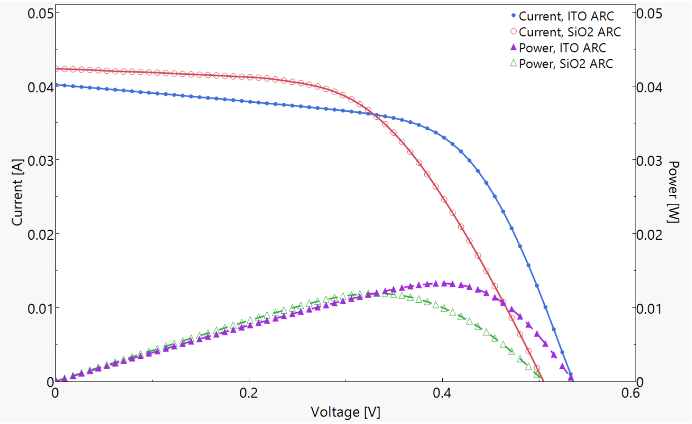

Figure 5.45: AM 1.5 I-V Curve For Wafer 4, SiO_2 vs ITO ARC.

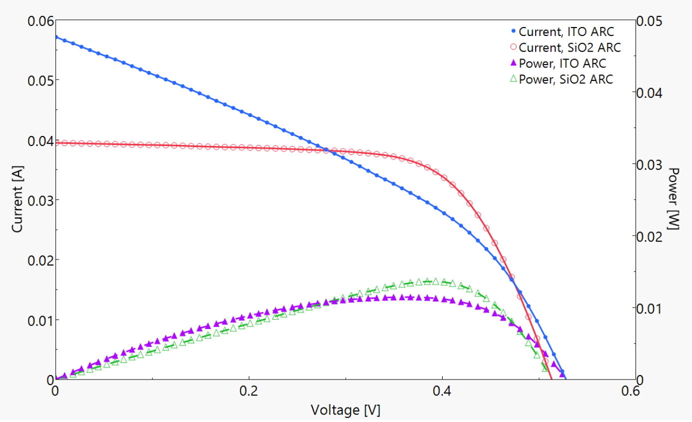

Figure 5.46: AM 1.5 I-V Curve For Wafer 5, SiO_2 vs ITO ARC.

Table 5.6: Summarized Results of Solar Cells Based on ARC.

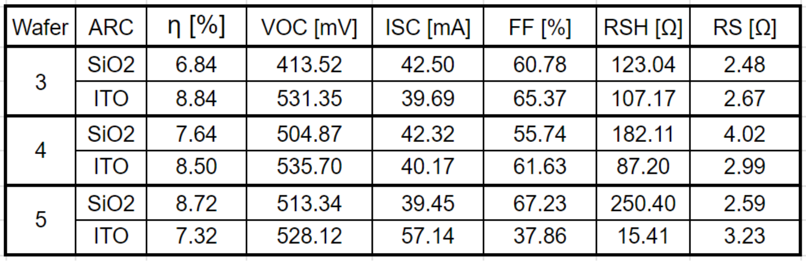

Wafer	ARC	η [%]	VOC [mV]	ISC [mA]	FF [%]	RSH [Ω]	RS [Ω]
3	SiO2	6.84	413.52	42.50	60.78	123.04	2.48
	ITO	8.84	531.35	39.69	65.37	107.17	2.67
4	SiO2	7.64	504.87	42.32	55.74	182.11	4.02
	ITO	8.50	535.70	40.17	61.63	87.20	2.99
5	SiO2	8.72	513.34	39.45	67.23	250.40	2.59
	ITO	7.32	528.12	57.14	37.86	15.41	3.23

The results in Table 5.6 are for cells number 2 and 5, with cell 2 having a SiO_2 ARC and cell 5 having an ITO ARC and were extracted from the I-V curves. It can be seen that the as deposited ITO films, on wafers 3 and 4, shows good η and FF. However, the ITO cells also have a lower short circuit current than their SiO_2 counterparts. This indicates that the ITO films improves carrier collection, seen by the higher FF, but decreases the number of electron-hole pairs generated, seen in the lower I_{SC}. Since the ITO films are not 100% transmissive, the loss of carriers can be attributed to the incident light that is reflected or absorbed by the ITO top layer. These losses, however, did not diminish the efficiency of these cells, which showed efficiencies of 8.84 and 8.50%. The low V_{OC} seen in the SiO_2 cell of wafer 3 indicates there could be some defect degrading the open circuit voltage of that cell. The defect could be a charge trapping state caused by a contaminate in the SiO_2 ARC, which could have originated from oxide furnace the layer was grown in. While the V_{OC} between SiO_2 and ITO cells in wafers 4 and 5 are more comparable, there still could be some contaminate impacting their performance, making accurate comparisons between the two ARC layers more difficult. To check for this possible issue, additional SiO_2 reference cells could be fabricated using a different oxidation furnace to check if the V_{OC} was still degraded in any way.

The shunt resistance, R_{SH}, and series resistance, R_S, of the cells were extracted from the I-V curves by take the negative inverse of the slope near the y and x intercepts respectively. R_{SH} indicates if there is any lower resistance path circumventing the intended path and R_S is the sum total of all the parasitic resistances of the contacts, semiconducting material, and solar cell as a whole. Both values are parasitic resistances, with the ideal R_{SH} being maximized and R_S minimized. Looking at wafers 3 and 4, it appears that the ITO ARC results in a lower R_{SH}. This could be a result of the ITO, which was coated across the entire surface of the wafer, interacting with neighboring cells. Cleaving the solar cells into individual units could improve the shunt resistance. For the series resistance, the ITO did not show as large an improvement as was expected. This could indicate that the majority of the series resistance could be coming from another source or that a more conductive ITO film is necessary.

Wafer 5, with the heated treated ITO ARC, showed a noticeable decrease in performance when compared to the oxide ARC. Noticeably, the I_{SC} showed significant improvement while the FF and R_{SH} deteriorated greatly. The increased carrier generation could be a result of the improved transmission of the annealed ITO. The poor FF is driven by the low shunt resistance. It was initially speculated that the 1 hour, 230°C anneal was either too high a temperature or too long of a treatment, resulting in the creation of Ti silicides at the Ti/Si interface. However, since both the SiO_2 and ITO cells were annealed, any TiSi formation would also be present in the SiO_2 cell, which, as seen in Figure 5.43, does not show signs of degradation. Therefore, it can be concluded that specifically the annealed ITO was causing the decrease in performance. The lowering of the resistivity of the ITO top coat could have increased the interaction between the solar cell, the surrounding field oxide, and neighboring cells. There could also be interactions between the Sn and the Ti or Al, as the 230°C anneal temperature corresponds to not only the Sn melting point, but points of new structural formations in the Sn-Ti and Sn-Al phase diagrams, seen in Figures 5.47 and 5.48. Cleaving the ITO cell into an individual unit and annealing the solar cell at a lower temperature could yield beneficial insight into the factors that affected this degradation.

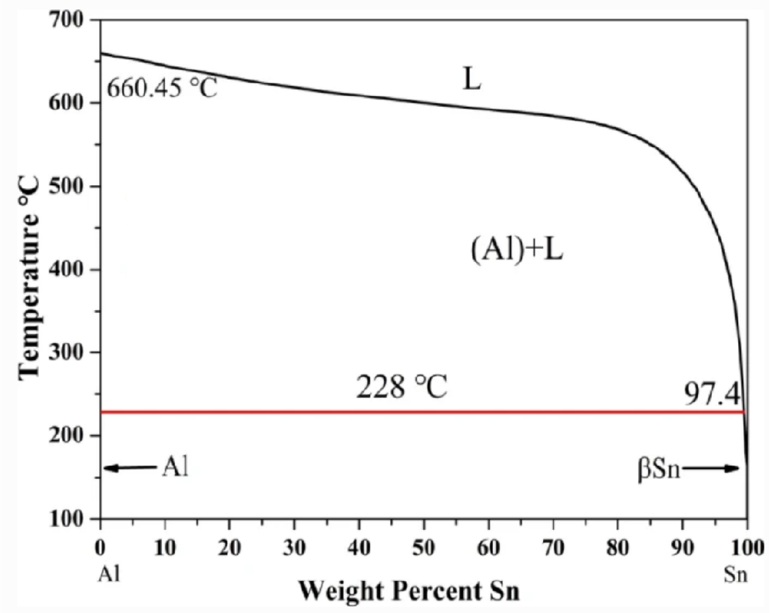

Figure 5.47: Sn-Ti and Sn-Al Phase Diagrams [62, 63].

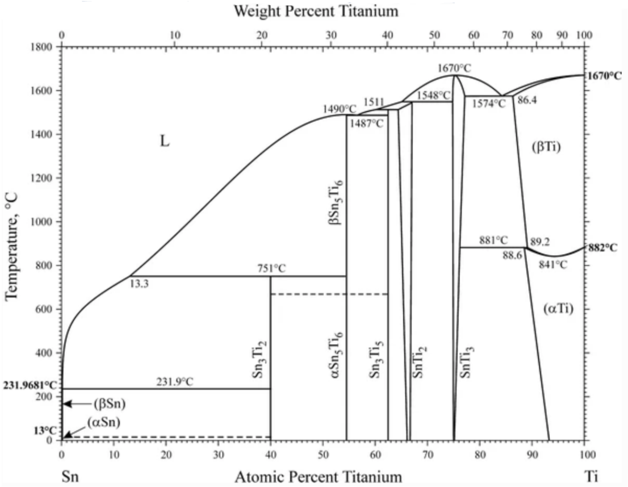

Figure 5.48: Sn-Ti and Sn-Al Phase Diagrams [63].

Table 5.7: Impact of Cell Dimensions and Shadowing on Solar Cell Metrics.

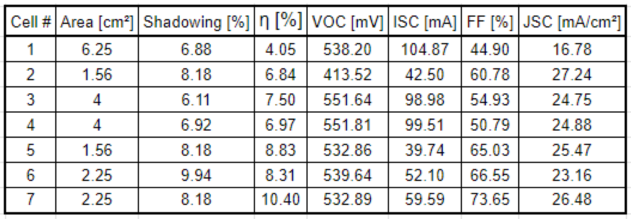

Cell #	Area [cm²]	Shadowing [%]	η [%]	VOC [mV]	ISC [mA]	FF [%]	JSC [mA/cm²]
1	6.25	6.88	4.05	538.20	104.87	44.90	16.78
2	1.56	8.18	6.84	413.52	42.50	60.78	27.24
3	4	6.11	7.50	551.64	98.98	54.93	24.75
4	4	6.92	6.97	551.81	99.51	50.79	24.88
5	1.56	8.18	8.83	532.86	39.74	65.03	25.47
6	2.25	9.94	8.31	539.64	52.10	66.55	23.16
7	2.25	8.18	10.40	532.89	59.59	73.65	26.48

As discussed in Section 4.2.2, the dimensions and design of the cells were varied to study the impact on cells performance. The summarized results of each cell on wafer 3 are shown in Table 5.7. Cell 1 was the largest solar cell and performed worst. This was driven by the front contacts, which were not thick enough to collect the generated current, further demonstrated by the poor fill factor. Cells 3 and 4 had the same area, but cell 4 had additional metal fingers to better collect carriers. Table 5.7 shows the increased shadowing and subsequent blocking of incident light had a detrimental effect on the fill factor, decreasing the efficiency overall, but appeared to have little impact on the I_{SC}. A similar experiment was done using cells 6 and 7, with cell 6 having a thicker busbar. There is a sizable difference between the I_{SC} of these cells, with increased shadowing reducing the carriers generated. Cell 7 yielded the best characteristics, with a high FF and current density, demonstrating that the trade off between increased contact area was not worth the cost of additional shadowing. Cells 2 and 5 had the same front contact dimensions and different ARC materials as discussed above. While cells 5 and 7 have the same shadowing percentage, the higher fill factor and current density of the larger cell yielded a better efficiency. This demonstrates the optimal configuration for the ITO ARC device, with a lower percentage of shadowing and moderate area.

Chapter 6

Conclusion & Future Work

A low temperature process to sputter an indium tin oxide thin film in the RIT facility was successfully developed. The low thermal budget process was centered around a 4” InSn metal sputter target. Experiments investigating the deposition of oxygen starved, transmissive, and conductive ITO films resulted in the development of a processing window with a sputter pressure combination of 11.2mT Ar and 0.8mT O_2 at either 95 or 100 Watts. Anneal studies were conducted at 200 and 230°C for 1 and 2 hours in compressed dry air. By annealing these oxygen deprived films, significant improvement in the qualities of these films were noted. After a 2 hour, 230°C anneal, films deposited at 95W showed an increase in transmission from 51.9 to 78.5% while their resistivities dropped from $2.7\text{x}10^{-3}$ to $9.6\text{x}10^{-4}\Omega\text{cm}^2$. When the 100W films were annealed with the same conditions as the 95W films, their transmission showed a slight increase from 28.4 to 35.8% while their resistivities sharply decreased from $6.7\text{x}10^{-3}$ to $6\text{x}10^{-4}$. The difference between the as deposited 100W and 95W films is apparent, as is the different reactions to the post deposition anneal. When comparing these values to the baseline process, which had an as deposited and post anneal transmission of 62 and 79%, and a resistivity of $8.4\text{x}10^{-3}$ and $5\text{x}10^{-4}\Omega$-cm respectively, it can be seen that the 95W, post 230°C anneal films had better transmission and conductivity than the as deposited baseline and is just as transmissive as the post anneal baseline.

The sputter power also had a significant impact on the crystal structure of the ITO as well as its reaction to anneal treatments. While both 95 and 100W as deposited films showed a preferential (622) peak, as the 100W film was annealed at 230°C for 1 and 2 hours, the (622) peak diminished while a (222) peak grew. For the 95W films, the (622) peak remained the preferential peak even after the 2 hour 230°C anneal, with only minor (222) and (123) peaks forming. Additionally, the 95W films had no structural changes during the 200°C anneal, with new peaks only forming during the 230°C treatment. These differences could be due to different compositions, or oxygen content, of the sputtered films. It was also seen that the underlying substrate had an impact on the resulting peaks. Most notably, the (622) preferential peak was not present in the XRD scans of the films on the fused silica substrates. The peak in question was not a direct result of the Si wafer, as the wafer had an orientation of (100) which occurs at 69°. The scans were taken from a range of 5 to 65 °, avoiding the impact of the Si peak. Therefore, the underlying film or substrate can promote crystal growth in the sputtered film, possibly due to the ITO film attempting to match its lattice structure during deposition.

As a proof of concept, the ITO film was used as an anti reflective coating for solar cells. A low thermal budget process was needed as the cells utilized a Ti/Si front contact interface, where excess heat could cause Ti silicides to form. Three wafers with varied emitter implant doses were successfully fabricated, with a low dose, the same low dose split at different energies, and a higher dose split at different energies were used. The ITO film used as the ARC had a transmission of 64%, thickness of 622Å, refractive index of 2.064, and sheet resistance of 654 $\Omega/\square$. The wafer with the highest dose was annealed at 230°C for one hour, increasing the transmission and decreasing the refractive index and sheet resistance. The un-annealed ITO showed a slight improvement in contact resistance and a 1 to 2% higher efficiency but lower short circuit current. The reduced carrier generation was due to the reflection or absorption of the incident photons in the ITO. The annealed ITO solar cells generated a greater number of carriers, but had a very poor fill factor and shunt resistance, deteriorating the overall performance of the device. This degradation was speculated to be caused by either interactions between the cell being tested and neighboring solar cells or between the Sn in the ITO ARC and the Ti and Al in the front contacts. Further analysis of the annealed cell is necessary to determine the root cause. While a conclusion that the ITO ARC was better than SiO_2 film is not possible with this limited data, the results demonstrate a functional solar cell with reasonable electrical and optical responses.

Additional experiments of sputtered films at lower temperatures or in different atmospheres should be investigated, specifically the use of a nitrogen anneal on a heavily oxidized ITO film to promote conductivity. Etch studies of the as deposited and annealed films can also be done, allowing for easier patterning of the ITO. The impact of the crystal structure and anneal temperature on the etch rate would also have an effect on the low thermal budget process depending on the application of the film. Expansion of the processing window would allow for greater flexibility in what films were deposited and would ideally prevent the reliance on a highly precise gas flow combination to achieve good results. Additionally, the incorporation of other gasses in the plasma during sputtering, such as hydrogen, should be investigated, given the literature on these films not requiring an anneal.

References

[1] Wikipedia, “Transparent conducting films,” Jan 2023. https://en.wikipedia.org/wiki/Transparent_conducting_film.

[2] Wikipedia, “Indium tin oxide,” Jan 2023. https://en.wikipedia.org/wiki/Indium_tin_oxide.

[3] Wikipedia, “Abundance of elements in earth’s crust,” Aug 2022. https://en.wikipedia.org/wiki/Abundance_of_elements_in_Earth%27s_crust.

[4] dailymetalprice, “Daily metal spot prices,” Feb 2023. https://www.dailymetalprice.com/metalprices.php.

[5] R. Kamat, “Engineered emitters for improved silicon photovoltaics,” 2016. Master’s Thesis.

[6] N. R. E. Laboratory, “Reference air mass 1.5 spectra.” https://www.nrel.gov/grid/solar-resource/spectra-am1.5.html.

[7] H. Kim, C. M. Gilmore, A. Piqué, J. S. Horwitz, H. Mattoussi, H. Murata, Z. H. Kafafi, and D. B. Chrisey, “Electrical, optical, and structural properties of indium–tin–oxide thin films for organic light-emitting devices,” *Journal of Applied Physics*, vol. 86, no. 11, pp. 6451–6461, 1999. https://doi.org/10.1063/1.371708.

[8] Y.-C. Kao, S.-L. Ou, F.-L. Wu, and R.-H. Horng, “Performance enhancement of iii–v multi-junction solar cells using indium-tin-oxide electrodes,” *Thin Solid Films*, vol. 612, pp. 36–40, 2016. https://doi.org/10.1016/j.tsf.2016.05.045.

[9] X. Yan, F. W. Mont, D. J. Poxson, M. F. Schubert, J. K. Kim, J. Cho, and E. F. Schubert, “Refractive-index-matched indium–tin-oxide electrodes for liquid crystal displays,” *Japanese Journal of Applied Physics*, vol. 48, p. 120203, dec 2009. 10.1143/JJAP.48.120203.

[10] B. Sweetman. MBI Publishing Company, 1998. ISBN 978-1-61060-143-6.

[11] Q. Luo, “Indium tin oxide thin film strain gages for use at elevated temperatures,” 2001. https://digitalcommons.uri.edu/dissertations/AAI3025561.

[12] B. Smith, “Reflectivey and arcs_2017,” Aug 2017. Lecture Notes.

[13] H. Askari, H. Fallah, M. Askari, and M. C. Mohmmadieyh, “Electrical and optical properties of ito thin films prepared by dc magnetron sputtering for low-emitting coatings,” 2014. https://arxiv.org/abs/1409.5293.

[14] Y. S. Jung, “Spectroscopic ellipsometry studies on the optical constants of indium tin oxide films deposited under various sputtering conditions,” *Thin Solid Films*, vol. 467, no. 1, pp. 36–42, 2004. https://doi.org/10.1016/j.tsf.2004.02.047.

[15] H. A. Abd-Elnaiem, A.M., “Influence of annealing temperature on structural, electrical, and optical properties of 80 nm thick indium-doped tin oxide on borofloat glass,” *J Mater Sci: Mater Electron*, vol. 33, p. 23293–23305, 2022. https://doi.org/10.1007/s10854-022-09051-6.

[16] P. P. Edwards, A. Porch, M. O. Jones, D. V. Morgan, and R. M. Perks, “Basic materials physics of transparent conducting oxides,” *Dalton Trans.*, pp. 2995–3002, 2004.

[17] H. Köstlin, R. Jost, and W. Lems, “Optical and electrical properties of doped in2o3 films,” *physica status solidi (a)*, vol. 29, no. 1, pp. 87–93, 1975. https://onlinelibrary.wiley.com/doi/pdf/10.1002/pssa.2210290110.

[18] Wikipedia, “Band gap,” Feb 2023. https://en.wikipedia.org/wiki/Band_gap.

[19] A. S. P Manivannan, "Studies on the electrical and optical properties of reactive electron beam evaporated indium tin oxide films," *Journal of Physics D: Applied Physics*, pp. 1510–1515, 1993.

[20] T. S. Moss, "The interpretation of the properties of indium antimonide," *Proceedings of the Physical Society. Section B*, vol. 67, pp. 775–782, 1954. https://iopscience.iop.org/article/10.1088/0370-1301/67/10/306/pdf.

[21] J.-J. Lin and Z.-Q. Li, "Electronic conduction properties of indium tin oxide: single-particle and many-body transport," *Journal of Physics: Condensed Matter*, vol. 26, p. 343201, aug 2014. https://doi.org/10.1088

[22] S. K. Choi and J. I. Lee, "Effect of film density on electrical properties of indium tin oxide films deposited by dc magnetron reactive sputtering," *Journal of Vacuum Science & Technology A*, vol. 19, no. 5, pp. 2043–2047, 2001. https://doi.org/10.1116/1.1371326.

[23] D. Neerinck and T. Vink, "Depth profiling of thin ito films by grazing incidence x-ray diffraction," *Thin Solid Films*, vol. 278, no. 1, pp. 12–17, 1996. https://www.sciencedirect.com/science/article/pii/0040609095081178.

[24] T. Sasabayashi, P. K. Song, Y. Shigesato, K. Utsumi, A. Kaijo, and A. Mitsui, "Internal stress of ito, izo and gzo films deposited by rf and dc magnetron sputtering," *MRS Online Proceedings Library (OPL)*, vol. 666, p. F2.4, 2001. 10.1557/PROC-666-F2.4.

[25] J. Harrell, M. Acikgoz, H. Lieber Sasson, I. Visoly-Fisher, A. Genova, and M. Pavanello, "Models of surface morphology and electronic structure of indium oxide and indium tin oxide for several surface hydroxylation levels," *The Journal of Physical Chemistry C*, vol. 122, no. 1, pp. 584–595, 2018. 10.1021/acs.jpcc.7b10267.

[26] D. Raoufi and L. Eftekhari, "Crystallography and morphology dependence of in2o3:sn thin films on deposition rate," *Surface and Coatings Technology*, vol. 274, pp. 44–50, 2015. https://www.sciencedirect.com/science/article/pii/S0257897215003667.

[27] S. P. . A. A. S. Marikkannu, C. Sanjeeviraja, "Studies on the structural, optical, and electrical properties of jet-nebulized spray pyrolysis ito thin films," *Journal of Materials Science: Materials in Electronics*, pp. 2531–2537, 2015.

[28] M. Sousa and A. da Cunha, "Optimization of low temperature rf-magnetron sputtering of indium tin oxide films for solar cell applications," *Applied Surface Science*, vol. 484, pp. 257–264, 2019. https://www.sciencedirect.com/science/article/pii/S0169433219309067.

[29] L. Hao, X. Diao, H. Xu, B. Gu, and T. Wang, "Thickness dependence of structural, electrical and optical properties of indium tin oxide (ito) films deposited on pet substrates," *Applied Surface Science*, vol. 254, no. 11, pp. 3504–3508, 2008. https://doi.org/10.1016/j.apsusc.2007.11.063.

[30] K.-H. Choi, J.-A. Jeong, J.-W. Kang, D.-G. Kim, J. K. Kim, S.-I. Na, D.-Y. Kim, S.-S. Kim, and H.-K. Kim, "Characteristics of flexible indium tin oxide electrode grown by continuous roll-to-roll sputtering process for flexible organic solar cells," *Solar Energy Materials and Solar Cells*, vol. 93, no. 8, pp. 1248–1255, 2009. https://doi.org/10.1016/j.solmat.2009.01.015.

[31] A. C. J. K. W. d. B. T. G. Je-Hsiung Lan, Jerzy Kanicki *Journal of Electronic Devices*, vol. 25.

[32] T. L. Breen, P. M. Fryer, R. W. Nunes, and M. E. Rothwell, "Patterning indium tin oxide and indium zinc oxide using microcontact printing and wet etching," *Langmuir*, vol. 18, no. 1, pp. 194–197, 2002. https://doi.org/10.1021/la015543g.

[33] J. W. Lee, B. Pathangey, M. R. Davidson, P. H. Holloway, E. S. Lambers, B. Davydov, T. J. Anderson, and S. J. Pearton, "Comparison of plasma chemistries for dry etching thin film electroluminescent display materials," *Journal of Vacuum Science & Technology A*, vol. 16, no. 4, pp. 2177–2186, 1998. https://doi.org/10.1116/1.581326.

[34] J. S. Michael Quirk, *Semiconductor Manufacturing Technology.* 2001.

[35] P. Singer, “Future of dielectric cvd: High density plasma?,” *Semiconductor International*, vol. 20, pp. 126–134, 1997.

[36] J. B. Mooney and S. B. Radding, “Spray pyrolysis processing,” *Annual review of materials science*, vol. 12, no. 1, pp. 81–101, 1982.

[37] R. Pommier, C. Gril, and J. Marucchi, “Sprayed films of indium tin oxide and fluorine-doped tin oxide of large surface area,” *Thin Solid Films*, vol. 77, no. 1, pp. 91–98, 1981. https://doi.org/10.1016/0040-6090(81)90363-1.

[38] A. A. Fries, *Chemical Warfare.* 2008.

[39] M. Instruments, *Atomic Layer Deposition*, 2023.

[40] J. W. Elam, D. A. Baker, A. B. F. Martinson, M. J. Pellin, and J. T. Hupp, “Atomic layer deposition of indium tin oxide thin films using nonhalogenated precursors,” *The Journal of Physical Chemistry C*, vol. 112, no. 6, pp. 1938–1945, 2008. https://doi.org/10.1021/jp7097312.

[41] Z. Zhang, Y. Hu, Z. Lin, M. Si, A. Charnas, K. Cho, and P. D. Ye, “Atomically thin indium-tin-oxide transistors enabled by atomic layer deposition,” *IEEE Transactions on Electron Devices*, vol. 69, no. 1, pp. 231–236, 2022. https://doi.org/10.1109/TED.2021.3129707.

[42] M. Leskelä and M. Ritala, “Atomic layer deposition chemistry: Recent developments and future challenges,” *Angewandte Chemie International Edition*, vol. 42, no. 45, pp. 5548–5554, 2003. https://doi.org/10.1002/anie.200301652.

[43] J. R. Arthur, “Molecular beam epitaxy,” *Surface Science*, vol. 500, no. 1, pp. 189–217, 2002. https://doi.org/10.1016/S0039-6028(01)01525-4.

[44] S. K. Hua Zhou, Xiaxia Liao, “Effects of strain on ultrahigh-performance optoelectronics and growth behavior of high-quality indium tin oxide films on yttria-stabilized zirconia (001) substrates,” *Journal of Material Science: Materials In Electronics*, vol. 32, p. 21462–21471, 2021. https://doi.org/10.1007/s10854-021-06654-3.

[45] R. G. A. M. A. N. W. Nassim Derriche, Simon Godin, “Reflection high-energy electron diffraction,” 2019. https://phas.ubc.ca/ berciu/TEACHING/PHYS502/PROJECTS/RHEED.pdf.

[46] N. Shanmugam, R. Pugazhendhi, R. Madurai Elavarasan, P. Kasiviswanathan, and N. Das, “Anti-reflective coating materials: A holistic review from pv perspective,” *Energies*, vol. 13, no. 10, 2020. https://www.mdpi.com/1996-1073/13/10/2631.

[47] M. Ohring, *Discharges, Plasmas, and Ion-Surface Interactions*, vol. 2, ch. 4, pp. 145 – 197.

[48] M. Jackson, “Plasma parts 1 and 2: Basics and sputtering,” Oct 2021. Lecture Notes.

[49] J. Green, “An overview of magnetron sputtering,” Jan 2023. https://www.sputtertargets.net/blog/an-overview-of-magnetron-sputtering.html.

[50] K. S. H. O. Y. F. H. S. Taku Suyama, Hansin Bae and H. Toyoda, “Quantitative evaluation of high energy o ion particle flux in a dc magnetron sputter plasma with an indium tin oxide target,” *Journal of Physics D: Applied Physics*, vol. 50, no. 44, 2017. DOI 10.1088/1361-6463/aa87a1.

[51] J. O’Hanlon, *A User’s Guide to Vacuum Technology.* Wiley, 2005. ISBN: 9780471467151.

[52] G. Packard, A. Rosenfeld, R. G. Manley, and K. D. Hirschman, “Flash lamp annealed ltps tfts with ito bottom-gate structures,” *ECS Transactions*, vol. 98, p. 141, sep 2020. https://dx.doi.org/10.1149/09807.0141ecst.

[53] P. Infante, "Characterization of dc reactive sputtered indium tin oxide thin films," 1994.

[54] G. Haacke, "New figure of merit for transparent conductors," *Journal of Applied Physics*, vol. 47, no. 9, pp. 4086–4089, 1976. https://doi.org/10.1063/1.323240.

[55] R. Gordon, "Criteria for choosing transparent conductors," *MRS Bulletin*, vol. 25, pp. 52–57, 2000. https://doi.org/10.1557/mrs2000.151.

[56] M. H. Bohra, "Process development for single-crystal silicon solar cells," 2014.

[57] R. Kamat, "Engineered emitters for improved silicon photovoltaics," 2016. https://ui.adsabs.harvard.edu/abs/2016MsT.........31K.

[58] G. Tuttle, "Tlm measurement, semiconductor fabrication," 2016. https://gtuttle.net/fabrication/topics/tlm_measurements.pdf.

[59] W. Jeitschko, "Refinement of the crystal structure of tisi$_2$ and some comments on bonding in tisi$_2$ and related compounds," *Acta Crystallographica Section B*, vol. 33, pp. 2347–2348, Jul 1977. https://doi.org/10.1107/S0567740877008462.

[60] S. A. Chambers, D. M. Hill, F. Xu, and J. H. Weaver, "Silicide formation at the ti/si(111) interface: Diffusion parameters and behavior at elevated temperatures," *Phys. Rev. B*, vol. 35, pp. 634–640, 1987. https://link.aps.org/doi/10.1103/PhysRevB.35.634.

[61] R. Banerjee, D. Das, S. Ray, A. Batabyal, and A. Barua, "Characterization of tin doped indium oxide films prepared by electron beam evaporation," *Solar Energy Materials*, vol. 13, no. 1, pp. 11–23, 1986. https://doi.org/10.1016/0165-1633(86)90024-9.

[62] C. Q. L. X. e. a. Yang, T., "Low-temperature synthesis of ti3al(sn)c2 solid solution using replacement reaction," *Journal of Materials Science: Materials in Electronics*, vol. 31, p. 20601–20610, 2020. https://doi.org/10.1007/s10854-020-04580-4.

[63] H. Okamoto, "Sn-ti (tin-titanium)," *Journal of Phase Equilibria and Diffusion*, vol. 31, p. 202–203, 2010. https://doi.org/10.1007/s11669-010-9663-2.

Appendix A

Table 6.1: Processing Details for P-type Si Solar Cells with ITO ARC

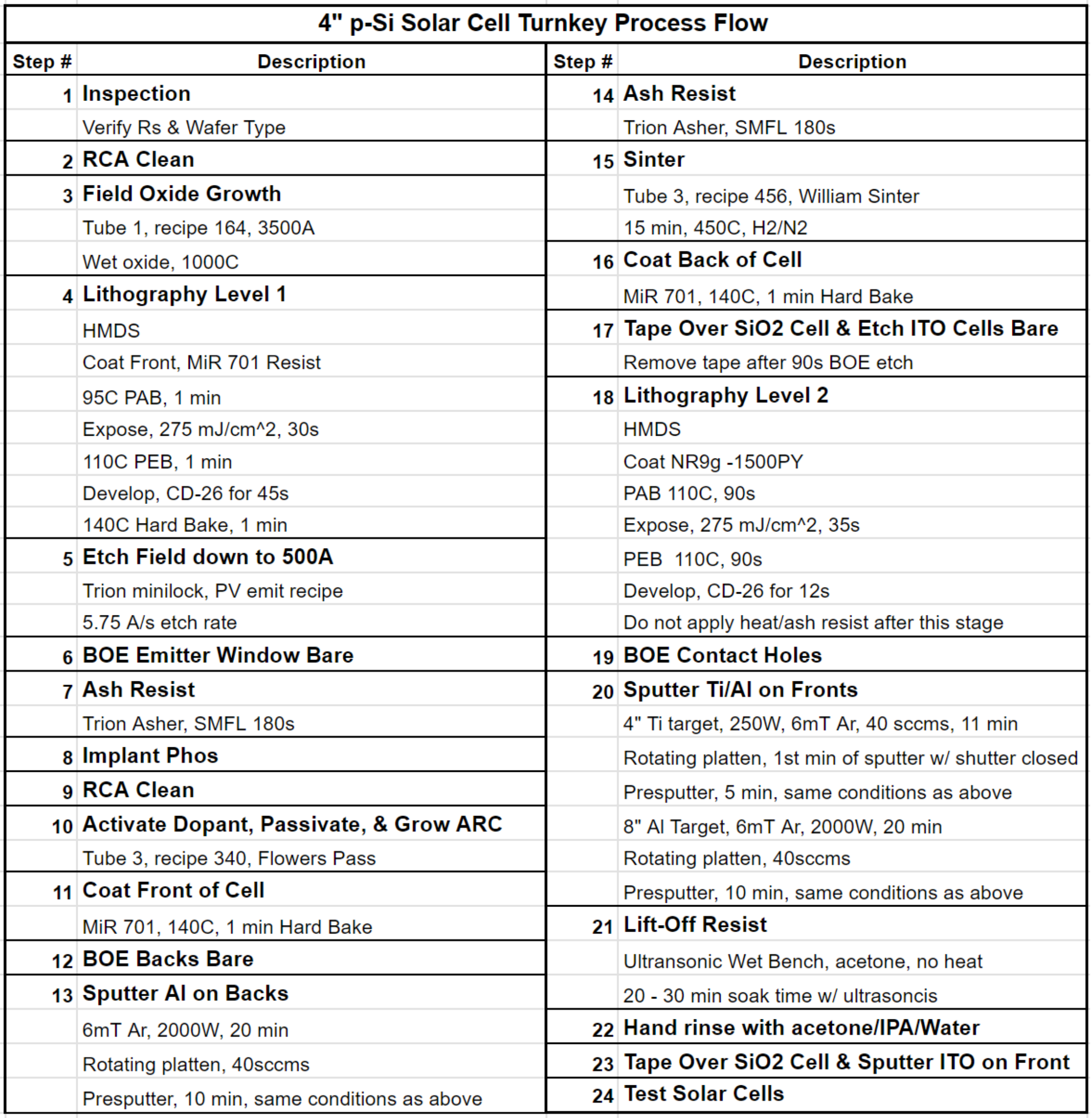

4" p-Si Solar Cell Turnkey Process Flow			
Step #	**Description**	**Step #**	**Description**
1	**Inspection**	**14**	**Ash Resist**
	Verify Rs & Wafer Type		Trion Asher, SMFL 180s
2	**RCA Clean**	**15**	**Sinter**
3	**Field Oxide Growth**		Tube 3, recipe 456, William Sinter
	Tube 1, recipe 164, 3500A		15 min, 450C, H2/N2
	Wet oxide, 1000C	**16**	**Coat Back of Cell**
4	**Lithography Level 1**		MiR 701, 140C, 1 min Hard Bake
	HMDS	**17**	**Tape Over SiO2 Cell & Etch ITO Cells Bare**
	Coat Front, MiR 701 Resist		Remove tape after 90s BOE etch
	95C PAB, 1 min	**18**	**Lithography Level 2**
	Expose, 275 mJ/cm^2, 30s		HMDS
	110C PEB, 1 min		Coat NR9g -1500PY
	Develop, CD-26 for 45s		PAB 110C, 90s
	140C Hard Bake, 1 min		Expose, 275 mJ/cm^2, 35s
5	**Etch Field down to 500A**		PEB 110C, 90s
	Trion minilock, PV emit recipe		Develop, CD-26 for 12s
	5.75 A/s etch rate		Do not apply heat/ash resist after this stage
6	**BOE Emitter Window Bare**	**19**	**BOE Contact Holes**
7	**Ash Resist**	**20**	**Sputter Ti/Al on Fronts**
	Trion Asher, SMFL 180s		4" Ti target, 250W, 6mT Ar, 40 sccms, 11 min
8	**Implant Phos**		Rotating platten, 1st min of sputter w/ shutter closed
9	**RCA Clean**		Presputter, 5 min, same conditions as above
10	**Activate Dopant, Passivate, & Grow ARC**		8" Al Target, 6mT Ar, 2000W, 20 min
	Tube 3, recipe 340, Flowers Pass		Rotating platten, 40sccms
11	**Coat Front of Cell**		Presputter, 10 min, same conditions as above
	MiR 701, 140C, 1 min Hard Bake	**21**	**Lift-Off Resist**
12	**BOE Backs Bare**		Ultransonic Wet Bench, acetone, no heat
13	**Sputter Al on Backs**		20 - 30 min soak time w/ ultrasoncis
	6mT Ar, 2000W, 20 min	**22**	**Hand rinse with acetone/IPA/Water**
	Rotating platten, 40sccms	**23**	**Tape Over SiO2 Cell & Sputter ITO on Front**
	Presputter, 10 min, same conditions as above	**24**	**Test Solar Cells**